UNIVERSITÄT PADERBORN
Die Universität der Informationsgesellschaft

Building Blocks for Integrated Homodyne Detection with Superconducting Nanowire Single-Photon Detectors

Der Naturwissenschaftlichen Fakultät
der Universität Paderborn
zur Erlangung des Doktorgrades

Dr. rer. nat.

vorgelegt von

Maximilian Protte

Paderborn, July 25, 2023

Contents

Summary 1

Integration of optical components with high precision and accuracy will be essential for future quantum applications in communications and sensing. For this, we need low-loss waveguides, quantum-state generation, active modulation, and single photon detection.

In this work, I present the fabrication of devices for each element of this list in titanium in-diffused lithium niobate (Ti:LN) using a maskless optical lithography. Using a single lithography system, we can fabricate devices whose structure sizes span six orders of magnitude (from hundreds of nanometers to several centimeters).

We demonstrate low-loss waveguiding in Ti:LN, periodic poling for quasi-phase matching, electro-optic modulation, and fabrication of superconducting nanowire single photon detectors (SNSPDs) on silicon with widths in the micrometer range. The versatility gained by using a maskless laser lithography will help developing applications in the field of quantum communications and sensing.

While fabrication of SNSPDs on z-cut lithium niobate remains a challenge, we combined multiple devices realized in Ti:LN to demonstrate a first implementation of homodyne detection with off-chip SNSPDs. Interference with vacuum showed that the detector can be used as a linear detector by evaluating the count rate of a SNSPD and that the signal is shot-noise limited. We were able to measure a shot-noise clearance of 49 dB, which is the highest reported clearance for an optical homodyne detector. The results demonstrate the versatility of these detectors for exploring the wave-particle duality of light.

Zusammenfassung 2

Die Integration optischer Bauteile mit hoher Präzision und Genauigkeit wird für künftige Quantenanwendungen in den Bereichen der Kommunikation und Sensorik unerlässlich sein. Dafür benötigen wir verlustarme Wellenleiter, Erzeugung von Quantenzuständen, aktive Modulation und Einzelphotonendetektion.

In dieser Arbeit präsentiere ich die Herstellung von Bauteilen für jedes Element dieser Liste in Titan-eindiffundiertem Lithiumniobat (Ti:LN) mittels maskenloser optischer Lithografie. Mit einem einzigem Lithografiesystem können wir Strukturen, deren Größen sich über sechs Größenordnungen erstrecken (von hunderten Nanometern bis zu mehreren Zentimetern), herstellen.

Wir demonstrieren verlustarme Wellenleitung, periodische Polung, elektrooptische Modulation und supraleitenden Einzelphotonendetektoren (SNSPDs) auf Silizium mit Mikrometerbreite. Die Vielseitigkeit, die durch den Einsatz einer maskenlosen Lithografie gewonnen wird, trägt dazu bei, Anwendungen im Bereich der Quantenkommunikation und Sensorik voranzutreiben.

Während die Herstellung von SNSPDs auf Lithiumniobat eine Herausforderung bleibt, haben wir mehrere der in Ti:LN realisierten Bauteile kombiniert, um eine erste Implementierung der Homodyne-Detektion mit Off-Chip SNSPDs zu zeigen. Die Interferenz mit dem Vakuum zeigte, dass der Detektor als linearer Detektor verwendet werden kann und dass das Signal durch Schrotrauschen limitiert ist. Wir haben festgestellt, dass die Lokaloszillatorleistung um 49 dB reduziert werden kann, bevor der Detektor nicht mehr schrotrauschbegrenzt ist. Dies ist der bisher größte gemessen Bereich. Die Ergebnisse zeigen die vielseitige Verwendbarkeit dieser Detektoren zur Erforschung des Welle-Teilchen-Dualismus des Lichts.

Introduction 3

The field of photonics spans many textbooks, exploring the fundamental properties of light and technologies for information transmission, processing, and storage. For the development of new technologies, the nature of light must be well understood and studied.

Historically, there exist two possible ways to describe the nature of light: The classical and the quantum description. In the classical regime we consider light as an electromagnetic wave and two-wave interference is a clear proof of the wave-like behavior. The interference of light was demonstrate by Thomas Young in his famous double slit experiment [1]. To describe the propagation of electromagnetic waves in a more quantitative fashion we require the Maxwell equations [2]. Solving them and the wave equation yields a mathematical solution of an electromagnetic wave, for a given boundary condition [3]. This solution is often referred to as a *mode* and plays an essential role in classical and quantum optics. Many applications have been developed, where light is considered as a classical resource. One of these major applications is the transmission of information with classical optical signals over a glass fiber link (i.e. the internet) [4].

The introduction of the concept of electromagnetic field quanta by Max Planck in 1900 led to the quantum mechanical description of light and introduced the idea of light having particle-like behavior [5]. These single quanta were later referred to as *photons*. In quantum optics we mainly consider *quantum states* $|\Psi\rangle$ which can contain multiple photons. Even if photons are often pictured as particles, they can interfere and have a wave-like character. The resulting concept of wave-particle duality is best described with the words from Nils Bohr:

> "The two views of the nature of light are rather to be considered as different attempts at an interpretation of experimental evidence in which the limitation of the classical concepts is expressed in complementary ways" [6].

With the development of a quantum mechanical description of light, ideas are emerging for new applications that take advantage of the quantum mechanical properties of light. Three major areas that have become the focus of researchers around the world are quantum computation [7, 8], communications [9, 10], and sensing [11]. The goal of any application from these fields is to gain an advantage over their classical counterparts by exploiting the quantum mechanical properties of light.

To exploit the benefits arising from the quantum mechanical treatment of light, a better understanding of its nature and methods for measuring the quantum mechanical properties of light are needed. The implementation of such methods and the interpretation of the performed measurements is not trivial. The challenge is already illustrated by the

mentioned example of wave-particle duality, where no simple answer can be given to the question of what light is. The mentioned duality in the description of light also manifest in the two popular descriptions of light fields in the modern field of quantum optics. In quantum optics we can differentiate between the discrete variable and the continuous variable case.

In the *discrete variable* (DV) case, we consider light in terms of different photon numbers n occupying a single mode of the electromagnetic field [12]. The single mode can be described by its Hamiltonian, which contains the mode's total energy and can be used to calculate its time-evolution. In the case of a single-mode electromagnetic field, the Hamiltonian takes the form of a quantum harmonic oscillator. The mode of an electromagnetic wave can thus be treated in terms of the solutions to a quantum harmonic oscillator (see eq. 3.1). The harmonic osciallator introduces different energy levels to the mode each corresponding to a *Fock state* $|n\rangle$, where n is related to the photon number occupying the mode. The Hamiltonian has the eigenvalues $\hbar\omega(n + 1/2)$, where ω is the frequency of the electromagnetic mode [12]. The photon-number operator $\hat{n}$ is the mathematical equivalent of measuring the photon number of a single electromagnetic mode, which we also refer to as a single-mode state.

As proposed by Max Planck, it follows from the eigenvalues that the energy of the electromagnetic field is discretized in single quantum units which are given by the Planck constant $\hbar$. A somewhat surprising result from this description is the vacuum state $|0\rangle$, for which no photons occupy the electromagnetic mode, nevertheless the mode exists and has a finite energy of $1/2\hbar\omega$. This number state plays a major role in all quantum optical experiments, as it will be discussed later.

The discretized nature of single photons is even more evident when we consider the polarization of a single photon Fock state $|1\rangle$. When sending a stream of single photons with horizontal/vertical polarization onto a polarizing beam splitter, the beam splitter projects the single photon state onto the horizontal $|H\rangle$ and vertical state $|V\rangle$. Depending on the polarization of the input photon, the photon is detected in one or the other arm of the beam splitter. If we change the polarization to a diagonal polarization ($|D\rangle$), the single photons will, on average, split evenly between the two ports of the beam splitter. If only a single photon is observed at any given time, there will never be coincidence detections between the two ports because the single photon cannot split between the two arms. It must randomly choose one arm of the beam splitter. From this simple example, we see that the measurement outcomes are discrete values with only two possible outcomes: The photon comes out one port or the other. This case is referred to as the discrete variable case. The pictorial idea of a light particle hitting a beam splitter and deciding on a path illustrates the particle-like behavior of light [13].

The second popular description of quantum light is referred to as the *continuous variable* case (CV). Going back to the eigenvalues of the Hamiltonian for a single-mode electromagnetic field, we see that they correspond to the eigenvalues of a quantum harmonic

oscillator. The Hamiltonian for such a system is given by

$$\hat{H} = \hbar\omega \left(\hat{n} + \frac{1}{2} \right) = \frac{1}{2}(\hat{p}^2 + \omega^2 \hat{q}^2) \tag{3.1}$$

with the number operator $\hat{n}$. On the right side of the equation, we see the two canonical operators $\hat{p}$ and $\hat{q}$, which are referred to as the quantum mechanical counterpart of the classical momentum and position of the harmonic oscillator. In the literature, instead of $\hat{p}$ and $\hat{q}$, the dimensionless quadrature operators $\hat{X}_1$ and $\hat{X}_2$ are often used.

The quadrature operators are measurement operators associated with two field amplitudes that oscillate out of phase with each other by 90°. When the quadratures are measured, the results are continuously distributed, which distinguishes them from the case of discrete variables. Additionally, the quadratures are phase-dependent. The phase dependence distinguishes this picture even more decisively from the particle-like nature of photons and their photon statistics. It is obvious that the case of continuous variables is associated with the wave-like properties of quantum light [12]. This simplified summary of the two cases already shows that depending on the measurement operation the results that can be obtained from measuring a quantum state can differ and different types of detection mechanisms are required to measure the photon-number/quadrature operator.

In the case of DV, it is a matter of measuring the photon number of a quantum state. In this method, the photon statistics are calculated from an ensemble measurement of a quantum state. From the photon statistics we can gain insights on the nature of light [14–16]. In quantum optics many different states exist that have different photon statistics. A coherent state $|\alpha\rangle$ is the closest quantum approximation to the field generated by a laser. The coherent state is an eigenstate of the annihilation operator $\hat{a}$ with the complex eigenvalue α. The annihilation operator $\hat{a}$ is interpreted as the subtraction of a photon from a state. A coherent state is a quantum state closely related to a classical laser source, since its electric field expectation values have the form of the classical expression, which includes a sinusoidal dependence. Its photon statistics can be described with a Poisson distribution [12]. In comparison, for a Fock state with the photon number 2 we will always measure two photons. A coherent state with a mean photon number $\bar{n}$ will not have the same photon statistics as a single photon also having a mean photon number $\bar{n}$. It is evident that by measuring the photon statistics we can gain insights on the quantum state and its nature. Achilles et al. [17] demonstrated the characterization of a non-classical state by measuring the counting statistics.

In order to measure the photon statistics, we require detectors that are sensitive to single photons and can differentiate between different photon numbers. Over the last two decades, it hase become evident that superconducting detectors like transition edge sensors (TES) and superconducting nanowire single-photon detectors (SNSPDs) are powerful detectors capable of filling this void in the near-infrared wavelength range [18, 19]. Miller et al. [20] demonstrated the first TESs for optical photons. One year later, Gol'tsman et al. [21] demonstrated the first SNSPD.

Photon-number resolution (PNR) is intrinsically given for TESs by acting as a bolometer (i.e. directly measuring the energy of the absorbed light). The TESs are cooled below and biased within the superconducting transition. When a single photon is absorbed by the detector this leads to a measurable increase in the resistance of the film. Lita et al. demonstrated the PNR of TESs for photons in the near-infrared with an efficiency of 95% [22]. TESs are operated at temperatures < 100 mK and their signal needs to be amplified with *superconducting quantum interference devices* (SQIRDs) which results in a high complexity and operation cost for TESs. With count rates up to 1 MHz, their maximum operating speed is rather low [19, 23].

In comparison, a single SNSPD is considered a click detector that detects the presence of one or more photons. Per se, it cannot distinguish between one or more photons and therefore has no PNR on its own. The detectors are operated at slightly higher temperatures (< 4 K) in comparison to TESs. To date, SNSPDs have demonstrated near-unity detection efficiency [24, 25], low dark counts [26], and high temporal resolution [27], which is why they are considered the gold standard for single photon detection. Fitch et al. [28] and Achilles et al. [29] showed that click detectors such as SNSPDs can also achieve photon-number resolution with a time-multiplexing scheme. Using the temporal degree of freedom is just one method to achieve PNR, it has also been demonstrated with spatial multiplexing [30]. Thus, SNSPDs are useful detectors when it comes to studying the discrete properties of quantum states. A schematic of a multiplexing scheme is shown in fig. 3.1.

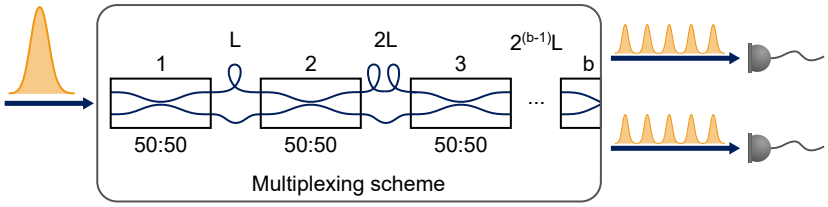

Figure 3.1: Schematic of a multiplexing scheme to achieve quasi-photon-number resolution with click detectors. An optical pulse is split on a beam splitter and one arm is delayed. A cascade of this structure, as shown here, leads to a sequence of pulses. Ideally each pulse containing approximately one photon, which can then be counted with click detectors.

To understand the measurement operations typically done in the continuous variable case, we first need to introduce the phase space of light derived from the treatment of an electromagnetic mode as a quantum harmonic oscillator. In the literature, the electromagnetic field is treated in terms of a quantum harmonic oscillator where on one side the discrete photon number operator $\hat{n}$ can be used to describe the number of photons that occupy a mode of the harmonic oscillator. On the other side we can introduce the two quadratures $\hat{X}_1$ and $\hat{X}_2$. While the photon number is discretized, the two quadratures are continuously distributed and can be used to characterize a mode just like the photon-number operator. The quadratures and their variance/uncertainty for different quantum states can be best

pictured in *phase space*. The concept of phase space is essential for picturing states, operations on them and the continuous measurement outcomes. A picture of phase space with different states is given in fig. 3.2 a).

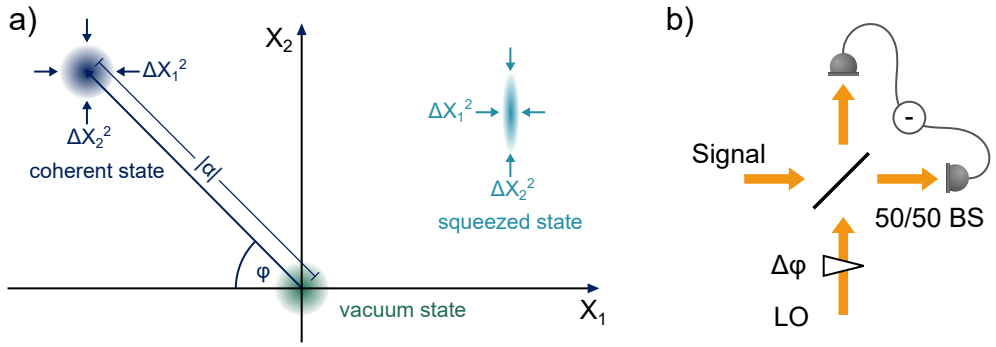

Figure 3.2: a) Drawing of phase space with a coherent state, a squeezed state and the vacuum state. The uncertainty in the quadratures $\langle \Delta \hat{X}_1^{\,2} \rangle$ and $\langle \Delta \hat{X}_2^{\,2} \rangle$ needs to fulfill the Heisenberg uncertainty principle. For a squeezed state the uncertainty in one quadrature is below the vacuum limit while the other one is increased. b) shows a schematic of a homodyne setup. By interfering a weak signal state with a strong LO on a balanced beam splitter (BS) the two quadratures can be measured when scanning the reference phase $\Delta\varphi$ of the LO.

An important example is the previously mentioned coherent state $|\alpha\rangle$. In phase space a coherent state is pictured as a ball as shown in fig. 3.2 a). The position of the state is given by its mean value of the quadratures $\hat{X}_1$ and $\hat{X}_2$. The distance of the coherent state to the origin is assosciated with the amplitude $|\alpha|$ of the coherent state. Since the quadratures do not commute, the measurement of the quadratures have to obey the Heisenberg uncertainty principle. Thus, the uncertainty $\langle \Delta \hat{X}_1^{\,2} \rangle$ and $\langle \Delta \hat{X}_2^{\,2} \rangle$ of the quadratures dictates the size covered by the state in phase space. For a coherent state, the uncertainty for both quadratures is equal ($\langle \Delta \hat{X}_1^{\,2} \rangle_\alpha = 1/4 = \langle \Delta \hat{X}_2^{\,2} \rangle_\alpha$) to the uncertainty of the vacuum state. The vacuum state, mentioned earlier, is considered a state with minimal uncertainty. Hence, the coherent state is also a state of minimal uncertainty. Since no photons occupy the vacuum mode, the amplitude of the field is zero, so it must be located at the origin.

An important example of a highly non-classical state that has not been mentioned before, but is of great importance for quantum applications, is a squeezed state [31, 32]. For squeezed light the uncertainty of one quadrature is below the vaccum noise. Since it still needs to fulfill Heisenbergs uncertainty principle the uncertainty of the other quadrature has to increase. The reduced noise of squeezed light can be used to increase the sensitivity of shot-noise limited detectors [32]. An example is the gravitational wave detector in the *Laser Interferometer Gravitational-Wave Observatory* (LIGO) [11], where the sensitivity of the gravitational wave detector was improved by introducing squeezed light into the system. Squeezed states are also an important resource for quantum information processing [33]. Their reliable characterization and generation is of great importance for applications like

quantum computing [8] and communication based on quantum key distribution (QKD) [34, 35].

Characterizing Quantum States in Phase Space

The measurement of the uncertainty area of a state can now be used to characterize a quantum state just like the photon counting statics in the DV case. With the technique of balanced homodyne detection (BHD) we are able to measure the phase-dependent probability distributions associated with measuring the quadratures $\hat{X}_1$ and $\hat{X}_2$.

The setup used for BHD is shown in fig. 3.2 b). It consists of a balanced beam splitter where two signals are interfered. The input field incident on the beam splitter are called the *local oscillator* (LO) and the signal. The LO is a bright laser-light field and provides the phase reference φ required for measuring the phase-dependency of the quadratures. We already assume here that the signal and the LO have a fixed phase relationship. This is the case in most experiments, since both signals are generated from the same laser source [36]. In strong-field homodyne detection the LO is assumed to be much stronger than the signal and powerful enough to be treated classically. The phase reference already indicates that BHD is a phase-sensitive measurement. Therefore, we need phase stabilization in the experimental setup, to ensure that the phase reference between the LO and the signal stays constant and does not fluctuate over time.

The signal is a weak quantum state that we want to characterize in phase space. After interference, both outgoing beams are detected with two linear photodetectors [36]. In the past, mainly photodiodes have been used because they are cost efficient, fast and have high efficiencies. The fact that photodiodes can be used is by far not a trivial assumption. In the context of homodyne detection, we try to reveal properties of a mode that is occupied by only a few photons. A “simple” photodiode is not sensitive to single photons, nevertheless we are able to reveal properties of the quantum state. How is that possible? The two photocurrents generated at the photodiodes are subtracted from each other. The subtracted signal contains the interference term of the LO and the signal. The difference in the currents is given by

$$\langle \hat{n}_{21} \rangle = 2^{1/2} |\alpha_{\mathrm{LO}}| \langle \hat{X}_{\varphi} \rangle \tag{3.2}$$

where $\hat{X}_{\varphi}$ is the phase dependent quadrature which we measure. The exact derivation of the above expression will be given in chap. 6.1. The interpretation of equation 3.2 is essential for the understanding of BHD. With calculating the difference we see that we can measure the values of the quadratures. By varying the phase we change the quadrature angle which we measure. This signal which is on the level of a few photons is now scaled up with the amplitude $|\alpha_{\mathrm{LO}}|$ of the LO. With the strong LO, we are able to achieve a signal strength that exceeds the noise floor of photodiodes, allowing the use of conventional semiconductor photodiodes. From the description of homodyne detection, it is evident that we are using this method to study the continuous wave-like nature of light.

We can also investigate the variance of the signal and thereby characterize the nature of a particular quantum state. Since the variance scales linearly with the intensity of the LO $|\alpha|^2$ we require linear detectors in order to correctly measure the noise of the signal. The recent theory of homodyne detection was developed by S. L. Braunstein [37] and Raymer et al. [38]. The work done by Breitenbach et al. [39] demonstrates a characterization of the complete family of squeezed states with homodyne detection, where the measured variance reveals the quantum optic properties of squeezed light. In addition, Breitenbach et al. demonstrated the reconstruction of the Wigner function $W(\hat{X}_1, \hat{X}_2)$ from the measured probability distributions of the quadratures. The Wigner function was first introduced by Wigner [40] as a function to link the wavefunction of a state to the measured probability distribution of the quadratures in phase space. The Wigner function is considered a *quasi-probability distribution* since it can take negative values. This is the case for non-classical states like the Fock state. The reconstruction of the Wigner function can therefore be used to reveal the non-classicality of states.

The Wigner function can be separated in the two different classes of Gaussian and non-Gaussian distributions. If the quadratures for a measured state have a Gaussian distribution then it is a Gaussian state. Coherent and squeezed states are examples of such states. An example for the non-Gaussian state was previously given with a single-photon Fock state, where the Wigner function takes on negative values and therefore has a non-Gaussian distribution. Lvovsky et al. [41] were the first to reconstruct the Wigner function of a Fock state with homodyne detection and thus showing its negativity.

Up to this point, I have presented two main measurement methods that are often considered in the context of quantum optics. The measurement of discrete photon statistics is a method based on the understanding of light as particles. Homodyne detection instead considers the wave-like continuous nature by interfering two signals and measuring phase-dependent correlations of the quantum mechanical quadratures. In recent years, there have been efforts in combining both measurements in phase-sensitive photon-counting experiments [42–44]. For this purpose, we can attenuate the LO in the homodyne scenario to the single-photon level. Measuring correlations in the photon number in this context is referred to as weak-field homodyne detection (WFHD). The difference in strong-field and weak-field homodyne and its implementation will be discussed in the following chapter in more detail.

3.1 The Transition from Strong-Field Homodyne Detection to Weak-Field Homodyne Detection

In WFHD, we try to encompass the particle- and wave-like nature of light by mixing a weak phase reference with a signal and then detecting the resulting signals with PNR detectors. Experimentally, WFHD has been mainly investigated by Donati et al. [43] and Thekkadath et al. [44].

In the work of Donati et al. [43] they could reveal phase correlations (a wave-like phenomena) in the photon-number basis (a particle-like description). For this, they attenuated the local oscillator to an intensity comparable to the signal, which is a split single-photon state (SSPS) generated from a nonlinear crystal. The state can be written as

$$|\Psi\rangle = \frac{1}{\sqrt{2}}(|0\rangle_A |1\rangle_B + |1\rangle_A |0\rangle_B) \tag{3.3}$$

where A and B are the two output modes of the balanced homodyne beam splitter. The state can be seen as a single photon leaving either one or the other arm of the detector.

Instead of linear photodiodes they used time multiplexed avalanche photodiodes to achieve PNR. When considering the joint probability of detecting in sum more than one photon, it is clear that the additional photons contributing to the detection event need to come from the LO. When measuring the joint probability for the detection events containing more than one photon but no more than three ($1 < m + m' > 3$) they could observe phase-dependent oscillatory behavior in the joint probability $P(m, m')$, where m and m' are the number of photons detected in mode A and B. It is somewhat surprising that the correlations of the split single-photon state is best visible when the state is mixed with the weak LO. This behavior (i.e. that the correlations scales with the strength of the weak LO) is well known for strong-field homodyning. The experiment showed clear identification of wave-like behavior measured with particle detectors.

In later work conducted by Thekkadath et al. [44], they extended the work presented earlier and explored the transition of weak-field to strong-field homodyne detection. In order to explore this transition they increased the LO power and investigated the change in the photon difference statistics. While increasing the LO power and measuring the projection of the quantum state onto photon-number states, they could observe a clear change in the probability distribution of the photon-number difference Δn between the two detector arms of the homodyne detector. At a strong enough LO they could show that the expected quadrature distribution could be measured.

In addition to tuning between the photon-number and quadrature measurements, Thekkadath et al. investigated the feasibility of a weak-field homodyne detector as a resource for the generation of interesting quantum states [44, 45]. In this context, the WFHD is used as a heralding detector. Depending on the measurement outcome of the WFHD, they could show that the photon statistics of the heralded state could be changed. In contrast, photon counting performs phase-insensitive non-Gaussian measurements by projecting light onto discrete photon states. In the work from Thekkadath et al. they could show that the non-Gaussian measurement of photon-counting has a phase-sensitive aspect to it.

The flexibility of WFHD makes it a promising tool for optical quantum information processing. Homodyne detection is considered as a phase-sensitive measurement by projecting light onto the continuous quadrature states. It is used for quantum-state characterization [46] and protocols that encode information in continuous variables [47]. In comparison, photon-counting performs phase-insensitive non-Gaussian measurements by projecting

light onto discrete photon states which are non-Gaussian states. Photon counting is essential when information is encoded in discrete variables (e.g. polarization). Additionally, it can provide a non-Gaussian resource needed for universal quantum computing with continuous variables [48]. WFHD can in principle perform both measurements by controlling the strength of the LO. For this reason, WFHD is considered a versatile tool for hybrid information protocols with discrete and continuous variables [49].

While all these experiments were performed in a scenario with rather weak fields, the feasibility of SNSPDs for strong LO fields has never been investigated. The TESs utilized in the work by Thekkadath et al. require extremely low temperatures, which makes their operation quite expensive and slow. Additionally, they do not offer high-speed operations with maximal count rates of 1 MHz [23]. The APDs used in the work by Donati et al. lack high detection efficiencies and low dark count rates at the near-infrared wavelength range, which is particularly interesting for applications in the field of quantum communication [23].

Even though SNSPDs also require cryogenic temperatures they can be operated at higher temperatures and have faster recovery times than TESs. In the past, the performance metrics of SNSPDs has been constantly improved. Detection efficiencies near unity [24, 25], low dark count rates with less than one detection event per day [26] and sub−3 ps timing resolution [27] are the current standard. The extremely low dark count rates result in a high signal-to-noise ratio (SNR) which is interesting for their application in the context of homodyne detection. If the detector can be treated as a linear detector, the high SNR may result in high shot-noise clearance. The shot-noise clearance is related to the noise of the raw output of the homodyne detector and the dark-count noise floor of the detector. A high clearance is desirable to quantify high amounts of squeezing. As shown by Breitenbach et al. [39] squeezing can be measured in terms of the noise reduction of the subtracted signal. The clearance determines how much squeezing can be measured before the noise floor of the detector is reached. Modern semiconductor-based detectors have achieved a shot-noise clearance of 37 dB at 2 MHz bandwidth [50] and 28dB at 100 MHz [51]. Since SNSPDs have never been used in this context, I want to investigate how they compare with the state-of-the-art homodyne detectors and this work will be their first implementation in the context of homodyne detection.

SNSPDs are detectors, just like TESs or APDs, that are normally used to study the particle-like nature of light, in the sense that they are used to measure photon statistics. If their suitability for strong-field homodyne detection is proven in this work, they are a versatile detector system capable of studying wave and particle-like phenomena. By multiplexing the detectors we can achieve *quasi*-photon-number resolution. It is not considered a detector with true PNR because it cannot distinguish between the absorption of one photon and the simultaneous absorption of two photons by the same detector. However, if the number of photons incident on the detector over a certain timescale is small, so that the probability of two photons being absorbed by the detector at the same time is also small, we achieve a quasi-PNR. With the PNR of multiplexed SNSPDs, they can be also utilized for the

WFHD, making them a viable detector for switching between weak-field homodyne and strong-field homodyne applications.

In order to exceed the feasibility of homodyne detection further, I will work towards the complete integration of a homodyne detector. Since homodyne detection is a phase sensitive measurement, integration of the various components of the homodyne detector is advantageous to reduce phase variations between the signal and the LO and lower phase stabilization requirements. In addition, chip-scale integration is beneficial in the long term because it will lead to modules with a high degree of miniaturization that can be mass-produced at low cost and used for quantum applications such as CV-QKD [52].

The integration of a homodyne detector for strong-field applications has been demonstrated previously by different groups around the world. The beam splitter as the most fundamental unit has been realized in different material platforms to show partially integrated homodyne detection [53–55]. Including on-chip detectors based on semiconductor photodiodes was shown by Raffaelli et al. [56] and Bruynsteen et al. [51]. In these publications the interference of the vacuum state with a local oscillator was used to show a quantum random number generator. A different approach was taken by Kaiser et al. [57], where a fully guided homodyne measurement was performed by only using off-the-shelf telecom fiber components. An almost fully integrated approach was realized for proton-exchanged lithium niobate [58]. In this case, the state generation and manipulation were integrated on chip. The actual detectors were not included on the lithium niobate chip. Probably the most complete integration, with phase control, beam splitter and on-chip detection, was realized in a silicon chip by Zwang et. al. [59]. A weak-field homodyne detector integrated on-chip has not been demonstrated to this point.

From the preceding discussion of the state-of-the-art integration of the homodyne detector was presented to varying degrees. The components demonstrated in the cited work can be grouped in three different sections. We require phase modulation and a beam splitter, we need the integration of detectors and last but not least a scalable solution for integrated quantum light sources that can be used to generate the signal state for the homodyne detector. A graphical representation for the three areas is given in fig. 3.3 where the bulk optical symbols and an exemplary representation of the integrated counterpart are shown. Although state generation is not necessarily considered part of homodyne detection, it should be considered a resource for homodyne detection and its application in CV-QKD and other CV information processes [33, 49].

An essential aspect that has not yet been discussed for integrated quantum applications is the optical loss in the system. The loss introduced into a system plays a crucial role in quantum optics and is very different from the loss in classical systems. In a classical system, the signal is amplified to compensate for the loss in the system. In quantum optics, the loss is described by mixing the vacuum $|0\rangle$ into the initial quantum state. When a state is affected by a loss, it can be treated as a beam splitter where the state enters at one port while the vacuum enters through the other port. One of the two output modes of the beam splitter is considered as the new signal, which partially contains the vacuum state. The amount of vacuum is determined by the loss in the system. The signal leaving the other

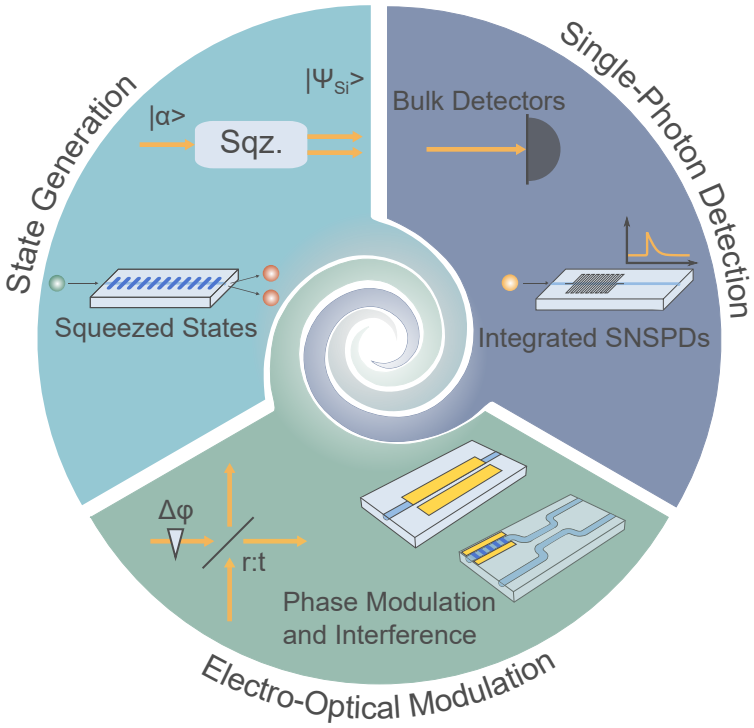

Figure 3.3: Representation of all the integration blocks that are important for (weak-field) homodyne detection. The integration of quantum light sources, the modulation of light and the detection of light are the three main building blocks. In each of the three areas a bulk optic representation and their integrated counterpart are displayed.

arm of the beam splitter is lost. Since "the presence of vacuum" is measurable in quantum optics, the loss affects the measurement results for a state which is influenced by loss. For squeezed light in particular loss reduces the amount of measurable squeezing [60, 61]. Since high amounts of squeezing are required for applications like CV quantum computing [8], we require low-loss integration systems. Additionally, loss leads to a smoothed quadrature distribution [36]. If the losses are high enough, it can completely remove any negativity from the Wigner function, leaving the non-classical properties of the initial state unrevealed. Therefore, all components displayed in fig. 3.3 will need to be fabricated such that they add a minimal loss to the system. Since the production of the various components will make up the bulk of this work, I would like to briefly highlight some aspects to consider in terms of the features that an integration platform should offer, and how these are taken into account practically.

3.2 Integrating a Homodyne Detector

To create an integrated platform for quantum photonics, one needs to realize a toolbox of high-yield functional devices. The integration platform has to offer low-loss waveguiding, quantum light sources, low-loss fast optical switching, single-photon detection and very large scale integration [62, 63]. We require low-loss because in the context of homodyne detection loss reduces the amount of measurable squeezing. Quantum light sources for squeezed light or single photons are used as resources for quantum applications like quantum key distribution [9, 10], quantum computing [8, 64] or quantum sensing [11]. Fast optical switching is of interest for feed-forward applications in the context of quantum communication or computation [65]. In combination with integrated detectors, a simple scheme involving the detection of a photon and the subsequent manipulation of another photon based on the previous detection shows rudimentary information processing.

The integration of all these components only makes sense for a commercial application, when they can be fabricated with a high yield, reproducibility and efficiency. As part of homodyne detection, we perform interference experiments that require a stable phase reference between the LO and the signal. Integration reduces the influence of environmental effects on the phase and thus eases the requirements for phase stabilization and therefore, integrating a homodyne detector is the most sensible way forward.

Up to this point, a variety of integration platforms exist, all of which have different advantages and disadvantages. In the following, I will discuss some of the most popular integrated optics platforms in the context of their application in quantum optics. It is not the scope of this work to give a complete overview of different material platforms and a more detailed overview can be found in [62, 63]. Nevertheless, I would like to highlight just a few of the most important platforms in integrated photonics and their suitability for quantum applications. For the purposes of this introduction, I will briefly discuss silicon, silicon nitride, gallium arsenide, and lithium niobate as integration platforms, as they best illustrate the platform requirements and are considered the most advanced platforms.

Silicon: One of the most studied materials for integrated photonics is silicon. The amount of research that has gone into developing today's mature manufacturing processes is unmatched by other platforms. Due to the mature fabrication based on CMOS structures, it is possible to pattern wafer-sized complex architectures. The strong confinement of silicon waveguides leads to a high component density. Due to the strong confinement, light is more likely to be scattered due to the sidewall roughness of the waveguide [66]. The biggest drawback of silicon photonics for quantum applications is two-photon absorption (TPA), where two photons at 1.55 µm are absorbed in the valance band. Consequently, TPA is mainly a problem when high-power nonlinear processes are used. Moving to longer wavelength can heavily reduce the TPA, reducing the nonlinear propagation loss [67]. One drawback is that the supporting infrastructure must be developed for longer wavelengths. As a first step Biele et al. demonstrated a homodyne experiment with bulk optics in the 2 µm band [68].

Silicon Nitride: Moving to silicon nitride as a material with a wider bandgap eliminates the problem of two photon absorption at the telecom wavelength. Having the possibility to pattern silicon nitride with the matured CMOS technologies, leads to low-loss waveguiding with propagation losses $< 0.1\,\mathrm{dBm}^{-1}$ [69]. Since unstrained silicon and silicon nitride have no $\chi^{(2)}$ for spontaneous parametric down conversion (SPDC), nonlinear processes based on spontaneous four-wave mixing (SFWM) have to be used for quantum-state generation. The SFWM scales with the much smaller $\chi^{(3)}$, which requires the use of ring resonators with high quality factors, adding another layer of complexity [70]. While SWFM is considered an all-optical process, electric-field induced second harmonic generation (EFISHG) had been proposed in the early 1960s using an external electric field to break the symmetry and induce a strong $\chi^{(2)}$. This effect has been demonstrated for silicon waveguides [71].

Gallium Arsenide: Such nonlinear processes can be used to generate squeezed light or single photons and have a probabilistic nature. An on demand single-photon source is realized with the help of quantum dots. A quantum dot is a semiconductor particle with a size of a few nanometers. Due to the spatial confinement of the dot in all three dimensions its emission spectrum is comparable to that of an atom. For this reason they are also called artificial atoms in which single electron-hole pairs can be trapped to generate on-demand single photons [72]. These quantum dots are mostly based on III-V semiconductors [64] and can be either homogeneously or heterogeneously grown on a substrate or placed on an underlying waveguide layer by pick and place methods [73]. Gallium arsenide (GaAs) is the platform which is most developed compared to other III-V platforms. Due to the rather high propagation losses, compared to other platforms like silicon nitride, GaAs is not suitable for patterning large scale circuits [74]. That is why there have been many experiments on combining hybrid structures based on GaAs and SiN [73, 75].

Another important feature that the integration platform should provide is active refractive index modulation for phase control and variable switching. Ideally, one can make use of the Pockels effect which allows for high modulation speeds [76]. From the presented platforms thus far, only GaAs offers this possibility. For other platforms, like silicon nitride, switching can be achieved by electrostatic devices up to megahertz bandwidth [75].

Lithium Niobate: Alongside GaAs, lithium niobate (LN) is a second platform utilizing the Pockels effect for electro-optical modulation. Besides its electro-optical properties LN offers a strong $\chi^{(2)}$ for quantum-state generation. Even though it is a probabilistic process, it can be used to generate squeezed states with squeezing up to 6 dB in a single pass continuous wave configuration [77] and is widely used for state generation in quantum optical experiments. Due to the wide transparency of lithium niobate from $0.4 - 5\,\mu\mathrm{m}$, the potential to fabricate waveguides with low absorption is present.

When discussing lithium niobate in more detail we have to consider two different approaches. In recent years, thin-film lithium niobate (TFLN) has raised much attention. To fabricate waveguides in TFLN a dry etching process can be used. By etching a few 100 nm,

waveguides with propagation losses of 0.27 dB/cm can be realized on a wafer scale [78]. Due to the underlying silicon dioxide layer a moderate mode confinement, which is comparable to silicon nitride can be achieved [75]. The electro-optical and nonlinear properties of lithium niobate can thus be used more efficiently. Due to the moderate confinement in TFLN, on-chip coupling is generally achieved by grating couplers, which do not easily achieve coupling efficiency close to unity and do not exhibit robust and long-term stable coupling [79].

Another approach to achieve waveguiding in lithium niobate is to diffuse a thin metal layer (titanium in our case) into the crystal, thereby locally changing the refractive index [80]. While for TFLN we have a refractive index contrast around one, the change in the refractive index in titanium in-diffused lithium niobate (Ti:LN) is two orders of magnitude smaller. For Ti:LN, propagation losses < 0.1 dB/cm can be measured [81–83]. The weak confinement leads to mode sizes comparable to a standard single-mode fiber at 1.55 µm. Due to the high mode matching (up to 90 %), on-chip coupling can be achieved by butt-coupling with standard glass fiber [84].

Due to the efficient on-chip coupling a modular-based approach towards building a quantum network can be taken. Because the component density for Ti:LN is comparably small, a functional modular-based quantum network would consist of single chips, each one with a few high-performing components, all connected with glass fiber. With this approach, certain modules can be exchanged when they break, or they can be replaced by better performing modules. Taking the same approach with platforms with strong confinement is challenging since achieving highly efficient and robust on-chip coupling is still an issue of current research.

Ti:LN has a long history and has been in development for more than a decade at Paderborn University in the workgroups of Prof. Sohler [81, 85] and Prof. Silberhorn [84]. But even though it has been well studied for applications in the classical regime it is still of interest for researchers working in the quantum optical regime. The work of Luo et al. [86] demonstrated the bunching of two single photons on a beam splitter (i.e., Hong-Ou-Mandel interference) in a fully integrated Ti:LN chip. To date, this is the most advanced integrated quantum optical experiment performed in Ti:LN. In the scope of this work Ti:LN will be the integration platform of choice. Although interest in TFLN has increased in the recent past, we believe that the insights that can be gained for Ti:LN are also relevant to research on TFLN.

The transition from classical experiments to quantum optics involving photon counting experiments requires the capability of detecting single photons. Previously, I have discussed the potential of SNSPDs in this context. Many different material platforms like NbN [21], NbTiN [87, 88] MoSi [89], and WSi [90–92] have been used to build superconducting detectors [93]. For this work, amorphous tungsten silicide has been used and I will therefore restrict myself to this material moving forward. The integration of SNSPDs has already been demonstrated on many platforms [62]. Höpker et al. [94] already demonstrated SNSPDs on Ti:LN. Due to the weak coupling of the evanescent field of the waveguide mode to the detector, the detector lacks high detection efficiency. In addition, the pyroelectric

properties of lithium niobate cause damage to the detector, resulting in low detector yield. Both problems are addressed in this work by changing the detector geometry.

The WSi-based detectors consist normally of a 4.5 nm thick film that is operated below < 1 K. The width of the nanowires is in the range of $80 - 200$ nm, which requires the fabrication with electron-beam lithography. Since the fabrication with e-beam lithography is expensive and time consuming, the use of optical lithography would be a desirable alternative.

It was shown that by decreasing the superconducting film thickness and scaling the width of the nanowire up to the micrometer scale, detectors which are sensitive to single photons can be fabricated by optical mask lithography [95, 96]. The potential of patterning large scale detector structures by optical lithography was highlighted in the work of Wollman et al. [97]. Furthermore, the transition to micrometer-wide structures is of interest for integration with waveguides that exhibit low confinement, as these are expected to amplify system detection efficiency [94]. Therefore, the utilization of micrometer-wide SNSPDs will be the focus of this work.

For this thesis I developed the fabrication process for micron-wide superconducting nanowire single-photon detectors with optical laser-lithography (see chap. 5.3) [98]. The structuring process enables large-scale devices with reduced stitching, fast and easy prototyping of arbitrary detector geometries and all-in-one-step patterning of detectors, additional electronics and contact pads. The demonstration of micron-wide SNSPDs represents the first fabrication of these using direct laser lithography [98]. The future integration of SNSPDs with waveguides restricts us to material platforms that are compatible with cryogenic temperatures. Therefore, the performance of the functional devices of the integration platform must be tested at cryogenic temperatures. For this we investigated the compatibility of Ti:LN with low temperatures. The work by Lange et al. [99] shows a working SPDC source at cryogenic temperatures. Electro-optical devices at these temperatures were investigated by Thiele et al. [100].

Even though Ti:LN has been well studied in Paderborn, I was able to contribute to the fabrication of devices in lithium niobate during my research. In the past, lithium niobate was patterned using optical mask lithography. One issue with optical mask lithography is that it does not offer flexibility in sample design. If there is no possibility to manufacture masks in your facility, expensive masks with long delivery times have to be ordered. Especially in research, there is a need for high flexibility and rapid prototyping, which direct laser lithography can provide.

In the case of direct laser writing, a UV laser beam is focused on a sample. By scanning the sample surface an arbitrary design can be patterned into resist. Since direct laser lithography has never been used in Paderborn for patterning integrated circuits in lithium niobate, part of my research was to develop the recipes for patterning integrated devices for state generation, modulation and detection as shown in fig. 3.3. The processes developed in this regard will be discussed in chap. 4. The ability to fabricate all components shown in fig. 3.3 with a single patterning tool simplifies the fabrication and leads to rapid prototyping.

With the combination of processes from all three sections of fig. 3.3 on a single chip, I wanted to verify the feasibility of SNSPDs for homodyne detection. While the interference of the LO and the signal will be carried out in an integrated fashion, off-chip SNSPDs will be used to investigate their feasibility for strong-field homodyne detection. With this SNSPDs would be considered detectors that are able to study the particle and wave-like nature of light and add to their versatility in the research field of quantum optics. To present the steps I have taken in this direction, I structured this thesis as follows.

In chapter 4, I will present the work done on process optimization to realize a toolbox for integrated quantum optics in lithium niobate. I will concentrate on the basic waveguiding mechanism, quasi-phase matching for quantum-state generation and the patterning of electrodes on LN to make use of the electro-optical properties. For all three blocks the necessary theoretical background will be given in chapter 4. Progress on integrating superconducting detectors on lithium niobate will be presented in chapter 5. The focus of this chapter is on the fabrication of micron-wide superconducting nanowire single-photon detectors. In the following chapter 6, I will present the results of the performed integrated homodyne detection experiment with single SNSPDs. A more detailed theoretical description of homodyne detection and quantum optics will be given in this chapter. Although full integration was not done because off-chip detectors were used, this work represents the first implementation of a homodyne detector with SNSPDs. The conclusion and an outlook will be given in chapter 7.

Development of Integrated Components in Lithium Niobate

4

Just as with today's CMOS electronics, with their technological advances in integration, the future of optical applications lies in the integration of components into advanced optical circuits to perform various optical tasks. From this point onward, we will be concentrating on congruent lithium niobate as an integration platform, since it will be the foundation of the later fabricated integrated components [101, 102]. A variety of devices that can be used for quantum applications have been established in Ti:LN for a long time. Nevertheless, the requirements of superconducting nanowire single-photon detectors for quantum experiments, result in building the toolbox shown in fig. 3.3 for cryogenic temperatures. While the experimental testing of individual components was carried out by my colleagues Nina Lange [103], and Frederik Thiele [100, 104], it was my task to develop the fabrication of these components based on direct laser lithography.

In the course of this chapter, I will discuss the theoretical background for the different components presented in this work and how they will be experimentally fabricated. In chap. 4.1, I will first concentrate on the waveguiding properties of lithium niobate, which forms the basis of the component toolbox. For efficient nonlinear processes, quasi-phase matching achieved by periodic poling is crucial. Therefore, I will explain the necessary theoretical background for the nonlinear interaction and its experimental investigation in chap. 4.2. In the last section 4.3, I will present the electro-optical properties and the fabrication processes for the electrode fabrication.

4.1 Waveguiding in Lithium Niobate

A waveguide is defined by guide light with a minimal loss of energy by restricting the propagation direction of the light. The confinement of light is described by the refractive index distribution of the guiding material and its surrounding. The refractive index is a dimensionless number that indicates the ability of a medium to bend light, with light bending diffracted towards the region of higher refractive index. Therefore, to describe the waveguide properties of a geometry, we need to take the refractive index distribution of the geometry into consideration.

The contrast in the refractive index distribution determines whether we are talking about a strongly confined mode or a weakly guided mode. Silicon ridge waveguides have a

strong confinement due to the high refractive index contrast of silicon and its surrounding material. In comparison, metal in-diffused lithium niobate forms a platform which offers weak confinement due to a refractive index contrast that is three orders of magnitude smaller.

4.1.1 Background

The theory presented in the following will be taken from [3, 105, 106]. More details can be found in the referenced textbooks. In order to describe optical waveguiding in a more quantitative way, one has to consider the Maxwell equations

$$\begin{aligned} \nabla \times E &= -\frac{\partial B}{\partial t}, \\ \nabla \times B &= \mu_0 \frac{\partial D}{\partial t}, \\ \nabla \cdot D &= 0, \\ \nabla \cdot B &= 0. \end{aligned} \tag{4.1}$$

The electric field E, magnetic field B, and the displacement field D are all vector fields. For the sake of simplicity the vector notation is dropped. μ_0 is the magnetic permeability of vacuum. For the equations above, we are considering the special case of a dielectric, non conducting and non-magnetic media. When taking only harmonic fields ($\propto \exp(i\omega t)$) that oscillate with the frequency ω into account, the first two Maxwell's equations simplify to

$$\begin{aligned} \nabla \times E &= -i\omega B \text{ and} \\ \nabla \times B &= i\omega\mu_0 D. \end{aligned} \tag{4.2}$$

The last two equations from 4.1 remain unchanged. Applying a second curl-operator onto the two eqs. 4.2 leads to the vectorial wave equations

$$\begin{aligned} \nabla^2 E + \frac{\omega^2}{c^2}\epsilon E + \nabla\left(E \cdot \frac{\nabla\epsilon}{\epsilon}\right) &= 0 \text{ and} \\ \nabla^2 B + \frac{\omega^2}{c^2}\epsilon B + \left[\frac{\nabla\epsilon}{\epsilon} \times (\nabla \times B)\right] &= 0. \end{aligned} \tag{4.3}$$

c is defined as the speed of light and ϵ is the permittivity which is a material specific function. For non-magnetic materials we can set $\epsilon = \epsilon_0 n^2$, where n is the refractive index

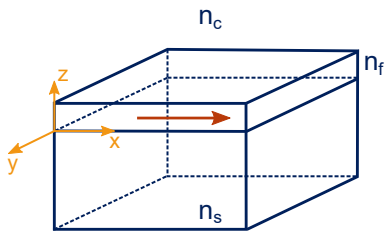

Figure 4.1: Schematic of a planar waveguide. The light is propagating along the x-direction. The light is confined in the film with the refractive index of n_f. In the schematic an asymmetric planar waveguide is depicted which is surrounded by the cover with the refractive index n_c and the substrate with the refractive index n_s.

and ϵ_0 the vacuum permittivity. In the most general case ϵ depends on x, y, z. Hence, the vector wave equations are given in a general formalism that does not impose any additional constraints on the system under consideration. For the example of Ti:LN, we would assume a refractive index profile that depends on y, z (i.e., $n(y, z)$). To obtain a guided mode in an arbitrary refractive index profile, the two wave equations need to be fulfilled. Solving these analytically can be challenging, thus numerical calculations are used to determine the electric field distributions.

Nonetheless, the wave equations can be simplified for certain cases, allowing an analytical approach. One such simple example is the planar waveguide shown in fig. 4.1. For a planar waveguide a film with a higher refractive index n_f is surrounded by a substrate and a cover, both having the lower refractive indices of n_s and n_c. The refractive indices are assumed to be constant along the propagation direction and inbetween the interfaces of different materials, resulting in $\nabla\epsilon = 0$. The wave equations then simplify to the Helmholtz equations

$$\begin{aligned} \Delta E + \epsilon\frac{\omega^2}{c^2}E = 0 \text{ and} \\ \Delta B + \epsilon\frac{\omega^2}{c^2}B = 0. \end{aligned} \tag{4.4}$$

To further simplify the Helmholz equation, it is assumed that $E, B \propto \exp(-i\beta x)$. β is defined as the propagation constant and is linked to the effective refractive index n_{eff} of the mode. Both variables are mode-specific quantities and define the supported waveguide mode. The electric and magnetic field distribution, fulfilling the Helmholz equations with this ansatz, are considered as guided modes of the planar waveguide.

Using a planar waveguide as an example, we can now derive expressions for the two polarization modes, transverse-electric (TE) and transverse-magnetic (TM). From the two Maxwell equations in 4.2 we can derive a set of differential equations (three electric and

three magnetic). Since the derivation for the TM mode is similar to the TE mode, we will just concentrate on the transversal-electric solution. From eq. 4.2 we obtain

$$\begin{aligned}
&\frac{\partial}{\partial y}E_x - \frac{\partial}{\partial z}E_y = -i\omega B_z = i\beta E_y, \\
&\frac{\partial}{\partial x}E_z - \frac{\partial}{\partial z}E_x = -i\omega B_y = i\beta E_z - \frac{\partial}{\partial z}E_x, \\
&\frac{\partial}{\partial z}E_y - \frac{\partial}{\partial y}E_z = -i\omega B_x = \frac{\partial}{\partial z}E_y.
\end{aligned} \tag{4.5}$$

For the derivation of the equations above, we have taken into account that the film is infinitely long in the y-direction, leading to $\frac{\partial}{\partial y}A = 0$, and that the mode is propagating in the x-direction ($\frac{\partial}{\partial x}A = -i\beta A$).

From the equations above we see that we can separate them into two groups. For the transversal-electric (TE) field, the electric field in the y-direction E_y is associated with the magnetic fields B_x and B_z in the x- and z-direction. In case of the transversal-magnetic (TM) field, the magnetic field in the y-direction B_y is associated with the x- and z- direction of the electric fields E_x and E_z. With this simple model we introduced the two polarization modes TE and TM.

In case of a refractive index profile that is not constant as for the planer waveguide (i.e the vectorial wave equation are considered), the solution is more complicated. Even in this case, however, we can approximate *quasi*-TE and *quasi-TM* modes, which is valid for the case of Ti:LN waveguides. For the *quasi*-TE mode we can estimate that:

$$\begin{aligned}
&\left|E_y\right| \gg |E_x|, |E_z| \text{ and} \\
&|B_z| \gg \left|B_y\right|, |B_x|.
\end{aligned} \tag{4.6}$$

In case of the *quasi*-TM mode we can write:

$$\begin{aligned}
&\left|B_y\right| \gg |B_x|, |B_z| \text{ and} \\
&|E_z| \gg \left|E_y\right|, |E_x|.
\end{aligned} \tag{4.7}$$

From the eqs. 4.6 and 4.7 we can see that it is sufficient to concentrate on the E_y and E_z field components for displaying both polarization modes. Since the refractive index profile of the Ti:LN waveguides changes continuously in the y- and z- direction, numerical methods are used to calculate the modes. In order to have a suitable model, it is thus necessary to consider the diffusion process and the crystal properties of lithium niobate in more detail (see chap. 4.1.3).

In this work two different crystal cuts, namely x- and z-cut will be consider. Since z-cut will make up the majority of this work, I will focus on z-cut for this section.

The crystal structure of LN is depicted in fig. 4.2. In case of z-cut the c-axis, shown in fig. 4.2 b), is oriented parallel to the z-axis of the coordinate system introduced for the planar waveguide. Thus, the terms z-axis and c-axis are interchangeable. The z-axis is perpendicular to the surface plane formed by the a_1- and a_2-axis of the crystal. The formalism given here is often found in literature to describe the crystal structure and are not, necessarily equal to the coordinate system x, y, z. In case of lithium niobate, $a_1 = a_2 = a$ and therefore we set the a-axes equal to the x- and y-axes.

Since the c- and a-axis are not symmetric, lithium niobate is a birefringent material. The extraordinary index n_e is parallel to the z-axis. The ordinary index n_o lays in the plane spanned by the x and y-axis, which forms the substrate surface. Fabricated waveguides, are oriented such that the light propagates in x-direction. The two supported polarizations TE (transversal-electric) and TM (transversal-magnetic) are therefore polarized along the y- and z-axis.

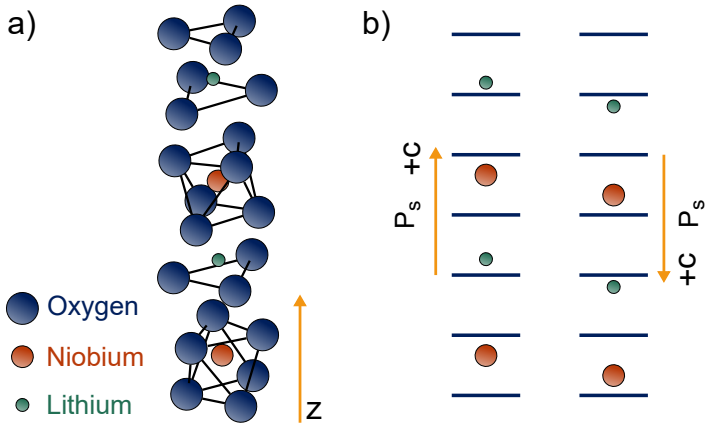

Figure 4.2: Crystal structure of lithium niobate. a) shows the different planes of oxygen atoms and the position of the lithium- and niobium atoms located between the oxygen planes. b) pictures the position in a 2D structure. Poling changes the position of lithium atoms, resulting in the inversion of the spontaneous polarization P_s.

To theoretically describe the supported modes for Ti:LN, simulations based on the finite-element method (FEM) can be used [107]. The refractive index profile introduced by the diffusion of titanium into the crystal can be calculated with the help of the general diffusion equation and the resulting refractive index change depending on the titanium concentration. More details on the diffusion are given in [80] and [102].

An empirical model is used for the simulations, which is consistent with experimental results obtained for previously fabricated Ti:LN waveguides. A 64 nm thick titanium strip with a width of 7 µm and a diffusion time of 8.5 h is used to derive the refractive index

profile [108]. In the diffusion process, the titanium atoms occupy the lattice site of the lithium atoms while the lithium atoms diffuse to the +c-side. The replacement of the lithium atoms locally changes the refractive index. The diffusion changes as a function of crystal orientation, resulting in a directional refractive index change. Therefore, the refractive index profile differs for n_e and n_o. The profile for the two refractive indices can be seen in fig. 4.3 a) and b).

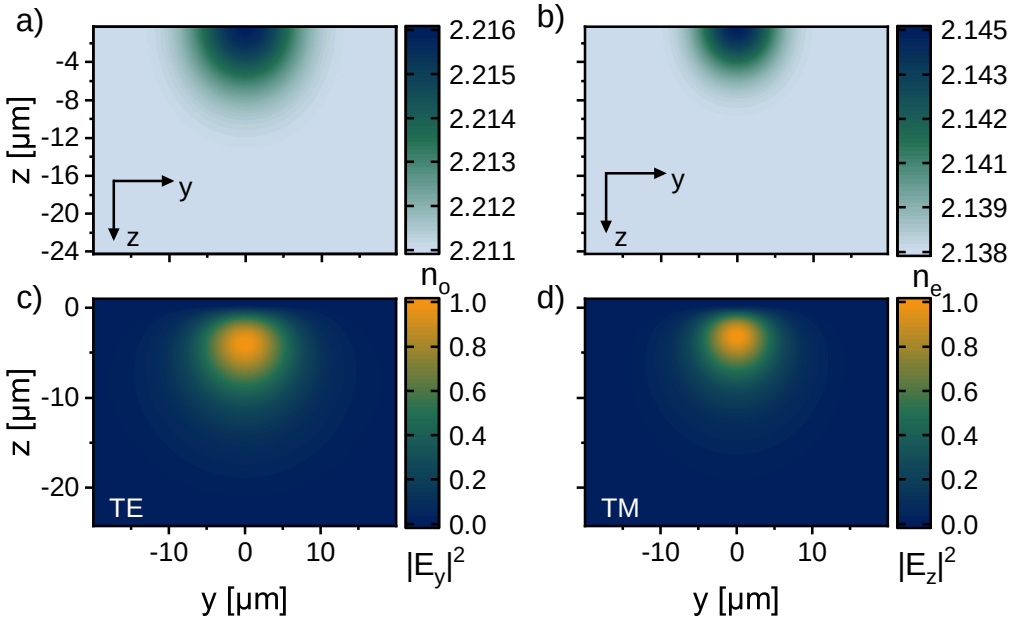

Figure 4.3: Simulated refractive index profile for a) the ordinary (n_o) and b) the extraordinary index (n_e) in Ti:LN. The calculated electric field distribution is shown for both polarizations c) TE and d) TM at 1550 nm.

From the plots in fig. 4.3, it can be observed that the refractive index change is on the order of 10^{-3}, resulting in the weak confinement of the light. With the help of the finite-element-method, the electromagnetic field distribution of the supported waveguide modes can be simulated. The electric field distribution for TE and TM can be seen in fig. 4.3 c) and d). Since for TE the light is polarized parallel to the y-axis (i.e. n_o) and TM parallel to the z-axis (i.e. n_e), a difference in the mode profile can be identified. In case of TM, the light is more strongly confined and located closer to the sample surface. The proximity to the surface can lead to slightly higher propagation losses due to light scattering on surface particles. Nevertheless, due to the guiding in the substrate and the gradual refractive index profile, the propagation losses can be < 0.1 dB/cm at telecom wavelength [82].

Besides achieving low-loss waveguiding, Ti:LN waveguides offer high mode overlap between optical glass fiber and the waveguide mode. A standard optical glass fiber mode has the mode field diameter (MFD) of (10.4 ± 0.5) µm [109], which is comparable with the field distribution shown in fig. 4.3.

Determining the overlap between a standard optical fiber and the waveguide leads to an overlap of 92% and 89% for TE and TM [84]. Additional optimizations can be done by mode manipulation of the waveguide mode [94]. Therefore, additional layers of materials with different refractive indices could be deposited on the sample surface. In chap. 5.2, I will present the measures I have taken to manipulate the Ti:LN mode by depositing a thin film of silicon on top of the waveguide [94].

With the theoretical background on waveguiding in Ti:LN introduced, the fabrication of waveguides can be addressed. While so far the fabrication of Ti:LN waveguides has been carried out by mask lithography at Paderborn University, the fabrication process with a maskless laser lithography has been developed in this work.

4.1.2 Fabrication with Direct Laser Lithography

The fabrication of nano- and micro structures plays a huge role in all types of different fields in physics. Depending on the critical feature size different pattering mechanisms like electron-beam lithography or optical lithography have to be considered. In this work, I have focused on using a maskless laser lithography to pattern various types of integrated components which sizes span over six orders of magnitude, ranging from hundreds of nanometers to several centimeters. The fast and rapid prototyping, offered by direct laser-writing, is ideal for component optimization and flexible circuit design. A list of all the components realized in the scope of this work are given in tab. 4.1. Optical components based on Ti:LN have been well studied in the past [110] and have a long history in Paderborn [85], where they have been fabricated with optical mask lithography. A maskless optical lithography has thus never been used in Paderborn. While Ti:LN been used for classical optics experiments in the past, its application in the context of quantum optics is relatively recent [58, 86].

In the table 4.1 the reader can find cross-links to the individual chapters where more detailed descriptions of the individual fabrication processes are given. Since finding the optimal exposure parameters is similar for all presented devices I will give a detailed overview on this process only in this section.

In case of optical lithography a UV-sensitive photoresist is exposed with UV light. The radiation wavelength of the used light dictates the resolution of the system. In the scope of this work light with a wavelength of 375 nm was used. Depending on the resist, parts of the resist are removed in the developer (positive resist) or withstand the developer while unexposed parts are removed (negative resist). Which resist to pick depends on the application. More information on individual resists chosen can be found in the chapters given in tab. 4.1.

The direct laser writer used for this work utilizes two different write modes, that will be abbreviated with *WM I* and *WM II* in the following.

Table 4.1: Different integrated components presented in this work. The typical feature sizes, the write mode and the chapters, which contain detailed information on the individual fabrication processes, are listed. Depending on the write mode different minimal feature sizes can be achieved.

Integrated devices	Write mode	Typical feature size	Chapter
Waveguides	WM I	Width: 7 µm Length: ≤ 10 cm	4.1.3
Periodic Poling	WM II	Periods: 8 – 21 µm Length: 76 mm	4.2
Elec.-Opt. Modulators	WM I	Electrode Separation: 9 – 15 µm Electrode Length: 15 mm	4.3
Mode-Tapers	WM II	Width: 0 – 3 µm Length: ≤ 1700 µm	5.2
Supercond. Detectors	WM II	Width: 0.6 – 1.4 µm Length: ≤ 6 mm	5.3

The write mode used for each device can be taken from tab. 4.1. The two different write modes use different objectives leading to different spot sizes and therefore different minimal feature sizes. For the WM I, features with sizes ≥ 1 µm can be realized. The use of WM II has the disadvantage of a lower write speed, but in return offers a minimum structure size of 300 nm. To exploit the potential of the system, the thermal treatment of the photoresist, the exposure parameters and the developing process have to be optimized. The exact process parameters can be found in the referenced chapters from tab. 4.1. Since the process of finding the correct exposure parameters is similar for all processes, I will explain the procedure in the following.

For an optimal exposure of the resist, the focus value and the intensity (i.e. dose) of the laser beam have to be optimized. To focus on a sample, the system offers an automatic focus option. In this case a red laser beam, going through the objective on the sample surface, is used. By analyzing the back reflection an optimal focus position is automatically determined. A piezo element is used to fine-tune the optimal focus position. To be in the optimal process window the focus value of the piezo element has to be optimized. The focus value indicates the value, by which the piezo element shifts the objective from the autofocus position. The tuning range for the focus value ranges from −100% to 100% which corespondents to a tuning range of ≈ 80 µm. Depending on the type of resist, its thickness, and the substrate the optimal focus value changes, since all influence the beam shape in the resist. During the exposure the piezo element keeps a constant distance between the resist surface and the objective.

The intensity of the laser beam needs to be optimized additionally to the focus value. The laser power can be tuned up to 70 mW. Since the dose can be varied by the laser output power, the exposure takes place at a constant writing speed. Below a set laser output power of 15 mW the measured power deviates from the set value. Therefore, an acousto-optic

modulator and a set of neutral-density filters can be used to modify the laser intensity below 15 mW. The acousto-optic modulator can be set to intensity values from 20 – 100% in steps of 5%. The laser power can be further reduced to 50%, 25%, 12.5%, 5%, 1% and 0.1% of the initially set laser power by the neutral density filters.

To find the optimal exposure parameters a calibration design can be exposed and developed. A sweep of the parameters can be performed on a single sample. The influence of the focus and laser power can be investigated with the cameras of the same system after developing. Example pictures that show the influence of the laser power and focus are displayed in fig. 4.4 a) and b). In fig. 4.4 c) and d) different test structures are shown that can be used to evaluate the process for dense lines or the minimum feature size of the process. In a_1) an optimal focus value of 5% is pictured. When detuning the focus, the shapes round off and individual structures merge together. This effect can be seen in a_2) where a focus value of 30% is used. The focus value is varied until sharp edges and a small degree of merged shapes are obtained.

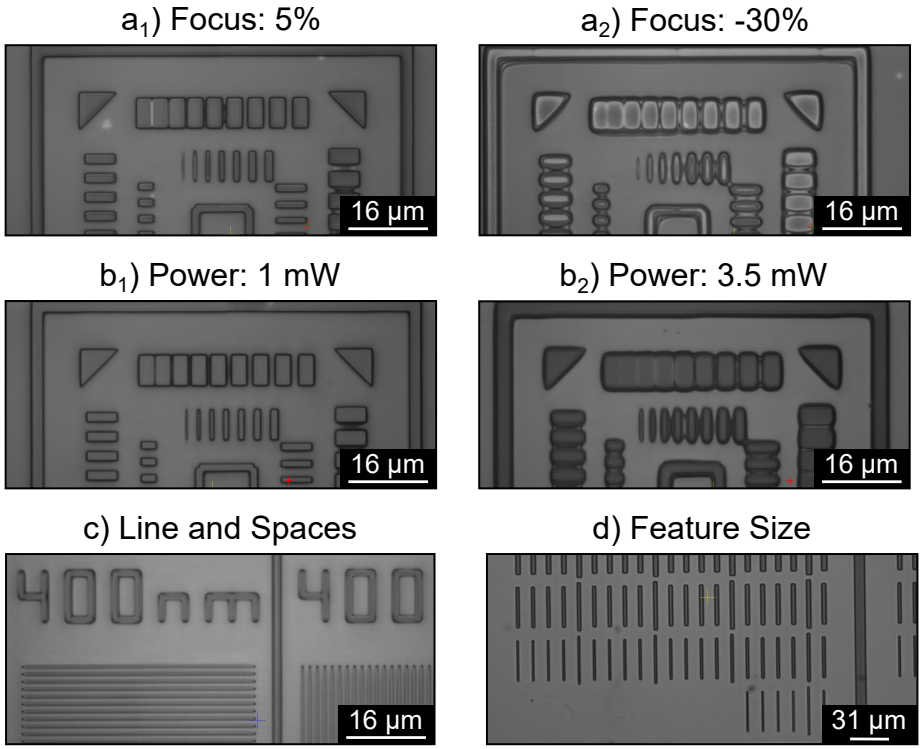

Figure 4.4: Picture of the design for exposure parameter tests. In a) and b) the influence of changing the focus and the laser power is visible. c) displays the test pattern to evaluate dense lines with a width of 0.4 µm and a spacing of 1.2 µm. While a)-c) show pictures of structures patterned with WM II, d) pictures the part of the test design to estimate the minimum feature size, that were exposed with the WM I.

The influence of the laser power can be seen in fig. 4.4 b_1) and b_2). For the given pictures

the test design was exposed with the two power values of 1 mW and 3.5 mW. While the individual structures are nicely separated at a lower laser power, a higher laser power leads to an overexposure of the resist. Since the development rate of the resist depends on the dose which was used for the exposure, structures that are illuminated with a high dose tend to grow in size. If a non sufficient dose is used stitching will be visible and the developed structures will be smaller in size. To find the optimal laser power, the test design is exposed with different values of laser power. For the optimal laser power, the shapes, depicted in fig. 4.4 a) and b), are separated as much as possible without any stitching. The minimum feature size can be evaluated from the example structure in fig. 4.4 d). In order to validate that dense lines can be patterned, the structures pictured in fig. 4.4 c) need to be separated.

The stitching properties of the exposure process is crucial for structures that exceed the write field size of the write mode. When exposing a sample to the UV laser beam the sample drives at a constant speed in the y-direction of the design. The coordinate system used here corresponds to that of the *gds*-design and is not related to the coordinate system introduced for the description of lithium niobate. In the x-direction an acousto-optic deflector is used to deflect the beam and expose a strip. The width of the strip depends on the write mode. For the WM I the width is 150 µm and for the WM II we have a width of 30 µm. Structures that do not exceed this limit in the x-direction are not effected by stitching errors. In the y-direction the size of the structure is only limited by the maximum wafer size which the system can handle. In our case a length of up to 10 cm can be exposed. When preparing a design, the stitching direction should be considered. Therefore, long waveguides should be orientated parallel to the y-direction to reduce stitching errors which may lead to an increase in propagation losses.

For each individual combination of photoresist and substrate an optimal focus value and laser power has to be determined. When fabricating waveguides, periodic poling and electrodes on lithium niobate, different resists and different resist thicknesses will be used for each process. The optimized parameters will be listed in each of the three section below.

4.1.3 Fabrication of Titanium In-Diffused Waveguides

Fabrication Summary: To realize waveguides in lithium niobate by metal in-diffusion an 82 nm thick layer of titanium is deposited on the $-c$-surface. The waveguide is patterned into a photoresist with optical lithography. With a wet etching process, titanium stripes of 7 µm width remaining on the sample. In the last step the titanium is diffused into the crystal. To do so, the sample is heated up to 1060 °C in an oxygen-rich environment. The temperature is kept constant for 8.5 h. Due to the high temperature the titanium atoms diffuse into the underlying crystal. A schematic of the fabrication process is depicted in fig. 4.5. When diffusing into the crystal, the titanium atoms replace the lithium atoms. The lithium atoms diffuse to the $+c$-side and accumulate there, which will be relevant when considering periodic poling for quasi-phase matching (see chap. 4.2).

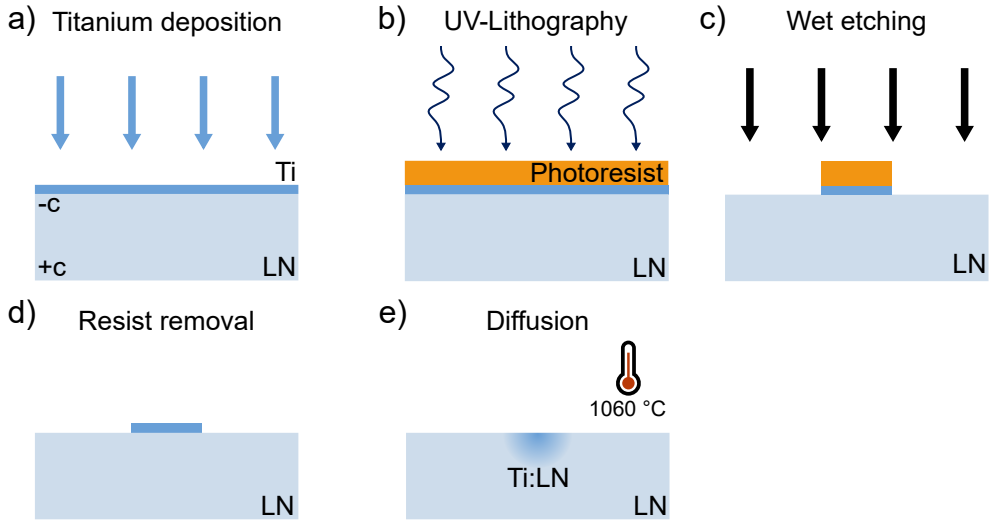

Figure 4.5: Fabrication of titanium in-diffused waveguides. In a) titanium (Ti) is deposited on z-cut lithium niobate. With optical lithography a waveguide is patterned in the photoresist (see b)), followed by the wet etching process pictured in c), to structure the Ti according to the resist. In d) the residuals are removed and the titanium is in-diffused at 1060 °C as shown in e).

Before the deposition of titanium, the lithium niobate samples have to be properly cleaned. All cleaning processes are carried out in an ultrasonic bath at 40 °C. In a first step acetone and isopropanol are used to remove the residual photoresist that was used as a protective layer on the sample surface. In order to reduce the surface tension, the samples are cleaned in a ultrasonic bath with a cleaning lye. To remove all remaining organic residuals an etching solution based on ammonia and hydrogen peroxide is used.

The deposition of the titanium is done with an electron-beam evaporater. The base pressure

for the deposition is on the order of 10^{-7} Torr. An 82 nm thick layer of titanium, with a deposition rate of ≈ 10 Å/s, is deposited on the sample surface. A schematic of the sample at this point of fabrication can be seen in fig. 4.5 a).

For the optical lithography a photoresist is spin-coated on the sample surface. For the fabrication of the waveguides the negative resist *AZ nLof 2020* is used. The resist is spin coated with 6000 rpm for 3 s and a ramp of 5 s. This results in a resist thickness of 0.9 µm as was verified with a profilometer. To remove the residual solvents in the resist, the sample is heated up in a convection oven at 110°*C* for 15 min. Normally the softbake of resists is done on a hot plate, but since LN is pyroelectric a rapid temperature change of the sample could lead to pyroelectric damages of the sample.

The temperature and baking time of a resist is crucial for its performance in optical lithography [111]. In case of a negative resist the exposure and an additional post-exposure bake (PEB) leads to a linking of short phenolic resin molecules to longer chains [111]. These so-called cross-links in the resist, making it resistant against the developer. For high temperatures (> 120 °C depending on the resist) and longer baking times the cross-links are getting stronger. This results in a cross-linking of the resist in areas that have not been exposed to UV light. Therefore, structures are rounded off and increased in size. The influence can be seen in fig. 4.6. The pictures are taken for equal exposure parameters and the duration of the PEB was changed. The experiments were done on silicon since a hotplate could be used to verify the convection oven parameters. Comparing first the structures on a hot plate for a PEB time of a) 45 s, b) 60 s and c) 75 s, a rounding of the structures, an enlargement and the resulting merging of the structures at 75 s of PEB time, can be observed. In case of a PEB time of 45 s the stitching of the write fields and the development of exposed structures, due to weak cross-links can be recognized. Based on these results a PEB time of 60 s was picked for the hotplate. The results obtained for the hotplate were used as a reference for the process optimization in the convection oven. With a PEB time of 15 min in the confection oven (see fig. 4.6 d)) similar results as shown for the hotplate and 60 s can be achieved. For the softbake prior to the exposure the same time as for the PEB was taken.

After spin coating and softbake the lithography step can be performed (see. fig. 4.5 b)). The optimized exposure parameters for *AZ nLof 2020* on titanium can be taken from tab. 4.2. The waveguide design was exposed with WM I. The design was made so that the waveguides run along the y-direction of the system so that they are not affected by stiching. For a straight waveguide sample 25 groups of 3 waveguides with a separation of 100 µm were patterned into the resist. The separation of individual groups is 200 µm. The width of the waveguides is set to 7 µm.

After the exposure, a PEB is performed at 110 °C for 15 min to strengthen the cross-links in the resist. As a developer *AZ 726 MIF* is used. The developer is diluted with water in a ratio of 85:15. This results in a slower developing time and an easier process control. The development time was set to a fixed value of 30 s. Since the titanium will be etched, an additional hardbake step at 120 °C for 15 min is done. The additional baking step does not change the structure but increases the etch resistance of the resist.

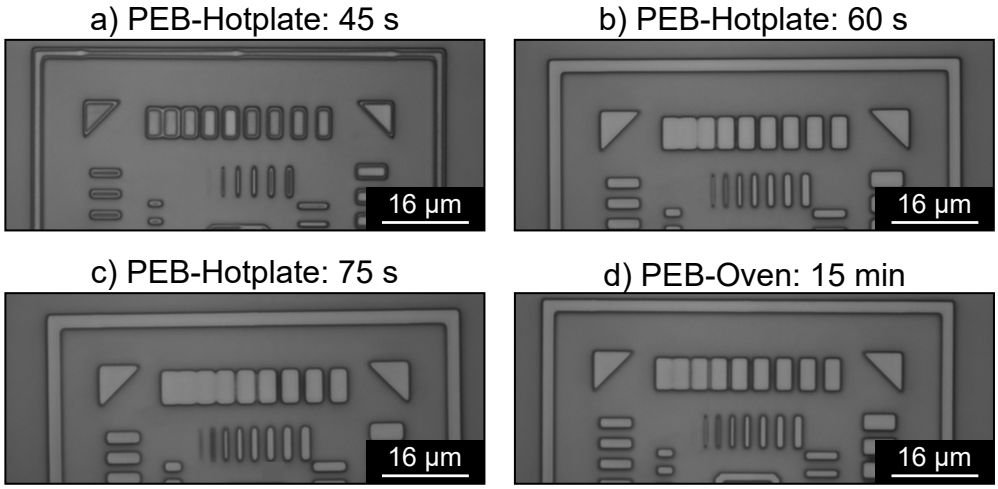

Figure 4.6: Results from the test for the optimal PEB time for *AZ nLof 2020* on silicon. While for a) - c) a hotplate was used, a convection oven was utilized for d). The effect of a too short/long PEB can be seen in a) and c). The similar result for hotplate and oven can be taken from comparing b) and d).

The wet etching process shown in fig. 4.5 c) is done based on the same etching solution used for the cleaning procedure. To increase the etching time ethylenediaminetetraacetic acid (EDTA) is added. The etching is done in a water bath at 40 °C. The process is stopped by rinsing the sample with water, after the titanium is fully etched away indicated by the returning transparency of lithium niobate. Etching solution and water for stopping the etching process are kept both at 40 °C to reduce pyroelectric effects. The etching time can vary from sample to sample. The returning transparency indicates the end of the etching process which is after ≈ 7.5 min.

Table 4.2: Lithography parameters for the negative photoresist *AZ nLof 2020* on titanium with the WM I.

Photoresist	Focus	Power	Filter
AZ nLof 2020	−12%	42 mW	100%

After etching, the residual photoresist has to be removed from the remaining titanium stripes. Therefore, *TechniStrip NI555* is used as a stripper. The stripper is heated up to 70 °C for its optimal performance. In a ultrasonic bath the remaining resist is then completely dissolved. In a last step isopropanol is used to remove any remains from the *TechniStrip NI555*. With this a 7 µm wide titanium stripe as pictured in fig. 4.5 d) remains on the lithium niobate sample.

For the realization of a waveguide the titanium is in-diffused into the lithium niobate in a diffusion oven. The sample is heated to 1060 °C. The temperature is kept constant for 8.5 h (see fig. 4.5 e)). The diffusion is performed under an oxygen environment. In order to

be able to couple light into the waveguide from the end facets, these have to be polished in a last step.

In a first characterization step, we can determine the propagation losses of the waveguides. The method from Regener et al.[81] is well suited for calculating the losses of a low-finesse waveguide resonator. This non-destructive, polarization-sensitive methods enables the determination of the propagation losses by measuring the Fabry-Pérot resonances formed by the two end facets of the waveguide chip with the reflectivity R. By tuning the temperature of the chip, the sample length changes slightly, resulting in a shift of the -PFabry-Pérot resonance. The arising change in the output intensity can be measured with a photo diode. From the contrast K of the curve the losses can be determined. A big advantage of this method is that it is independent of the in- and out-coupling efficiency. Besides the temperature one can also vary the input wavelength to determine the propagation losses α. The equation to calculate the losses is given by

$$\alpha \propto \frac{4.34}{L}(\ln R + \ln 2 - \ln K). \tag{4.8}$$

L is defined as the length of the sample. Example results for the propagation losses of 45 waveguides in the center of a sample can be seen for the polarizations of TE and TM in fig. 4.7. For both polarizations, propagation losses below < 0.1 dB/cm can be achieved, which is considered the standard for Ti:LN waveguides [82]. This demonstrates that low-loss waveguides can be realized with maskless optical lithography.

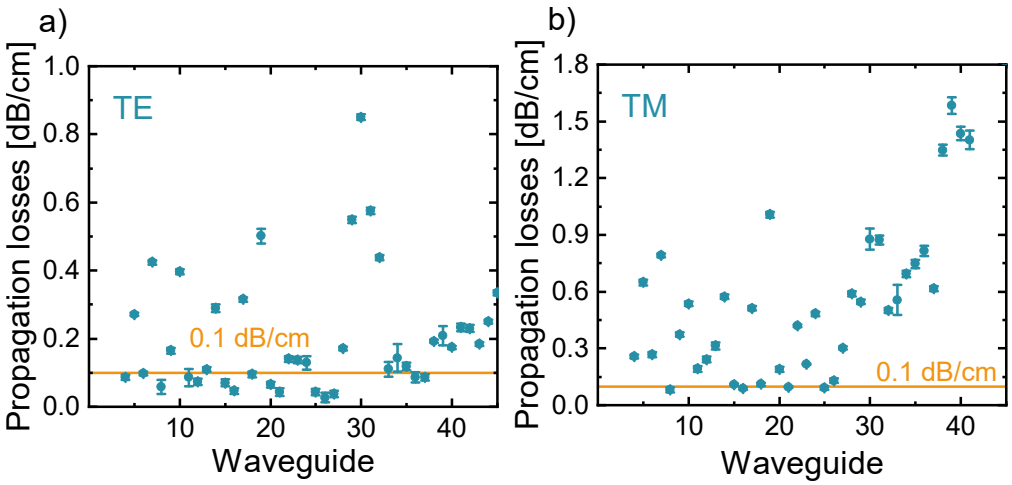

Figure 4.7: Propagation losses for 7 µm straight waveguides for both polarization modes a) TE and b) TM. It can be seen that losses below 0.1 dB/cm can be achieved.

Resist inhomogeneities and imperfections arising from the polishing are more likely towards the edge of the sample. These imperfections lead to higher propagation losses, which are not attributed to the exposure process with maskless lithography. For this reason, the waveguide groups, which are in proximity to the edge are not included in the plots.

The average higher propagation losses for TM indicate the influence of the stronger confinement and the closer proximity to the sample surface as discussed in chap. 4.1.1. The close proximity to the surface increases the scattering of guided light on impurities on the sample surface. Especially after the polishing procedure, residuals of the polishing solution can remain on the sample surface. Proper cleaning is thus essential for the good performance of the waveguides. The exemplary sample used for the data shown in fig. 4.7 was characterized twice. In between the two measurements the sample was cleaned with a lye solution. This decreased the losses for TM and TE by 0.4 dB/cm and 0.2 dB/cm on average, showing the necessity of proper sample cleaning.

Additional loss sources are inhomogenities in the waveguide structure or scratches on the sample surface leading to an increased scattering. In such cases, a drastic increases in the measured losses for small amount of waveguides is a indication for this. The scratches can also arise from residuals of the polishing solution on the sample surface. Scratches on the end-facet due to the polishing can lead to scattering of the light at the end-facet which can be also a source of loss. Despite the variety of factors that influence the propagation losses, I demonstrated that low-loss waveguides can be manufactured with direct laser writing.

4.1.4 Fabrication of Passive Components

With low-loss waveguides as the foundation of our toolbox, functional passive components like directional couplers can be fabricated. For these, two waveguides are brought into close proximity. The evanescent field of the waveguide mode overlaps with the adjacent waveguide mode, resulting in an exchange of energy between the two waveguide modes. The amount of energy transfered from one waveguide to the other depends on the length of the coupling regime and the effective refractive index difference of the two waveguides. For the theoretical description of these integrated beam splitters the couple mode theory is required.

The theory behind the coupled mode equations for a direction coupler and the derivation of them can be found in [112]. Here, I start with the coupled mode equation for a directional waveguide coupler in the x-direction:

$$\begin{aligned} \frac{\partial A_1(x)}{\partial x} &= -i\kappa_{12} A_2(x) \exp(i\Delta\beta x) \text{ and} \\ \frac{\partial A_2(x)}{\partial x} &= -i\kappa_{21}^* A_1(x) \exp(-i\Delta\beta x). \end{aligned} \tag{4.9}$$

$A_1(x)$ and $A_2(x)$ are the coupling amplitudes of the two waveguide modes, which depend on the position in the directional coupler. Since they are varying in the propagation direction x, this can be interpreted as an energy transfer between the two modes. $\Delta\beta = \beta_1 - \beta_2$ is the difference between the propagation constants of the two individual waveguides. The coupling constants κ_{12} and κ_{21}^* quantify the strength of the coupling. For a directional

coupler the coupling constants are related to

$$\begin{aligned} \kappa_{12} &\propto \iint E_2(y,z)\Delta n_1^2(y,z)E_1^*(y,z)\ \mathrm{d}y\mathrm{d}z \text{ and} \\ \kappa_{21} &\propto \iint E_1(y,z)\Delta n_2^2(y,z)E_2^*(y,z)\ \mathrm{d}y\mathrm{d}z. \end{aligned} \tag{4.10}$$

The two equations above take the form of an overlap integral between the spatial field distributions of the two waveguide modes $E_1(y,z)$ and $E_2(y,z)$. Since the coupled mode theory is in principle a perturbation theory, the presence of the second waveguide and its refractive index profile is treated as a perturbation, which is quantified with $\Delta n_{1,2}^2 = n_{1,2}^2(y,z) - n_{2,1}^2(y,z)$. From eq. 4.10 we can see that an decreasing distance between the waveguides will increase the coupling strength, since the overlap between the coupling fields will increase. The power $P_{1,2}$ in both modes can be calculated by

$$P_{1,2}(x) = \left|A_{1,2}A_{1,2}^*\right|^2. \tag{4.11}$$

When we are considering the symmetric case (i.e identical waveguides $\Delta\beta = 0$) and that all the starting power is in the first waveguide, the power in the two waveguides is given by

$$\begin{aligned} P_1(x) &= |A_0|^2 \cos^2(\kappa x) \text{ and} \\ P_2(x) &= |A_0|^2 \sin^2(\kappa x) \end{aligned} \tag{4.12}$$

where $\kappa = \sqrt{\kappa_{12}\kappa_{21}}$. The coupling length $L_c = \pi/2\kappa$ defines the length required to transfer the complete power into the adjacent waveguide.

For the experimental realization of a directional coupler two waveguides that are separated by 13 µm from center to center are fabricated. A schematic of a directional coupler is shown in fig. 4.8. The length of the region where they are in close proximity (i.e. the coupling regime), is varied from $1 - 10$ mm in 1 mm steps. In order to bring the waveguides in close proximity or to stop them from coupling, bends with a length of 4.5 mm are used. When the two waveguides are separated they have a distance of 127 µm to match the distance of the fiber cores in multi-mode glass pigtail. The entire coupler is automatically designed with a *Python* script. The bends are approximated by a cosine function decomposed with a mesh size of 30 µm along the bend length of 4.5 mm.

To evaluate the behavior of the directional coupler, the setup shown in fig. 4.9 b) is used. A laser source at 1550 nm is coupled into the waveguide. With a half-wave plate and a rotatable polarization filter, TE and TM can be separately measured. For the out coupling a lens with an NA of 0.25 is used. The mode can be imaged with an near-infrared camera. Exemplary mode images for the TE and TM mode are pictured in fig. 4.9 b). The mode images show the smaller mode size of the TM mode, which was previously discussed.

When coupling into one of the two waveguides the end-facet of the output is imaged. Since the two output ports light up the position out coupling lens needs to be changed to image

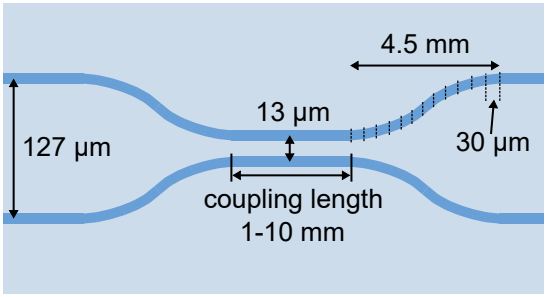

Figure 4.8: Design of a directional coupler. Away from the coupling regime the two waveguides are separated by 127 µm. The bends are approximated by a cosine function which is decomposed with a mesh size of 30 µm.

the two output ports individually. Since there are two possible inputs, the same coupler can be characterized twice (once from each input). As a result we obtain two coupling ratios for one coupler length.

In order to obtain the power in one arm, the intensity measured in each pixel of the mode image is summed up. When normalizing on the total power in both arms of the coupler the results shown in fig. 4.9 a) are obtained. For both polarizations we see a change in the output power of one arm when changing the coupler length. The data matches well with the sine-square fit functions which is expected from eq. 4.12. The errors given in the graph are calculated from the difference in the obtained output power, when changing the input of the coupler. If we assume a perfect coupler (i.e. no losses), the input port should not have an influence on the splitting ratio of the coupler. Nevertheless, we see that the measured splitting ratio is different for the two inputs. This can be explained by additional propagation losses in only one of the output arms. Losses in the input arm would not change the measured splitting ratio of the coupler. When considering the mean difference we obtain an average deviation of ±3%.

The data shows that for both polarizations there is almost a complete power transfer to the adjacent waveguide. For the TE polarization a minimal power of $(1.9 \pm 0.2)\%$ remained in the input waveguide. For TM the power extinction in the input waveguide is even higher with $(0.8 \pm 0.2)\%$. The results indicate that the coupling modes have equal propagation constants, since only for a symmetric coupler ($\Delta\beta = 0$) a full power transfer can be achieved. An asymmetry in the coupler can result from fabrication imperfections such as variations in the waveguide width in the coupling region. If there is a difference in the propagation constant of the two waveguides the maximum power that is transferred to the adjacent waveguide is reduced. Since the propagation constant depends on the wavelength-dependent refractive index profile of the waveguide, the directional coupler has a wavelength dependence that is not investigated here.

Comparing the two fits obtained from the data, a different periodicity for TE and TM can be observed. Since the coupling constant κ dictates how fast the power oscillates between the two waveguides, it is clear that TE and TM have different coupling constants.

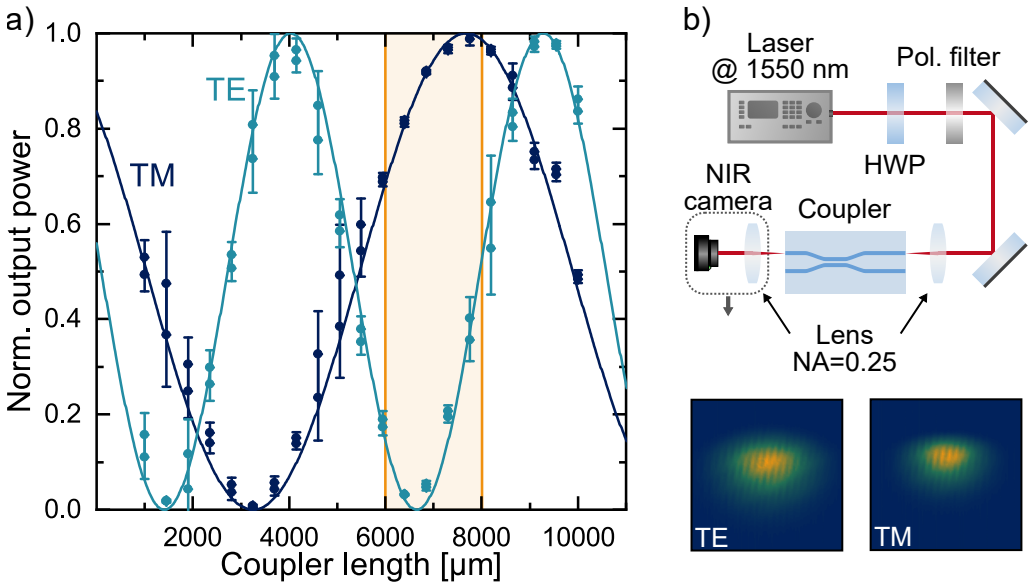

Figure 4.9: Results and setup for a directional coupler in Ti:LN. a) shows the measured Power in the bar waveguide. b) displays the setup used for taking the mode images and shows example mode images for the two polarization modes. A half-wave plate (HWP) and a polarization filter (Pol. filter) is used to change between TE and TM. A near-infrared (NIR) camera is used for mode imaging. The highlighted area in a) is the coupling region interesting for utilizing a PBS, which will later be relevant for the weak-field homodyne chip.

The difference comes from the different spatial mode distribution of the two polarization modes. Since eq. 4.10 states that the coupling constant is proportional to the spatial mode overlap, the coupling is weaker for TM due to its slightly stronger confinement. The weaker coupling is also evident in the data.

The difference in the coupling constant can be utilized for the realization of an integrated polarizing beam splitter (PBS). The fabrication of such will be necessary for the integration of a homodyne detector. Therefore, I highlighted the area in the graph where the highest polarization splitting is measured for the sample. For the following homodyne chip the coupler length was varied from 6000 – 8000 µm in 15 steps. The homodyne chip will be later used to perform a partially integrated homodyne experiment. On the chip will be an integrated phase shifter, polarization converter and a polarizing beam splitter. The polarization converter (PC) will be characterized in chap. 4.3.3. A picture of the layout of the homodyne chip and the fabrication parameters can be found in chap. A.4.

The PBS is characterized with the setup shown in fig. 4.9 b). Instead of the lens with the NA of 0.25, a high NA objective (NA=0.90) is used to increase the resolution of the mode images. 1550 nm is used as an input wavelength. The evaluation of the mode images was done as previously described. The mode images are taken at equal camera settings and

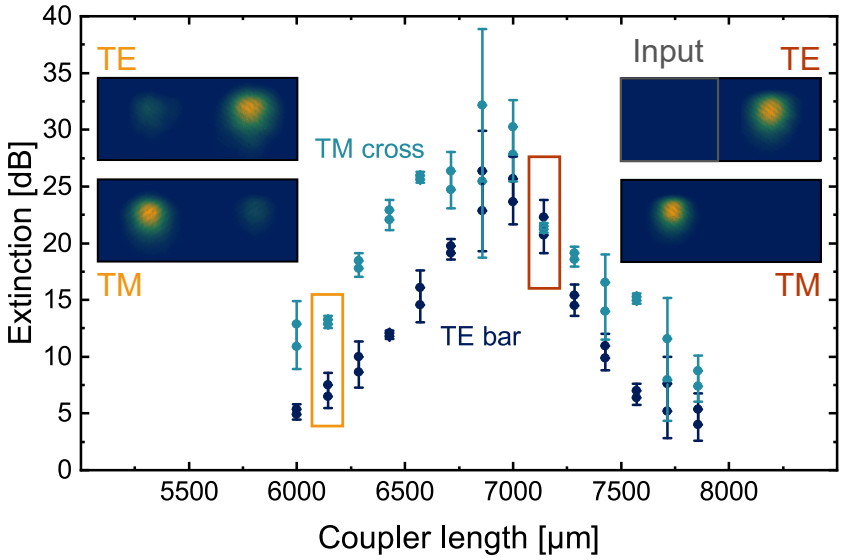

Figure 4.10: Characterization of the integrated PBS performance. An extinction over 20 dB in both polarizations for coupler lengths ranging from 6500 – 7250 µm can be achieved. In the insets the mode images taken for the highlighted coupler structures are displayed. For all given mode images, the input waveguide is located in the left part of the mode images, which is highlighted in a mode image. For each structure there are two data points for changing the input waveguide of the directional coupler.

from the total intensity in the mode images the extinction of the two polarization modes in the opposite arms of the coupler can be calculated.

The results are shown in fig. 4.10. With the bar waveguide I refer to the waveguide which is used as an input waveguide. The cross waveguide is the adjacent waveguide to which the light can couple. In the plot four example mode images are given. For the orange highlighted coupler an extinction above 5 and 12 dB for TE and TM is achieved. In the mode images it is evident that the TE polarization couples to the adjacent waveguide of the input (i.e. cross waveguide) while the TM mode couples into the input waveguide (i.e. bar waveguide). In case of the orange highlighted structure, it is visible that light still remains in the unwanted arm of the PBS.

When changing the coupler length an increase of the extinction in the two output ports of the PBS is visible. In red a coupler with an extinction greater than 20 dB for both polarizations is highlighted. The mode images for this case are included in the plot. It is visible that a high proportion of the TE polarized light couples to the cross waveguide, while the TM polarized light remains in the bar waveguide. The in red highlighted structure will later be used for the homodyne experiment presented in chap. 6.

In summary, I have shown that with direct laser lithography we are able to fabricate benchmark Ti:LN waveguides with propagation losses < 0.1 dB/cm. With this we are

able to fabricate directional couplers. Due to the phase-mismatch between TE and TM ($\beta_{TE} \neq \beta_{TM}$) we are able to fabricate an integrated PBS, which we will utilize for the homodyne experiments. In the next section, which deals with nonlinear processes in lithium niobate, the phase-mismatch between coupling modes is discussed in more detail. Since the waveguides will later be used in a quantum optical homodyne experiment, it is worthwhile to compare them with previous work in this context. The demonstration of an integrated Hong-Ou-Mandel experiment by Luo et al. [86] is to date the most complicated quantum optical experiment performed in Ti:LN. The propagation losses and achieved performance for the directional coupler are comparable to the results mentioned in [86]. This comparison shows that the structures realized with the maskless lithography can be used in the context of integrated quantum optics.

Besides the use of a directional coupler as a PBS, we can configure it as balanced beam splitter. In the work from Jan Philipp Höpker [113] the results obtained in the scope of my work were used to fabricate an integrated interferometer based on balanced beam splitters. The interferometer was used to perform photon subtraction experiments to manipulate quantum states and reveal quantum properties of light.

4.2 Nonlinear Processes in Lithium Niobate

For any optical quantum information protocol, quantum states like single photons, squeezed states or even more complex quantum states are required [33]. Creating these states can be quite a challenge and is a problem in current research. While multiple approaches are possible, we concentrate on the generation of squeezed states and single photons with the help of nonlinear crystals. In the following, I will be describing the theoretical framework for the generation of said states. I will then discuss the fabrication of lithium niobate chips, which take advantage of the nonlinear properties of lithium niobate to generate single photons.

4.2.1 Nonlinear Material Polarization

To generate single photons, a process called spontaneous parametric down conversion (SPDC) can be used. In this process a strong pump field propagates through a nonlinear crystal. Due to the nonlinear interaction a decay of a pump photon into two photons with a longer wavelength can occur. This process takes place on a probabilistic basis and by this distinguishes itself from the single-photon generation with on-demand sources like quantum dots. If both generated photons have the same wavelength we call them degenerate. The possible wavelengths are dictated by energy and momentum conservation. Even though a quantum mechanical formalism is required to describe SPDC, it is sensible to first look at the reverse process of sum-frequency generation (SFG) or second harmonic generation (SHG). These two processes can be described classically and will be later used in

experiments to quantify the quality of the periodic poling in lithium niobate. The presented theoretical background is taken from [114] and [115].

The origin of nonlinear optics lies in the description of the interaction between light and matter in case of intense electromagnetic fields. When a field with the frequency ω interacts with the charges in the medium, this can be described as a classical harmonic oscillator. In theory the electron is located in the harmonic potential of the atomic core. If the strength of the electromagnetic field increases, the harmonic oscillator, formed by the electron-atom interaction, starts to be anharmonic, i.e responding nonlinearly to the incoming field. To explain this in a more quantitative way, one can look at the wave equation for an electromagnetic wave propagating through a non-magnetic material without external charges and no electrical current:

$$\nabla^2 \boldsymbol{E} + \frac{1}{c^2}\frac{\partial^2 \boldsymbol{E}}{\partial t^2} = \frac{1}{\epsilon_0 c^2}\frac{\partial^2 \boldsymbol{P}}{\partial t^2}. \tag{4.13}$$

The material polarization P induced by the incoming electromagnetic field can now be split into a linear and non-linear term P^l and P^{nl}. The linear term is responsible for the *normal* prorogation through the medium and is linked to the standard linear refractive index. SPDC and SHG are processes included in the nonlinear polarization P^{nl}. Both processes are a three-wave mixing process and are therefore included in the second order nonlinear term

$$P_i^{(2)}(t) = \epsilon_0 \sum_j \sum_k \chi_{ijk}^{(2)} E_j(t) E_k(t) \tag{4.14}$$

with $\{i, j, k\} = \{x, y, z\}$ being the crystal axis of the nonlinear crystal. The tensor $\chi_{ijk}^{(2)}$ is called the second order nonlinear susceptibility and quantifies the interaction strength of the coupling electric fields $E_j(t)$ and $E_k(t)$. The electric fields can be written as a composition of $E_{j,k}(\omega_n)$ oscillating at the frequency ω_n:

$$E_{j,k}(t) = \sum_n E_{j,k}(\omega_n) \exp(-i\omega_n t). \tag{4.15}$$

We can express the polarization in a similar way:

$$P_i(t) = \sum_n P_i(\omega_n) \exp(-i\omega_n t). \tag{4.16}$$

In both cases the sum is carried out over positive and negative n. With $E(-\omega_n) = E(\omega_n)^*$ and $\omega_{-n} = -\omega_n$, $E(t)$ is given as a general expression for an electric field. With this convention we can rewrite eq. 4.14 as

$$P_i^{(2)}(\omega_n + \omega_m) = \epsilon_0 \sum_{jk} \sum_{nm} \chi_{ijk}^{(2)} E_j(\omega_n) E_k(\omega_m). \tag{4.17}$$

The sum over n, m is done for both positive and negative values. The nonlinear polarization

$P_i^{(2)}(\omega_n+\omega_m)$ acts as a source term for an electromagnetic field with the frequency $\omega_n+\omega_m$. The nonlinear susceptibility is a material-dependent tensor whose tensor elements depend on the symmetry of the nonlinear crystal. In literature it is often introduced as

$$d_{i,j,k} = \frac{1}{2}\chi^{(2)}_{i,j,k}. \tag{4.18}$$

The indices j and k can be interchanged when $\chi^{(2)}_{i,j,k}$ is frequency independent and the Kleinman symmetry is valid [115]. Then j and k can be replaced with a single index l. The notation for l is according to

j,k	11	22	33	23, 32	31,13	12,21
l	1	2	3	4	5	6

. (4.19)

The indicies of $\{1,2,3\}$ correspond to the crystal axis $\{x,y,z\}$. With this we can rewrite eq. 4.17 for the specific case of an electromagnetic field of two frequencies ω_1, ω_2:

$$\begin{bmatrix} P_x^{(2)}(\omega_1+\omega_2) \\ P_y^{(2)}(\omega_1+\omega_2) \\ P_z^{(2)}(\omega_1+\omega_2) \end{bmatrix} = 4\epsilon_0 \begin{bmatrix} d_{11} & d_{21} & d_{31} \\ d_{12} & d_{22} & d_{32} \\ d_{13} & d_{23} & d_{33} \\ d_{14} & d_{24} & d_{34} \\ d_{15} & d_{25} & d_{35} \\ d_{16} & d_{26} & d_{36} \end{bmatrix}^{\mathrm{T}} \cdot \begin{bmatrix} E_x(\omega_1)E_x(\omega_2) \\ E_y(\omega_1)E_y(\omega_2) \\ E_z(\omega_1)E_z(\omega_2) \\ E_y(\omega_1)E_z(\omega_2)+E_z(\omega_1)E_y(\omega_2) \\ E_x(\omega_1)E_z(\omega_2)+E_z(\omega_1)E_x(\omega_2) \\ E_x(\omega_1)E_y(\omega_2)+E_y(\omega_1)E_x(\omega_2) \end{bmatrix}. \tag{4.20}$$

In case of eq. 4.20 we are already considering the special case of sum-frequency generation, where ω_1 and ω_2 are summed together. When the input field have the same frequency $\omega_1 = \omega_2 = \omega_p$, we talk of second harmonic generation.

For the purpose of this work lithium niobate is used as nonlinear material. It belongs to the point group 3m. Due to its crystal symmetry the tensor d_{il} can be simplified to [116]:

$$\begin{bmatrix} 0 & 0 & 0 & 0 & d_{31} & -d_{22} \\ -d_{22} & d_{22} & 0 & d_{31} & 0 & 0 \\ d_{31} & d_{31} & d_{33} & 0 & 0 & 0 \end{bmatrix}. \tag{4.21}$$

4.2.2 Second Harmonic Generation and its Phase Matching in Lithium Niobate

The properties of the later fabricated lithium niobate chips are characterized with nonlinear measurements. In this work we will characterize the fabricated poling periods with SHG measurements. Generally, we have to differentiate between type-0, type-I and type-II SHG. For type-0, input and output signal have the same polarization. Type-I has orthogonal polarization for input and output and in case of type-II, the two input photons have different polarization. In this work I will concentrate on a type-II SHG process.

In case of type-II SHG, two light beams of the same frequency ω_p with orthogonal polarization (TE and TM) couple and generate a signal at twice the frequency in TE polarization. This process is schematically pictured in fig. 4.11 a). d_{eff} refers to a value of d for a fixed geometry. From eq. 4.17 and eq. 4.21, we can write the nonlinear polarization in the y-direction as

$$\begin{aligned} P_y^{(2)}(2\omega_p) &= 4\epsilon_0 d_{31}[E_y(\omega_1)E_z(\omega_2) + E_z(\omega_1)E_y(\omega_2)] \\ &= 8\epsilon_0 d_{31}E_z(\omega_p)E_y(\omega_p) \end{aligned} \tag{4.22}$$

where $P_y^{(2)}(2\omega_p)$ acts as a source term for a field with twice the pump frequency ω_p. The input fields are given in orthogonal polarization $E_y(\omega_p)$ and $E_z(\omega_p)$.

For degenerate SPDC as the reverse process, a single photon decays into two photons with half the frequency. The two photons generated are called signal and idler. The signal and idler photons can be treated as a source of single photons or squeezed light. The Hamiltonian $\hat{H}$ that describes the interaction for the degenerate case is given by

$$\hat{H} = i\hbar(\eta^* \hat{a}^2 - \eta \hat{a}^{\dagger 2}) \tag{4.23}$$

where $\hat{a}$ and $\hat{a}^\dagger$ are the annihilation and creation operator of the signal and idler photon. The state generated with this Hamiltonian is a single-mode squeezed state. Since the annihilation and creation operator are squared, it is evident that always an even number of photons is generated. η can be considered as the strength of the interaction and is related to the strength of the pump field and the nonlinear susceptibility. More details on the quantum mechanical description of this process can be found in [12].

It was already mentioned that for all nonlinear process, energy conservation has to be fulfilled. A second condition is given by the conservation of momentum. In case of waveguide modes, we often talk of the phase-matching condition of the coupling modes. To derive an expression for the phase-matching, the spatial distribution of the electric fields $E(\omega_n)$ can be expressed by

$$E(\omega_n)(r) = A_n \exp(\mathrm{i}k_n \cdot r), \tag{4.24}$$

where A_n is the spatially slowly varying amplitude and k_n the wave vector of the mode with frequency ω_n. The propagation of an intense light beam through the nonlinear material, as depicted in fig. 4.11 a), follows the coupled-amplitude equation:

$$\frac{\mathrm{d}A_3}{\mathrm{d}x} = \frac{2\mathrm{i}d_{\text{eff}}\omega_3}{k_3 c^2} A_1 A_2 \exp(\mathrm{i}\Delta k x). \tag{4.25}$$

Similar expressions can be derived for A_1 and A_2, being the amplitude of the pump photons. Since in an experiment the amplitudes of A_1 and A_2 are much higher than that of the nonlinear signal A_3, it can be assumed that $\frac{\mathrm{d}A_{1,2}}{\mathrm{d}x} = 0$. Δk denotes the phase mismatched

between the coupling modes and is defined by

$$\Delta k = k_1 + k_2 - k_3 = \frac{n_1\omega_1}{c} + \frac{n_2\omega_2}{c} - \frac{n_3\omega_3}{c} \tag{4.26}$$

and accounts for the momentum conservation of the nonlinear process. With the constant amplitudes of A_1 and A_2 in the x-direction, the differential equation for A_3 can be solved by integrating over x. For a propagation distance of the waveguide length L, the amplitude is given by

$$A_3 = \int_0^L \frac{2\mathrm{i}d_{\mathrm{eff}}\omega_3}{k_3c^2} A_1A_2 \exp(\mathrm{i}\Delta kx)\ \mathrm{d}x. \tag{4.27}$$

In the experiment we measure the intensity I_3 which is proportional to $|A_3|^2$. With the refractive indices of the coupling modes $n_{1,2,3}$, the intensity of the third light wave can be written as [115]

$$I_3 = \frac{8d_{\mathrm{eff}}^2\omega_3^2 I_1I_2}{n_1n_2n_3\epsilon_0c^2} L^2\ \mathrm{sinc}^2\ \frac{\Delta kL}{2}. \tag{4.28}$$

In general, Δk is non-zero due to the dispersion of the nonlinear crystal. The three waves mixed are at different wavelength resulting into a phase-mismatch according to eq. 4.26. The birefringence of nonlinear crystals can be used to account for the phase-mismatch. In the case of Ti:LN this is not feasible for the desired wavelengths around 1550 nm and 775 nm.

Nevertheless, when optimal phase matching is achieved, I_3 scales quadratically with the length of the nonlinear crystal (i.e. $I_3 \propto L^2$). The scaling can be seen in fig. 4.11 b). For the non phase-matched case, $I_3 \propto \sin^2 \frac{\Delta kL}{2}$ can be written. In this case, the intensity varies periodically with the coherence length L_c as can be seen in fig. 4.11 b). L_c is defined as

$$L_c = \frac{\pi}{\Delta k} \tag{4.29}$$

and is a measure for the phase-mismatch. For the SHG parameteres considered in this work, coherence lengths of ≈ 9 µm are obtained. In the non phase-matched case, the maximal intensity I_3 will never exceed the limit reached at the coherence length, preventing the generation of a strong nonlinear signal. If no natural phase matching can be obtained, *quasi-phase matching* (QPM) can be used to increase the process efficiency, as can be seen in fig. 4.11 b).

For QPM the orientation of the permanent crystal polarization of lithium niobate is inverted periodically (see fig. 4.2 b)). Inverting leads to a change in the sign of d_{eff}. The periodic nonlinear susceptibility introduces an additional momentum k_Q that is added to the phase-matching condition 4.26, resulting in

$$\Delta k_{QPM} = k_1 + k_2 - k_3 - k_Q = k_1 + k_2 - k_3 - \frac{2\pi}{\Lambda} \tag{4.30}$$

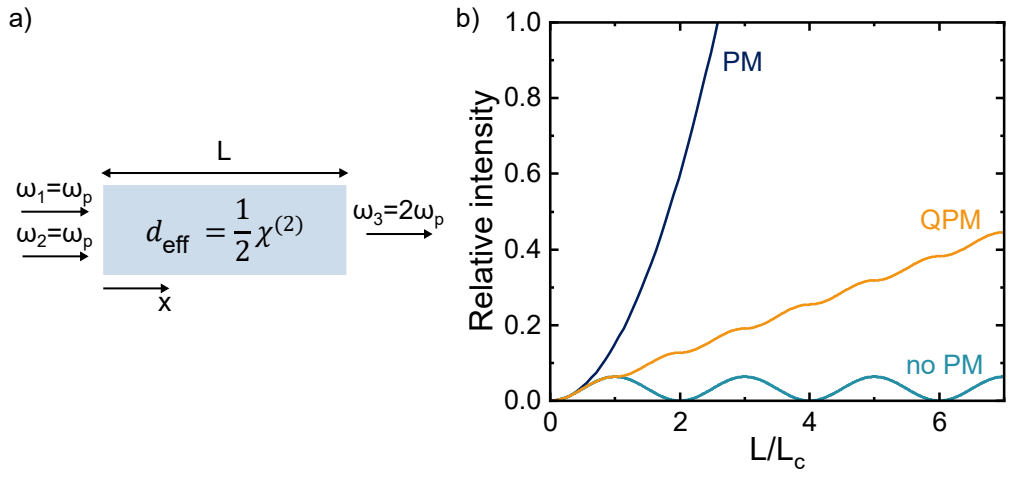

Figure 4.11: a) shows a schematic of a second harmonic generation process. In b) the different phase-matching conditions, phase-matched case (PM), quasi-phase-matched case (QPM) and non-phase-matched case (no PM), are shown.

where Λ is the poling period. By picking the poling period such that $\Delta k_{QPM} = 0$, the quasi-phase-matched case is obtained. The poling period can be calculated by

$$\Lambda = \frac{1}{\frac{n_1(\lambda_1,T)}{\lambda_1} + \frac{n_2(\lambda_2,T)}{\lambda_2} - \frac{n_3(\lambda_3,T)}{\lambda_3}}. \tag{4.31}$$

If a nonlinear process in a waveguide is considered, $n_{1,2,3}$ are defined as the effective refractive indices of the supported waveguides modes at the wavelength $\lambda_{1,2,3}$. For a fixed period Λ, the wavelengths $\lambda_{1,2,3}$ that fulfill the equation are called the phase-matching wavelength. When varying the input wavelength, the measured SHG signal can be described by the sinc^2-function from eq. 4.28, with the maximum intensity obtained at the phase-matching wavelength. The required poling periods vary depending on the type of nonlinear process (i.e type-0, type-I and type-II) since different polarization modes are coupling with each other.

QPM is not only required for nonlinear processes as described in this chapter. In the case of an electro-optical polarization converter, the TE and TM mode need to be phase-matched at the same wavelength. The required poling periods will vary from the one needed for SPDC. In fig. 4.12 the calculated poling periods from eq. 4.31 for an a) polarization converter and b) type-II SHG experiment are plotted. The model introduced in chap. 4.1.1 was used to calculate the effective indices of the waveguide modes at different wavelengths and a temperature of 300 K. For the displayed wavelength regime a linear fit was used to describe the simulated data. The fits are displayed in the plot. In case of type-II SHG at the telecom-wavelength, poling periods ranging from $8.0 - 9.2$ µm are required. For a polarization converter only the two polarization modes of TE and TM need to be considered. Therefore, the contribution of the second mode in eq. 4.31 can be neglected. The calculated poling

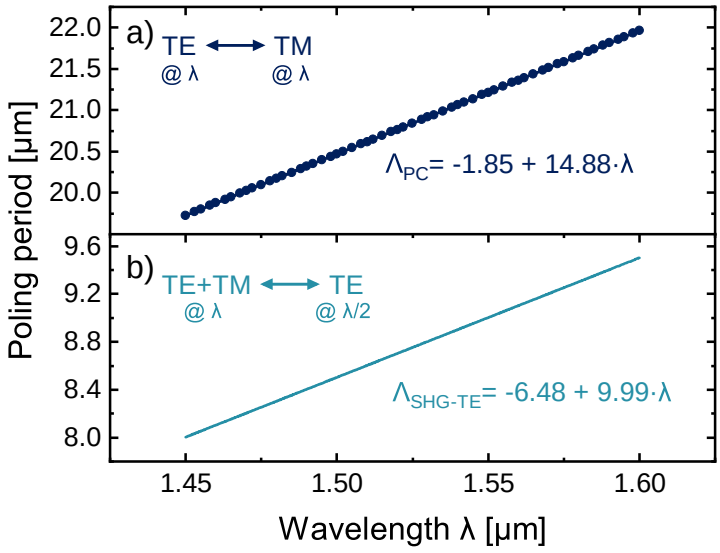

Figure 4.12: a) Calculated poling periods for a polarization converter. For the type II SHG process, plotted in b), only the linear fit is included.

period ranges from $20 - 22$ µm.

Fabricating the desired poling periods accurately and to a high degree of uniformity is crucial for obtaining efficient sources for quantum states such as single photons or squeezed states. In the scope of this work I was responsible for developing the optical lithography process with the maskless laser lithography. The fabrication and the analysis of these poling periods will be discussed in the following.

4.2.3 Fabrication of Periodically Poled Lithium Niobate

Fabrication Summary: To achieve periodically poled Ti:LN waveguides the permanent polarization is inverted in the entire crystal after the waveguide fabrication. With this, the waveguides are now on the $+c$-side of the crystal. The inversion takes place by applying a high voltage pulse ($\approx$ 10.5 kV) on the $+c$ and $-c$ side. With a direct laser lithography the periodic structures are patterned in a positive resist. With liquid electrodes and a high voltage pulse, the permanent polarization is then periodically inverted such that a structure as schematically shown in fig. 4.13 is obtained.

The fabrication of uniform poling periods is a demanding task. Even though the critical dimension of the structures are not close to the resolution of our optical lithography, assuming uniform exposure, due to the dynamic exposure process, is not trivial. The

general fabrication steps are depicted in fig. 4.13. For all the results presented on periodic poling z-cut lithium niobate was used.

For metal diffused waveguides, the periodic poling should be done after the waveguide fabrication because the high temperatures during the diffusion process erase the periodic domain pattern. In addition, the out-diffused lithium layer on the $+c$-surface has to be removed by grinding the sample backside. Otherwise, the lithium layer acts as a blockage to the poling process.

After the residual lithium layer is removed on the backside of the sample, the permanent polarization is inverted in the entire crystal. In order to flip the polarization a voltage of 21 kV per centimeter of sample thickness is required [117]. With $\approx$ 0.5 mm thick samples, voltages around 10.5 kV are needed to invert the polarization. In the actual poling process the position of the lithium/titanium atoms change in the crystal structure due to an applied strong electric field (see fig. 4.2 b)). When the atoms are pushed through the plane of oxygen atoms in the crystal, the permanent polarization is inverted [117].

Since the waveguides are fabricated on the $-c$-side and the initial $+c$-surface is not polished, the later required exposure process for the periodic structures can only be carried out on the initial $-c$-surface. However, since the domain growth (area of differently oriented polarization) starts from the $+c$-side, the crystal polarization has to be inverted as shown in fig. 4.13 a). Liquid electrodes based on an electrolyte are used for the electrical contact. A poling current of $\approx$ 1 mA is used for all the poling structures.

In a next step (see fig. 4.13 b)) a periodic structure is patterned into the positive *AZ 4533* resist. A top view of the structures is given in fig. 4.13 e). The structure needs to be well aligned to the underlying waveguide layer. The angle at the tips is = 120° and fits to the angle of the three equivalent a-axes of the conventional unit cell. They lie in the plane normal to the c axis [101]. For other angles of the tip, the sample can be damaged during the poling process, due to high current densities. The tips are added to the 7 µm wide rectangular poling structure, so that the waveguides are homogeneously poled. The size in the direction of the poling period Λ, also called duty cycle, is set to 42.5% of the poling period. During the poling process the domains not only grow in the z-direction but also parallel to the sample surface. When completely poled, the domains have grown underneath the resist. To achieve a perfect duty cycle of 50%, the design duty cycle is slightly below 50%. A deviation from the ideal duty cycle leads to a reduced efficiency of the nonlinear process.

The parameters used for the exposure are given in tab. 4.3. They were determined equal to the process described in chap. 4.1.3. The structure was developed for 4 min and 30 s in *AZ 826 MIF*. For the final optimized exposure process the WM II was used. In order to align the poling structure to the waveguides, alignment crosses were fabricated in the same step as the waveguides. The design of the poling structure is then aligned to the alignment crosses on the sample.

The electrical contact of the sample is done by liquid electrodes. Since the solutions attacks the photoresist, the resist is first treated with a thermal reflow process and then protected

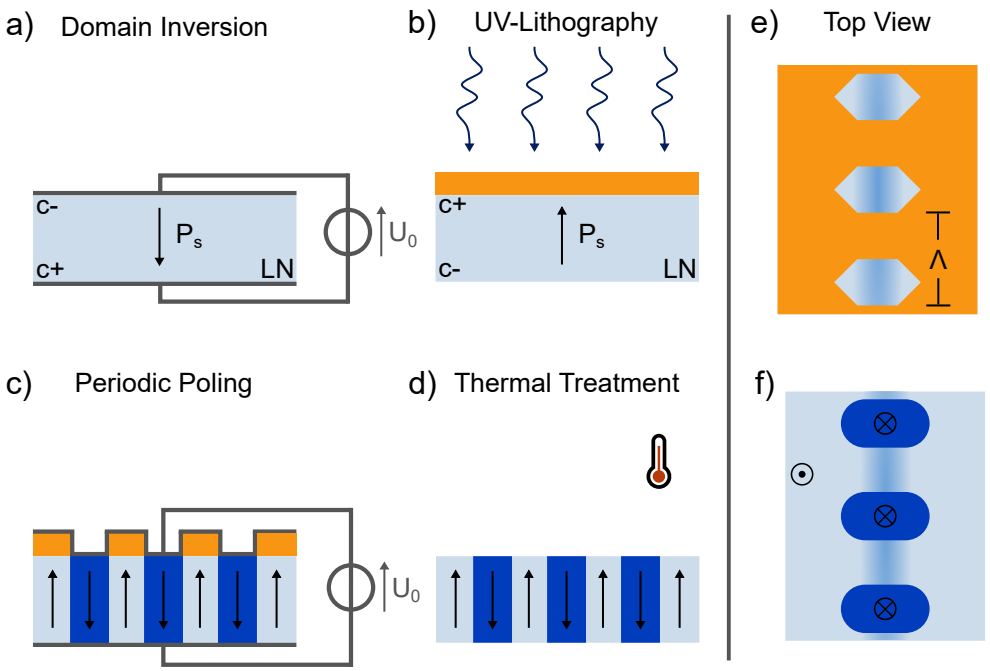

Figure 4.13: Simplified fabrication scheme for periodic poling structures in lithium niobate. In a) the permanent polarization is inverted in the entire crystal by applying a high voltage. In the lithography step the periodic poling structure is patterned in the photo resist. A schematic of the top view after developing is shown in e). c) pictures the electrical contacting of the surface. With a voltage pulse the polarization is inverted in specific areas of the crystal, forming the periodic structure shown in c) and d). To reduce losses and smooth the domain walls the sample is slowly heated up in the step d). f) pictures the finished sample from a top view.

by a gold palladium alloy that is deposited by sputtering. The metal layer also protects the resist from UV light which enables the imaging of the resist with a UV laser microscope without damaging the resist. From the measurements done with a laser microscope we can estimate the homogeneity of the poling period and the duty cycle on a sample. An example picture after the thermal reflow and the gold palladium alloy is given in fig. 4.14 a). The picture shows the good alignment to the underlying waveguide layer. The rounding of the tips result from the thermal reflow process of the resist.

In order to quantify the homogeneity of the poling period, the length of 8 poling periods is measured. Since the laser microscope uses a wavelength around 400 nm, averaging over

Table 4.3: Lithography parameters for the postive photoresist *AZ 4533* on lithium niobate with the WM II.

Photoresist	Focus	Power	Filter
AZ 4533	−2%	28.2 mW	5%

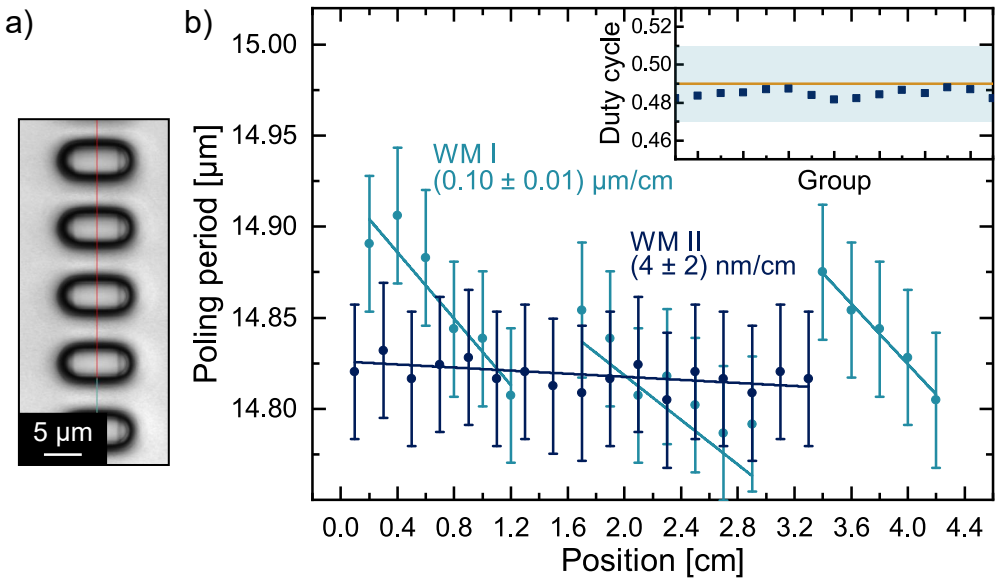

Figure 4.14: An example picture of the poling periods is shown in a). The results presented in b) indicate that for the WM I a shift of (0.10 ± 0.01) µm/cm can be measured. With the WM II this is significantly reduced. The inset shows the measured duty cycle for different waveguide groups. The variations of the duty cycle stay well within the ±2% error.

multiple poling periods increases the resolution, which is limited by the wavelength. These measurements can be done for multiple positions along the waveguide. In a first step the exposure was done for both write modes to check if the WM I offers sufficient quality. The measured poling periods are shown in fig. 4.14 b). The results given are averaged over multiple waveguide groups. The errors stated in the plot are calculated from the accuracy of the laser microscope used. For the WM I, the same design was patterned three times (position $0.2 - 1.2$ cm, $1.7 - 2.9$ cm and $3.4 - 4.2$ cm) along the waveguide direction. The data shows a clear trend of decreasing poling periods, when the distance from the design origin increases. The drift is estimated with a linear regression to quantify the change in the poling period. For the WM I a drift of (0.1 ± 0.01) µm/cm in the poling period was measured. This would result in a significant shift of the phase-matching wavelength along the waveguide. The shift could be due to a non uniform writing speed of the system along the waveguide direction. When exposing the design, the laser beam is stationary along the waveguide direction and it is assumed that the sample drives at a constant speed in the same direction. If this speed is not constant this may result in a drift of the poling period as measured for this case. Fluctuation in the laser power or resist inhomogeneities would be measurable in the duty cycle of the poling structures but not in the poling period.

To improve on the uniformity of the poling period, a process for the WM II was developed. The results are also plotted in fig. 4.14 b). The linear regression estimates a shift of (4 ± 2) nm/cm which is a significant improvement of the poling periods. Based on the results,

the fabrication of poling periods will be carried out with the WM II. Whether it is feasible to further improve the results by taking the drift into account in the design is a question to be investigated in the future.

In the insert of fig. 4.14 b) the results for the duty cycle are given. For each data point the duty cycle was averaged over multiple measurements along the waveguide direction. The average duty cycle is plotted in dependence of the waveguide group. An average duty cycle of $(49 \pm 2)\%$ was measured which is close to the ideal 50/50 duty cycle. In the experiment the domain of the inverted polarization does not only grow in the direction of the z-axis but also slightly underneath the resists in the normal plane of the z-axis. Therefore a duty cycle slightly below 50% is ideal to achieve an optimal duty cycle after poling. The deviation of the measured duty cycle stays well within the ±2% error of the mean duty cycle. The error is given by the resolution of the microscope (±2%). The variation could result from fluctuations in the laser power or the resist thickness. As a future task it may be possible to further improve the quality of the poling structures in the resist by taking the measured drift into account for the design parameters. For the purpose of this work, the quality of the resist structures was assumed to be sufficient to continue with the actual poling process.

After the investigation of the structure in the resist, the actual poling step, pictured in fig. 4.13 c), can be performed. Liquid electrodes are used to contact the gold palladium and the sample surface. The shape of the voltage pulse depends on the sample thickness (max. voltage required) and the free area that needs to be inverted (length of the pulse). The voltage is ramped up with high speed. Once the voltage exceeds the critical voltage required to invert the polarization, a constant current flows through the contacted sample area. The size of the area to be poled dictates for how long the voltage/current is kept constant. A poling current of 1 mA was used. To keep the flipped domain stable the voltage pulse decays with slow speed.

In a last step the resist is removed with acetone and isopropanol. The remaining gold palladium film is removed with a gold etch. In order to smooth the domain falls, reduce artificially poled areas and reduce propagation losses the samples are heated up to 400 °C. A schematic of the finished sample is shown in fig. 4.13 d) and f).

To analyze the poling periods further, one could selectively etch the surface of the LN samples. Since the different domain orientations have slightly different etching speeds in the ammonium solution, the poled areas can be made visible. This would increase propagation losses if further optics experiments are done. Therefore, nonlinear measurements have been done to quantify the quality of the fabricated poling periods in a non-destructive way.

4.2.4 Nonlinear Characterization of Periodically Poled Lithium Niobate

With the optimized fabrication process, a periodically poled Ti:LN sample (Ti:PPLN) with poling periods ranging from 8.77 – 8.81 µm and 9.86 – 9.91 nm and a length of 24 mm were

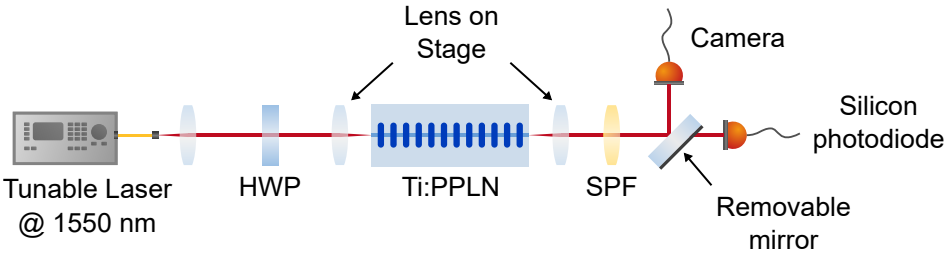

Figure 4.15: Schematic of the setup used for the nonlinear characterization of Ti:PPLN waveguides. For in- and outcoupling two lenses on x, x, y-stages are used. The sample is mounted on a stage which enables switching between the different waveguide groups. A half-wave plate (HWP) is used to set the input polarization. A short-pass filter (SPF) filters out the unwanted fundamental light.

fabricated. The periods were varied in 10 nm-steps. Each poling period was fabricated on three waveguides. The first set of poling periods were set for degenerate type-II SPDC at 1550 nm wavelength at cryogenic temperatures [103]. The longer poling periods have an expected phase-matching wavelength for type-II SHG above 1640 nm. They were fabricated for performing an SFG experiment in the scope of another project.

To determine the expected phase-matching wavelengths for the given periods, the dispersion of the effective refractive index n_{eff} has to be known. n_{eff} can be calculated with FEM-simulations. For the calculation an empirical correction term is added to correct for differences in the simulation model and the experimental data. The correction is based on the experimental data from previous characterizations of Ti:PPLN that were fabricated with the conventional mask lithography [99, 108]. For the correction, a temperature dependent fifth-order polynomial function is used [103]. The reasons for the correction can be manifold. If waveguide parameters, the temperature-depended refractive index, or the diffusion process deviate from the assumption taken in the empirical model, this can lead to an offset in the experimentally determined phase-matching wavelength and the theoretically expected wavelength. Although the correction can be applied down to cryogenic temperatures, all results presented in this thesis were obtained at room temperature.

Since type-II SHG acts as the reverse process of degenerate type-II SPDC, a first investigation of the poling periods is done with SHG measurements. This reduces the restrictions placed on the detection, because the measured signals are not on the single-photon level. The setup used to characterize the poling periods can be seen in fig. 4.15. A tunable laser is used as an input signal. The wavelength of the input signal is tuned in a 4 nm window in 0.01 nm steps. The laser is coupled into a waveguide by butt coupling with a lens. Because the process is optimized for type-II, the input is diagonally polarized to have energy in both polarization modes of the waveguide. In the waveguide SHG-photons with TE polarization are generated and coupled out to a photodiode. By filtering out the fundamental light, the wavelength-dependent intensity of the SHG signal can be measured.

An example measurement of a phase-matching curve for a poling period of 8.80 µm can

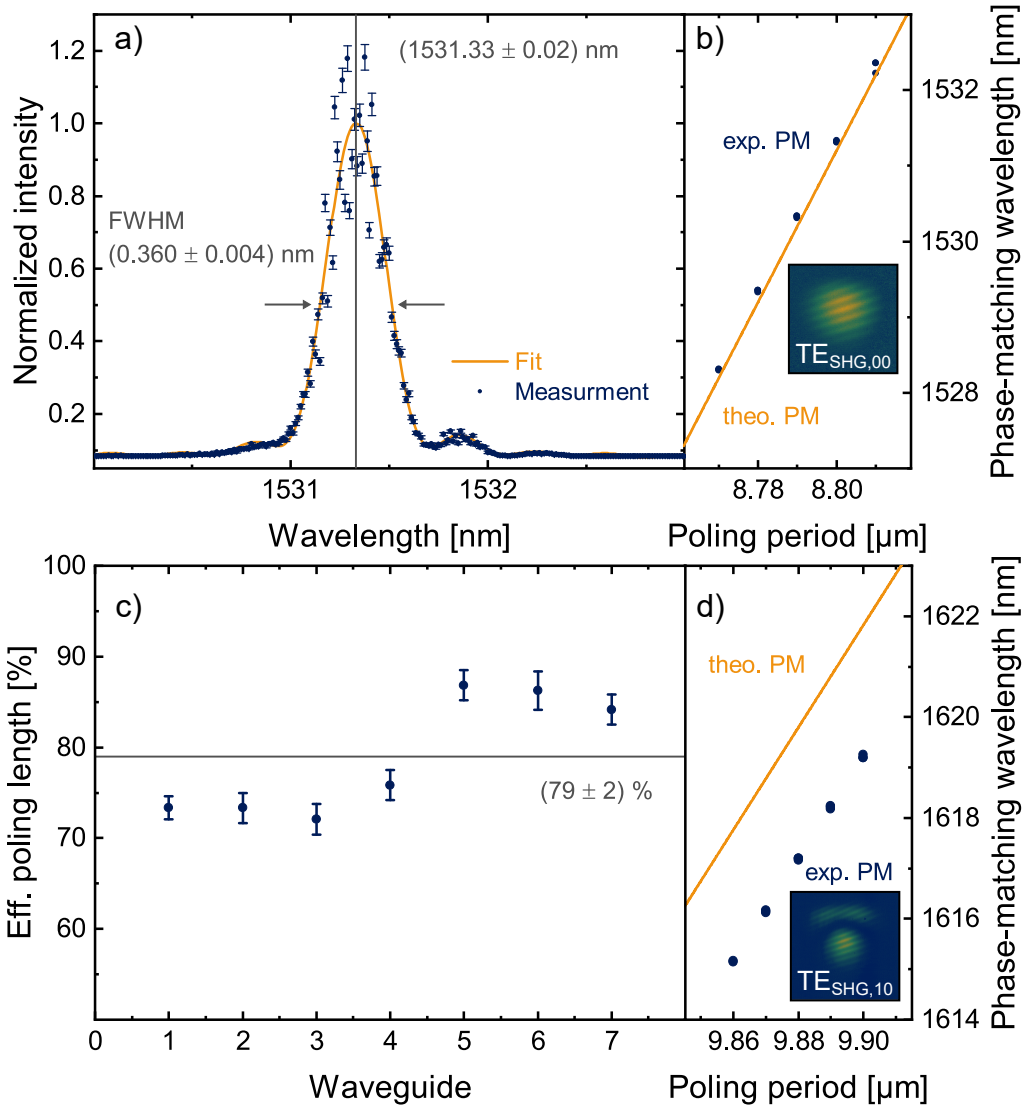

Figure 4.16: a) shows an example measurement of a phase-matching curve with a phase-matching wavelength of (1531.33 ± 0.02) nm and a FWHM of (0.360 ± 0.004) nm. In b) the experimentally determined phase-matching wavelength (exp. PM) of the poling periods 8.77 – 8.81 µm agrees well with the theoretically expected wavelength (theo. PM). The two mode images are examples for the b) $TE_{SHG,00}$ and d) $TE_{SHG,10}$ mode. In c) the effective poling length obtained from the fit for different waveguides is plotted. An average poling length of (79 ± 2)% is measured. d) shows the comparison of the experimental and theoretical phase-matching wavelength the poling periods ranging from 9.86 – 9.91 µm. The results are based on the higher order $TE_{SHG,10}$ mode.

be seen in fig. 4.16 a). The normalized SHG intensity is plotted over the fundamental input wavelength. The noise on the signal comes from Fabry-Pérot resonances in the setup,

which lead to additional modulations of the signal when varying the input wavelength. The photodiode has a measurement uncertainty of ±3%, resulting in the given error. According to eq. 4.28 the data should follow a sinc^2-function for the quasi-phase-matched case. However, due to imperfections in the phase-matching, we require an asymmetric sinc^2-function to match the obtained data. The analysis follows the procedure in [108]. The fit results in a phase-matching wavelength of (1531.33 ± 0.02) nm, where the error is given by the accuracy of the tunable laser. Since multiple poling periods have been fabricated on a single chip, we can measure different poling periods and the shift in the center wavelength. For the poling periods ranging from $8.77 - 8.81$ nm, the experimental phase-matching wavelength is plotted in fig. 4.16 b). In addition the phase-matching condition determined from the simulations with the correction is added. The calculated error from the fit for each data point is negligible and therefore excluded from the plot.

Each poling period could be measured on three different waveguides. All of them are included in fig. 4.16 b). For equal periods almost no difference can be identified from the experimental data, indicating that periodic poling structures can be fabricated with a high precision. Moreover, we can see that the experimental data agrees well with the expectations from the simulation indicating an accurate poling process. The experimental phase-matching wavelength lies within 0.2 nm of the simulated data.

The periods were fabricated in steps of 10 nm. This results in a shift of the phase-matching wavelength by 0.1 nm. This shift is matched by the experimental data. Herein, we have demonstrated that by using a maskless laser lithography, poling periods for SPDC at telecom wavelengths can be fabricated with high precision and accuracy. Furthermore, it is possible to precisely tune the phase matching to optimally match the sample to the desired nonlinear process.

For the periods in the range of $9.86 - 9.91$ nm the phase matching for SHG is expected to be outside the tuning range of the laser, with wavelengths above 1640 nm. Nevertheless, we were able to measure sinc^2-like phase-matching condition from $1615 - 1620$ nm for all poling periods in this range. The phase-matched wavelengths are shown in fig. 4.16 d). The signal measured is roughly 50% weaker than for the neighboring waveguide group with a shorter poling period. The reduced signal indicates a decrease in the efficiency of the generation process.

Just as for the directional coupler, the spatial overlap of the coupling modes affects the efficiency of the second harmonic generation. Since the waveguide is not single mode at the SHG wavelength, higher spatial modes can also contribute to the second harmonic generation. The standard 7 µm waveguide supports the three spatial modes: $\mathrm{TE}_{\mathrm{SHG},00}$, $\mathrm{TE}_{\mathrm{SHG},01}$ and $\mathrm{TE}_{\mathrm{SHG},10}$. Therefore, the lower efficiency of the nonlinear process could be explained by a lower mode overlap due to a higher order SHG mode. To verify this, the effective refractive indices for the different modes can be calculated. With these, the theoretical phase-matching condition can be calculated. The reduction of the effective index results for an increased mode index leads to shift in the phase-matching wavelength to shorter wavelength, which was measured in the experiment. Fig. 4.16 d) gives the

theoretical phase-matching condition for the $TE_{SHG,10}$ mode, which best agrees with the exp. data.

To verify that the nonlinear signal is in the $TE_{SHG,10}$ mode, mode images are made at the SHG wavelength. Two example images for the $TE_{SHG,00}$ and $TE_{SHG,10}$ modes are given in fig. 4.16 b) and d). While for the shorter poling periods (i.e. 8.77 – 8.81 µm) the fundamental SHG mode is measured, the mode image in fig. 4.16 d) clearly shows that the SHG signal is generated in the $TE_{SHG,10}$ mode.

Since the origin of the SHG signal has been clarified, it is now necessary to take a look at the discrepancy between the simulations and the experimental data. Compared to the previous small difference, there is a deviation of $\approx$ 2.5 nm in the phase-matched wavelength. A deviation in the phase-matching condition can always be attributed to a deviation in the effective refractive index.

If we compare n_{eff} for the fundamental SHG mode and the higher order mode, the difference is in the order of 10^{-3}. This difference provides a shift in the phase-matching condition of about 20 nm. Consequently, the difference in effective refractive index, at a deviation of 2.5 nm, is in the order of 10^{-4}. Thus, an accuracy of the simulation up to this order must be given to describe the results accurately. As already mentioned several times, an empirical model is used for the simulation, which was optimized for the fundamental modes in Ti:LN waveguides, which is why an exact description of the higher modes is not guaranteed. Furthermore, imperfections in the fabrication or the crystal also have an influence on the phase-matching condition. Since the system is so complex, it is not trivial to pinpoint the origin of the deviation. To compensate for the deviation, the phase-matching condition could be shifted by a controlled temperature change of the sample.

Nevertheless, the experimental data indicate that the poling periods can be patterned with a significant degree of reproducibility, since different waveguides with equal poling periods yield the same results. This hints towards an incomplete description of the experimental system by the simulation. The obtained data could be used to adjust the simulation model for higher order modes at the second harmonic wavelength. For further investigations it would be good to fabricate the same periods on different sample to exclude effects from the crystal and investigate the reproducibility between different samples further.

To analyze the quality of the fabricated periods further, we can consider the FWHM obtained by the fit, as displayed in fig. 4.16 a). For the example poling period of 8.80 µm, we obtained a FWHM of (0.360 ± 0.004) nm. The error is determined from the fit. The FWHM is influenced by the length of periodic poling structure for a given constant phase-mismatch $\Delta k \neq 0$. When increasing the length of the uniform poling the sinc^2-function narrows while for a short length of the poling structure the FWHM increases. Imperfections in the poling structure influence the FWHM similarly. Deviations in the phase-matching condition lead to a reduction of the uniform poling length [118]. Hence, non-uniform poling periods or variations in the waveguide profile along the propagation direction lead to a broadening of the sinc^2-function and can also introduce an asymmetry [119]. The effective poling length L_{eff} quantifies the reduction in the uniform poling length due to

these imperfections. With a python script [120], that was obtained in the scope of the work presented in [119] and [108], L_{eff} of a waveguide can be calculated. The perturbation of the phase-matching condition $\delta\beta_{\text{step}}$ is considered as a variation in the waveguide profile and is implemented as a step function consisting of seven equally broad plateaus of height c_i along the propagation direction x:

$$\delta\beta_{\text{step}}(x, c_1, \cdots, c_7) = c_i \text{ for } \frac{i-1}{7}L \leq x < \frac{i}{7}L, \text{ where } i = 1, \cdots, 7. \tag{4.32}$$

The perturbation is varied such that the deviation between the fit and the experimental data of the phase-matching curve is minimal. An example fit can be seen in 4.16 a). The relative effective poling length obtained for different waveguides is shown in 4.16 c). A mean effective poling length of $L_{\text{eff,mean}} = (79 \pm 2)\%$ and a maximum effective length of $L_{\text{eff,max}} = (87 \pm 2)\%$ could be obtained. The error is given by the fitting algorithm. We can conclude that the maskless exposure process delivers comparable results to the conventional fabrication process with photomasks [108]. With the results we could prove, that the direct laser writing provides a flexible alternative for fabricating periodically poled lithium niobate (PPLN).

To further increase the effective length is a demanding task. There are many factors that can have an influence on the propagation constant of the guided mode. Each factor would need to be separately investigated to check its influence on L_{eff}. A first step towards increasing L_{eff} even more , can be made by fabricating the waveguides with the WM II, to reduce variations in the waveguide profile.

In addition, conventional longer samples are used, which are then poled to a longer length. This allows the ends of the sample to be cut off after fabrication, leaving only the middle, homogeneously poled area. The reduced influence of imperfections, that can occur at the edge of the sample, increases the effective poling length. In our case, the sample was 26 mm long at the beginning, of which 24 mm should be poled. After polishing the end facets, the length was reduced to the 24 mm of the poling structure. Further shortening of the sample could increase the percentage of effective pole length by removing manufacturing imperfections that can result from being too close to the edge of the sample.

This first demonstration of PPLN waveguides with direct laser lithography leaves room for further investigation and experiments. The exploration of short poling periods < 6 µm is an demanding task which could be tackled in the future [117]. By varying the poling period along the waveguide, the phase-matching curve and with it the spectrum of single-photons, generated by SPDC, can be tailored to a specific task [121, 122]. For this, an accurate model and a reproducible patterning of the poling structures is required. Bulk lithium niobate is not the only platform that uses QPM based on periodic poling. Thin-film lithium niobate (TFLN) is a promising platform for photonic quantum systems. The fabrication of periodically poled TFLN is currently investigated by many groups around the world, leaving room for further investigations [123–125]. For all these projects, direct laser writing offers rapid prototyping and flexible design testing especially for aperiodic poling.

In a last step I want to complete the toolbox that lithium niobate offers by presenting the theoretical background and the fabrication of electro-optical modulators in lithium niobate.

4.3 Electro-Optical Modulation

The electro-optical properties of lithium niobate allow the manipulation of the refractive index of LN locally by applying an external electric field. Therefore, electrodes need to be placed on-top of the existing waveguide system. This further completes the toolbox from fig. 3.3 with the areas of state generation and electro-optic modulation fulfilled. The electro-optical properties of lithium niobate are based on the Pockels effect and many applications have been developed based on this effect in different crystals that lack inversion symmetry. Before describing the fabrication method for the electrodes, I want to briefly touch on the physical background and the working principle.

4.3.1 Background

Just like the previously introduced nonlinear effect of second harmonic generation, the Pockels effect can be seen as a nonlinear process of second order. The electric displacement field D in the crystal can be described by

$$D = \epsilon_r \epsilon_0 E = \kappa^0 E + \alpha E^2 + \beta E^3 + \dots \tag{4.33}$$

with the relative permittivity $\epsilon_r = n^2$ for nonmagnetic materials, the vacuum permittivity ϵ_0 and the applied external electric field E [76]. Just like for the material polarization P, a Taylor expansion can be made. D is in a first approximation linear dependent on the external electric field E and linked by the factor κ^0. Deviations from this linear behavior for stronger electric fields are described with the terms of higher order. In general the permittivity ϵ_r is given by the deviation of $\mathrm{d}D/\mathrm{d}E$ [76]:

$$\epsilon_r = \frac{\mathrm{d}D}{\mathrm{d}E} = \kappa_0 + 2\alpha E + 3\beta E^2 \tag{4.34}$$

Since the permittivity ϵ_r is linked to the refractive index, applying an external electric field can be seen as slight change of the refractive index. The change in the refractive index has an influence on the optical light field propagating through the material. When limiting ourselves to the second term, we talk of the linear Pockels-effect since the change in permittivity scales linearly with the external electric field. The next term of higher order would be considered as the quadratic Pockels effect but is of no importance for this work.

The change in the refractive index based on the linear Pockels effect can then be described by [112]

$$\Delta\left(\frac{1}{n^2}\right)_i = \sum_j r_{ij} E_j \tag{4.35}$$

where r_{ij} is the 6 x 3 electro-optic tensor which relates the changes in the refractive index of lithium niobate to the external static electric field E_j in the crystal direction j.

The refractive index of LN can be described with an ellipsoid, with the main axis dictated by the ordinary and extraordinary refractive index. $\Delta\left(\frac{1}{n^2}\right)_i$ quantifies how the refractive index ellipsoid changes depending on the applied electric field. Since LN belongs to the 3m point group the electro-optic tensor is defined as

$$\begin{bmatrix} 0 & -r_{22} & r_{13} \\ 0 & r_{22} & r_{13} \\ 0 & 0 & r_{33} \\ 0 & r_{51} & 0 \\ r_{51} & 0 & 0 \\ -r_{22} & 0 & 0 \end{bmatrix}. \tag{4.36}$$

To simplify the expression for the tensor, the Kleinmann symmetry was used just like for the nonlinear susceptibility in chap. 4.2.1. The use of the electro-optical effect enables the realization of integrated variable phase shifters, variable beam splitters and polarization converters. In the scope of this work phase shifters and polarization converters were fabricated for the integrated homodyne experiment presented in chap. 6.

A polarization converter is a device which utilizes the electro-optical properties of a crystal to couple the two supported polarization modes of a waveguide (i.e. TE and TM) by applying an external DC electric field. Since lithium niobate is birefringent, the two polarization modes have different propagation constants (i.e. $\Delta\beta = \beta_{\mathrm{TE}} - \beta_{\mathrm{TM}} \neq 0$). For the efficient coupling between the two polarization, we therefore need to introduce some periodic poling to account for the phase-mismatch. The desired poling periods were already plotted in fig. 4.12.

With a fixed poling period Λ we can write the phase-mismatch as

$$\Delta\beta = 2\pi\left(\frac{n_{\mathrm{TE}}(\lambda) - n_{\mathrm{TM}}(\lambda)}{\lambda}\right) - \left(\frac{2\pi}{\Lambda}\right). \tag{4.37}$$

$n_{\mathrm{TE}}(\lambda)$ and $n_{\mathrm{TM}}(\lambda)$ are the wavelength dependent effective refractive indices of the waveguide modes. If the poling period compensates for the phase-mismatch $\Delta\beta = 0$. When we consider the amplitudes of the two polarization modes $A_{\mathrm{TE}}(x)$ and $A_{\mathrm{TM}}(x)$, we can use

the coupled mode equations to derive the two solutions [100, 126]

$$\begin{aligned} A_{\mathrm{TE}}(x) &= \left\{ A_{\mathrm{TE}}(0) \left[\cos sx - i\frac{\Delta\beta}{2s} \sin sz \right] - i\frac{\kappa}{s} A_{\mathrm{TM}}(0) \sin sx \right\} \exp\left(i\frac{\Delta\beta x}{2} \right) \text{ and} \\ A_{\mathrm{TM}}(x) &= \left\{ A_{\mathrm{TM}}(0) \left[\cos sx + i\frac{\Delta\beta}{2s} \sin sz \right] - i\frac{\kappa}{s} A_{\mathrm{TE}}(0) \sin sx \right\} \exp\left(-i\frac{\Delta\beta x}{2} \right) \end{aligned} \tag{4.38}$$

with

$$s = \sqrt{\kappa^2 + \left(\frac{\Delta\beta}{2} \right)^2}. \tag{4.39}$$

s is definded as the switching parameter and if we consider the phase matched condition ($\Delta\beta = 0$) the switching parameter is equal to the coupling constant κ. $A_{\mathrm{TE}}(0)$ and $A_{\mathrm{TM}}(0)$ are the amplitudes of the input field for the two polarizations. κ is defined as [100]

$$\kappa = \frac{\pi \bar{n}^3 r_{51} V \eta}{\lambda G} \tag{4.40}$$

where $\bar{n} = \sqrt{n_{\mathrm{TE}} n_{\mathrm{TM}}}$ is the effective refractive index as the geometric mean. For the conversion of the polarization we require the electro-optic tensor element r_{51} which is equal to the r_{42} element which corresponds to a coupling of the two polarization modes in the y- and z-direction of the crystal when an electric field along the y-direction is applied. For this reason the electrodes will need to be placed alongside the waveguide. When a voltage is applied to the electrodes, the electric field generated is oriented along the y-direction and thus addresses the tensor element r_{42}. A schematic for the polarization converter and the orientation of the applied electric field is given in fig. 4.17 a). The electrode structure depicted in 4.17 a) consists out of silicon dioxide (SiO_2), chromium (Cr) and gold (Au) which corresponds to the actually fabricated electrode structure. The strength of the coupling is additionally influence by the overlap η between the applied electric field and the spatial modes. η is given by

$$\eta = \frac{G}{V} \frac{\int_A E^*_{\mathrm{TE}} E_j E_{\mathrm{TM}} \, \mathrm{d}A}{\sqrt{\int_A E^*_{\mathrm{TE}} E_{\mathrm{TE}} \, \mathrm{d}A \int_A E^*_{\mathrm{TM}} E_{\mathrm{TM}} \, \mathrm{d}A}} \tag{4.41}$$

where G and V are defined as the gap between the electrodes and the voltage applied to them. Under the assumption that the two polarization modes are phase matches the coupled amplitude equations 4.38 simplify to

$$\begin{aligned} A_{\mathrm{TE}}(x) &= A_{\mathrm{TE}}(0) \cos \kappa x - i A_{\mathrm{TM}}(0) \sin \kappa x \text{ and} \\ A_{\mathrm{TM}}(x) &= A_{\mathrm{TM}}(0) \cos \kappa x - i A_{\mathrm{TE}}(0) \sin \kappa x \end{aligned} \tag{4.42}$$

From the above equation we can see that the energy is now transferred between the two polarization modes. The coupling constant κ defines how fast the energy is transferred between the modes.

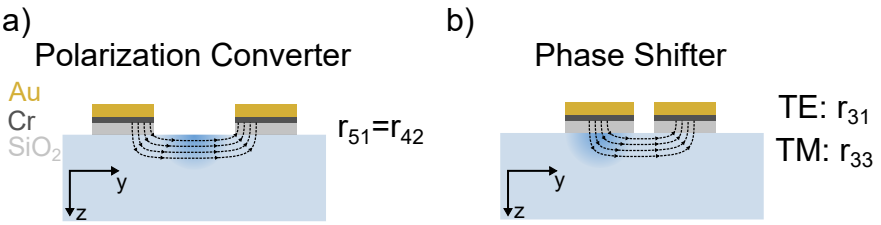

Figure 4.17: a) Schematic of a polarization converter. The applied electric field in the crystal is mainly oriented along the y-direction. For the phase shifter in b) the electrode is placed on top of the waveguide leading to an electric field mainly oriented along the z-direction of the crystal. In this case, the two polarizations TE and TM exhibit a different phase modulation due to the two tensor elements r_{31} and r_{33}. The electrodes consist of silicon dioxide (SiO_2), chromium (Cr) and gold (Au).

Before I continue with the fabrication and the experimental analysis of the fabricated polarization converter, I want to briefly discuss the background for an integrated phase shifter, since it will be included on the homodyne chip. The electrode configuration for a phase shifter is shown in 4.17 b). The electrodes are placed on-top of the waveguide Thus, the applied electric field is mainly oriented along the z-direction. In this scenario, the two tensor elements $\rho_{31} = 7.7 \times 10^{-12}$ m/V and $r_{33} = 28.8 \times 10^{-12}$ m/V lead to an unequal modulation of the optical phase for the two polarization modes. We can write the introduced phase difference $\Delta\Phi$ between the two polarizations as

$$\Delta\Phi = \kappa_{\mathrm{TE}} L - \kappa_{\mathrm{TM}} L \tag{4.43}$$

where L is the length of the phase modulator. $\kappa_{\mathrm{TE,TM}}$ is the coupling constant defined as in eq. 4.10 for the two polarization modes. In the coupling constant, the difference in the electro-optical coefficient is taken into account. More details on the theory can be found in [100, 112, 126]. In the following, I will discuss the fabrication process of the electrodes.

4.3.2 Fabrication of Electrode Structures

Fabrication Summary: The fabrication process for the electrodes is based on a lift-off process. The electrode stack consists of 400 nm of SiO_2 as buffer layer, 10 nm of Chromium as an adhesion layer and 100 nm of Gold for the electrodes. All the materials are magnetron sputtered. The buffer layer of SiO_2 is used to reduce the additional losses introduced by the electrodes on top of the waveguide. The general fabrication process can be seen in fig. 4.18.

After a standard cleaning procedure with acetone and isopropanol, 2 µm thick *AZ nLof 2020* resist is spin coated. The softbake temperature is 110 °C for 17 min. In comparison to the process for the waveguides the baking time is increased by 2 min since the resists thickness is increased for this process. The negative photoresist offers negative sidewall

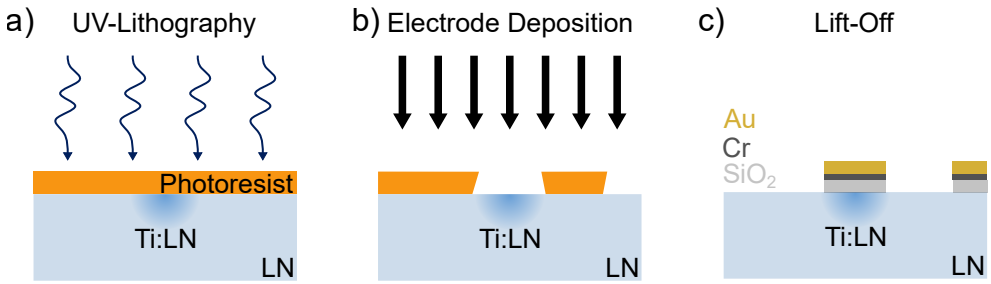

Figure 4.18: Fabrication of electrodes for electro-optical modulators. a) shows the exposure process. The deposition process pictured in b) is done by magnetron sputtering. The electron stack consists of silicon dioxide (SiO_2), chromium (Cr) and gold (Au). After the lift-off the electrode remain on the sample, as shown on c).

Table 4.4: Lithography parameters for 2 µm thick *AZ nLof 2020* on lithium niobate with the WM I.

Photoresist	Focus	Power	Filter
AZ 4533	4%	30 mW	5%

flanks as also depicted in fig. 4.18 b) which is beneficial for a clean lift-off process with reduced artifacts. The thickness is increased to 2 µm, since the electrode stack has a total height of > 500 nm.

The parameters for the exposure can be taken from tab. 4.4. The exposure was optimized such that a negative sidewall angle was achieved for the resist. Higher doses would lead to a widening of the structures and reduced negativity of the sidewalls. Increasing the PEB-time or the temperature would have a similar effect as increasing the dose. The PEB time and temperature were set to 17 min at 110 °C in an convection oven.

The development was carried out over 2 min and 15 s with 85% of *AZ 726 MIF* and 15% of water. No hardbake is required. In order to verify the negativity of the resist sidewalls a sample was cleaved and SEM images were taken under a vertical angle mount. An image of the structure can be seen in fig. 4.19 a). The negativity of the sidewalls can be clearly identified. The sidewall angle is estimated to be 72°.

For a final structure electrode gaps ranging from 9 – 15 µm and a length of several centimeters need to be realized. When the electrodes act as signal and ground electrodes a clean separation of the electrodes over the entire length of the electrodes need to be realized. This puts a high demand on the reliability of the lift-off process. Just like for the poling periods the electrodes need to be well aligned to the underlying waveguide layer, to have efficient modulation of the refractive index. From the laser microscope image in fig. 4.19 b) the alignment to the waveguide can be identified.

After the exposure the electrodes are magnetron sputtered (see fig. 4.18 c)) on the substrate. The sputtering was done by Felix vom Bruch. The electrode stack consist of a 400 nm silicon dioxide layer, a 10 nm chromium adhesion layer and a 100 nm gold layer. The lift-off

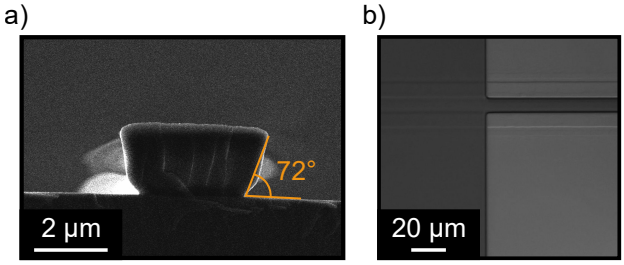

Figure 4.19: a) SEM image of the resist after developing. The negative sidewalls are at an angle of 72°. In b), a microscope image of the resist structure is shown, which is well aligned with the waveguide layer.

process is done with *TechniStrip NI555* as a remover which is heated up to 70 °C. The remover resolves the cross-linked resist without leaving residuals on the sample surface and is used for resists that withstand acetone as a remover. In a last step isopropanol is used for sample cleaning.

The development of the demonstrated fabrication process leads to the realization of electro-optic components. In the scope of this work an on-chip polarization converter and phase shifter were required, to perform a homodyne experiment. The characterization of the polarization converter will be described in the following section.

4.3.3 Characterization of the Polarization Converter

For the homodyne experiment, we require a polarization converter and a phase shifter additionally to the already presented PBS in chap. 4.1.4. In case of the polarization converter we need to periodically pole the waveguide in order to achieve phase matching between the two polarization modes. To achieve this at the telecom wavelength I fabricated poling periods from 20.96 – 21.38 µm in steps of 0.03 µm. The poling is done according to the process described in chap. 4.2.3. A length of 15 mm was periodically poled.

One waveguide group always consists of a straight waveguide with a polarization converter and the combination of a directional coupler and polarization converter. The directional coupler are the ones previously described in chap. 4.1.4. The exact layout of the chip can be found in chap. A.4. The electrodes are deposited as described in the previous chapter. In order to characterize the performance of the polarization converters the setup shown in fig. 4.20 is used. The characterization was carried out together with the help of Frederik Thiele.

Since the polarization converter has a phase-matching condition governed by the periodic poling, the conversion depends on the input wavelength. Thus, a tunable laser source is used to analyze the wavelength dependence of the conversion in the wavelength range from 1538 – 1556 nm. Additionally, according to eq. 4.41 the signal depends on the applied voltages to the electrodes. Therefore, the electrodes are contacted with probing needles

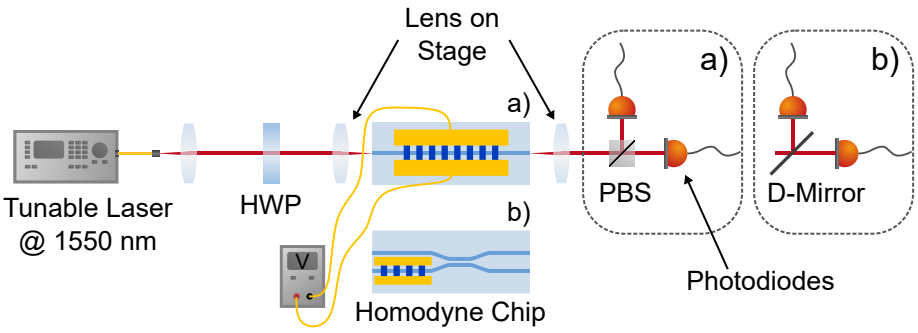

Figure 4.20: Schematic of the setup used to characterize the polarization converter of the homodyne chip. For a), the straight waveguide is characterized and an off-chip polarizing beam splitter (PBS) is used to split the two signals. For b), a PBS is integrated on chip. The signals from the two output ports is split with a D-shaped mirror (D-mirror) and measured on two photodiodes. A half-wave plate (HWP) is used to set the input polarization. Voltages in the range of −60 to 60 V can be applied to the electrode.

and a voltage in the range from −60 to 60 V can be applied. For each wavelength setting, the voltage is scanned in this range.

For the straight waveguides an off-chip PBS is used to split the light from the chip into the two polarizations of TE and TM. With two photodiodes the wavelength and voltage dependent conversion can be measured. When the polarization converter with the integrated PBS is characterized, the signals coming from the two output ports of the PBS are split with a D-shaped mirror and than measured with the two photodiodes. With this we can measure the switching map for all waveguide groups with a polarization converter. An example of a switching map for a polarization converter with an integrated PBS is shown in the inset of fig. 4.21 a). A clear modulation of the photodiode signal is observable. The fringing effects visible in the switching map arise from unresolved Fabry-Pérot resonators in the setup. For the calculation of the shown switching map, the signal from both photodiodes is normalized on the sum of both photodiodes.

In a next evaluation step, we investigate the maximum signal difference as a function of the input wavelength. This can be done for any set voltage value. The absolute maximum in the difference is then used to evaluate the phase-matching behavior. The voltage setting for which the maximum difference is measured is highlighted in the switching map and the resulting phase-matching condition is shown in fig. 4.21 b). For a fixed voltage value a sinc^2-like behavior of the photodiode signal depending on the wavelength is visible. The phase-matching wavelength can be obtained by determining the center of the peak. The error range in the plot is given by the electronic noise of the photodiodes.

This can be done for the different polarization converters fabricated on the chip. During the characterization I could observe that for poling periods < 21.05 µm and > 21.26 µm no

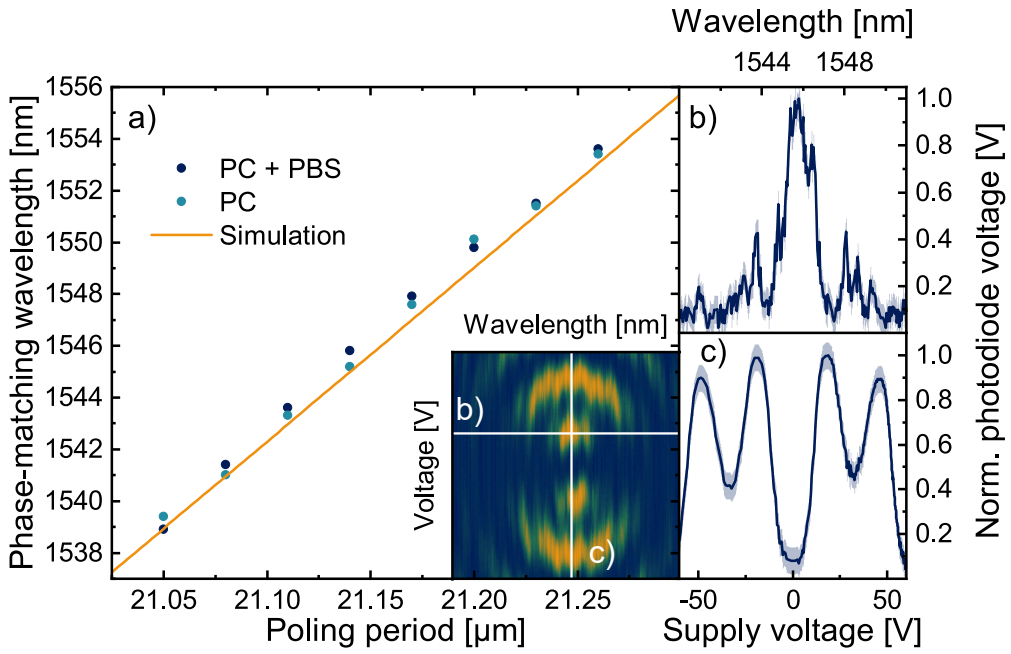

Figure 4.21: a) Phase-matching wavelength for different poling periods. From the plot we can see that the experimental results are in good agreement with the expected phase-matching condition from the design parameters. The phase-matching wavelength can be determined from phase-matching curves shown in b), by calculating the center wavelength of the peak. c) shows a voltage sweep from which the switching voltage $V_{\pi/2}$ can be determined.

modulation in the polarization was visible. These periods were at the edge of the poling holder. Therefore, it is most likely that these areas were not properly poled.

Nevertheless, the phase-matching wavelength of the remaining waveguide groups are plotted in fig. 4.21. Since a straight waveguide and the directional coupler were realized with equal poling periods, both can be compared. A good agreement between the different structures can be achieved. The mean deviation between the two structure components is (0.3 ± 0.16) nm. In addition I plotted the expected phase-matching conditions obtained from the theoretical effective refractive indices of the waveguide modes. We see a good agreement between the experimental and theoretical data. The results underline the previously presented results on the poling periods for the type-II SHG experiments and show that also larger poling periods can be fabricated with high precision and accuracy by maskless laser lithography. The error for the phase-matching wavelength is given by the accuracy of the tunable laser source (0.02 nm). Since the error is not well visible it is excluded from the plot.

In order to later perform homodyne experiments the spectral bandwidth of the polarization converter is crucial. As a figure of merit the FWHM of the obtained phase-matching

conditions is used. For all tested devices, the bandwidth is around (1.4 ± 0.05) nm. The error is given determined by the fit.

In the end, I want to determine the voltage $V_{\pi/2}$ required to switch between the two polarizations of TE and TM. As highlighted in the switching map of fig. 4.21 a) the voltage dependence is obtained for a fixed wavelength (i.e. the phase-matching wavelength). An example curve for the voltages dependent switching is shown in fig. 4.21 c). A clear modulation of the signal is visible when changing the applied voltage to the electrodes. From determining the voltage difference between the minima and maxima we obtain a $V_{\pi/2} = (16 \pm 2)$ V. The error is calculated from averaging over multiple results from different waveguide groups. Since the polarization converter has a total length of 15 mm, a voltage-length product of $V_{\pi/2} = (24 \pm 3)$ V $\cdot$ cm is calculated.

The polarization converters shown by Luo et al. [86] are half as long as the PC in this work. The shorter converter in [86] leads to a wider spectral bandwidth of the phase-matching condition. The voltage-length product calculated from the given results is higher than the reported 15 V $\cdot$ cm in [86] which can arise from a smaller overlap between the coupling polarization modes and the applied electric field. In summary this demonstration completes now two out of the three sections shown in fig. 3.3. Before continuing with the work done on integrating superconducting detectors on lithium niobate, I will briefly summarize the results from this chapter in the following.

Chapter Summary: Titanium in-diffused lithium niobate is a well known waveguide platform which has been extensively investigated in the context of classical optics experiments [85]. However, the application of Ti:LN in the field of quantum optics is an approach that is still being pursued today [86, 126, 127]. In this context, the work of Luo et. al. [86] probably represents the most complicated integrated quantum optical experiment to date for Ti:LN. For the demonstration of a Hong-Ou-Mandel interference, Luo et al. integrated multiple of the components presented in this work, which enables a comparison of the achieved performance in the scope of quantum optical experiments.

While this chapter was focused on the fabrication of integrated components in titanium in-diffused lithium niobate with a maskless laser lithography, the chip used by Luo et al. was fabricated with an optical mask lithography. With the use of a single patterning tool I was able to show that waveguides with propagation losses < 0.1 dB/cm at 1550 nm can be achieved, which is comparable to the state-of-the-art optical propagation losses in [86]. In addition, I demonstrate the realization of directional couplers. The results obtained for the directional coupler on the homodyne chip show an polarization extinction above 20 dB. The strong extinction of light in the unwanted arm of the coupler gives reason to assume symmetric waveguides. The demonstrated 20 dB exceed the PBS performance demonstrated in [86].

With the basic waveguide layer introduced I presented the results obtained for Ti:PPLN waveguides. With the help of direct laser writing I was able to show excellent agreement between the simulation and the experimentally verified phase-matching condition for poling periods ranging from $8.77 - 8.81$ µm. In the context of quantum optics the fabricated Ti:PPLN sample was used to show the generation of degenerate single photons by Lange et al. [103]. The demonstrated single-photon generation in [103] contributes to the area of quantum-state generation shown in fig. 3.3,

The differences between the simulations and the experimental results when higher order spatial modes are part of the nonlinear process need to be further investigated in the future. Nevertheless, it could be shown that an accurate fabrication of the poling periods and thus the desired phase-matching curve is achievable. The reproducibility of these results will need to be verified in the future by fabricating multiple samples with identical design parameters. The periodic poling introduced in this chapter is also required for realizing an integrated polarization converter.

The polarization converter will also utilize the electro-optical properties of lithium niobate, adding to the necessary areas shown in fig. 3.3. For this purpose I developed a lift-off process, to pattern electrodes on the underlying Ti:LN waveguide. The operation of these electrodes also works at cryogenic temperatures making them compatible with superconducting detectors. The verification and performance testing of different electro-optic modulators fabricated with this process was carried out by Frederik Thiele. More details can be found in [100, 104].

The characterization of different polarization converters fabricated on the homodyne chip was presented in this chapter. The results show a good agreement between the experimental and theoretical phase-matching conditions. An average voltage-length product of $V_{\pi/2} = (24 \pm 3)$ V · cm was measured. In comparison to the figures of merits given by Luo et al. [86], the polarization converter shown in this work exhibits a larger switching voltage which can arise from a reduced overlap of the applied electric field and the waveguide mode. The narrower spectral bandwidth of the polarization converter in comparison to the reported bandwidth in [86] results from the longer poling section realized in this work. Nevertheless, a clear conversion between the two polarization modes of the waveguide were shown.

In summary, I have illustrated that the results obtained with maskless lithography yield device performance comparable to that previously obtained with optical mask lithography [86]. Thus, for the complete integration of a homodyne detector, only the detector itself is missing. For this purpose, SNSPDs will be used in the following. The next chapter will therefore contain the steps which were taken towards the integration of SNSPDs on Ti:LN.

Integrating Single-Photon Detectors on Lithium Niobate 5

Measuring light down to the single-photon level has been in the focus of research interest for many years due to its applications in quantum communication, metrology, and quantum computing. To reach better system performance different types of detectors such as photonmultiplayer tubes (PMTs) [18], single-photon avalange diodes (SPADs) [18], transistion edge sensors (TESs) [20] and superconducting nanowire single-photon detectors (SNSPDs) [21] have been realized and tested [128]. The different detector types have different advantages and disadvantges that have to be considered when planning the detector requirements for your experiment. Photon number resolution is for example a property that is not intrinsically given for every detector type listed above. When performing weak-field homodyne experiment, we want to gain insights on correlations in the photon numbers of a signal state. Therefor, being able to measure the photon-number statistics in this scenario is highly desirable [43, 44]. SNSPDs do not offer PNR, when treated as on-off detectors. By multiplexing SNSPDs quasi-photon-number resolution can be achieved [28, 129]. Additionally, SNSPDs have never been used in the context of strong-field homodyne detection. If they prove feasible in this regard, they represent versatile detectors that can investigate the wave-like and particle-like nature of light. In this chapter I am going to concentrate on the fabrication and characterization of SNSPDs.

5.1 Basics of Superconducting Nanowire Single-Photon Detectors

Superconducting nanowire single-photon detectors are known for their near unity detection efficiency [24, 25], their low noise resulting in an outstanding signal-to-noise ratio [26] and their excellent timing properties [27]. It is important to emphasize that not all of these properties can be achieved in a single device. To realize benchmark devices, it is necessary to design the detector according to the desired requirements.

Integration of these detectors on a waveguide platform is important for fully integrated quantum circuits to perform quantum communication protocols [130], on-chip feed forward applications [65, 104] and quantum-state generation with photon subtraction [113]. That is why SNSPDs have been implemented on many different integration platforms such as semiconductors based on gallium arsenide [131], silicon [132] or silicon nitride [133], and on dielectric waveguides such as thin film lithium niobate [134] Ti:LN [94] or tantalum pentoxide [135].

Functional SNSPDs have been realized for different superconducting materials, with NbN, NbTiN, MoSi and WSi being the most common materials. In this work the superconducting detectors will be made out of tungsten silicide which was magentron-co sputtered by Varun B. Verma at the *National Institute of Standards and Technology*. Typically the nanowire width is between 80 and 200 nm. The film thickness can rang from $2 - 5$ nm depending on the superconducting material. To be single-photon sensitive, the wire is cooled down to be superconducting. Most of the time the detector is patterned in a meander fashion to fill the active area of the detector and increase the system detection efficiency. A bias current I_B is applied to the detector, which is below the critical current I_C at which the superconducting state would break down. The detection mechanism is schematically pictured in fig. 5.1 [136]. Prior to a detection event the wire is in the superconducting state as shown in fig. 5.1 a).

Upon the absorption of a photon in the superconducting material, Cooper pairs are broken, which results in a localized break down of the superconducting state (see fig. 5.1 b)). The so-called "hotspot" has a size in the range of $10 - 20$ nm and lies in the order of a few coherence lengths. The exact mechanisms of the growth of this hotspot has been under investigation for many years and a complete theory has not been derived till this point [137]. In the simplest model the nucleation of a hot-spot leads to a redirection of the current to the edge and surpassing the critical current, causing the formation of a normal region across the wire [137–140]. The hotspot-based models provides an intuitive description of the detection mechanism, but lack a quantitative consistency when applied to experimental data. The hotspot model predicts a deterministic, threshold-like response. This means that the detector will either respond to all photons of a given energy or it will not.

The experimental data instead shows an exponential decrease of the count rate when lowering the bias current I_B of the detector. This exponential decay indicates a regime in which some kind of fluctuation produces a detection event. Magnetic vortices are seen as natural candidates for these fluctuations and lead to models based on vortex assisted photon detection [90, 141–143]. In these models the absorption of a photon reduces the energy barrier for a vortex entry into the nanowire and enables the crossing of a vortex, turning the wire into the normal-state (see fig. 5.1 c)). The normal-state grows until it covers the entire width of the nanowire. The timescale of this growth is on the order of picoseconds and leads to an increase in the resistance of several kΩ.

When looking at the circuit diagram (see fig. 5.1), an SNSPD can be approximated as a switch in parallel with a large resistor and a kinetic inductance wired in series. Upon the detection of a photon the switch opens. A 50 Ω amplifier chain is connected in parallel to the SNSPD. When the detector turns normal the current is pushed out of the nanowire and into the load resistor where a voltage pulse as shown in fig. 5.1 can be measured. Once the current is redirected , the nanowire cools down and returns to the superconducting state (see fig. 5.1 e)-f)). The time it takes to rebuild the current in the nanowire depends on the detector design and the material but can be on a time scale of 10 ns [18]. During this recovery time t_D the detector is not able to detect a second impinging photon. Since single

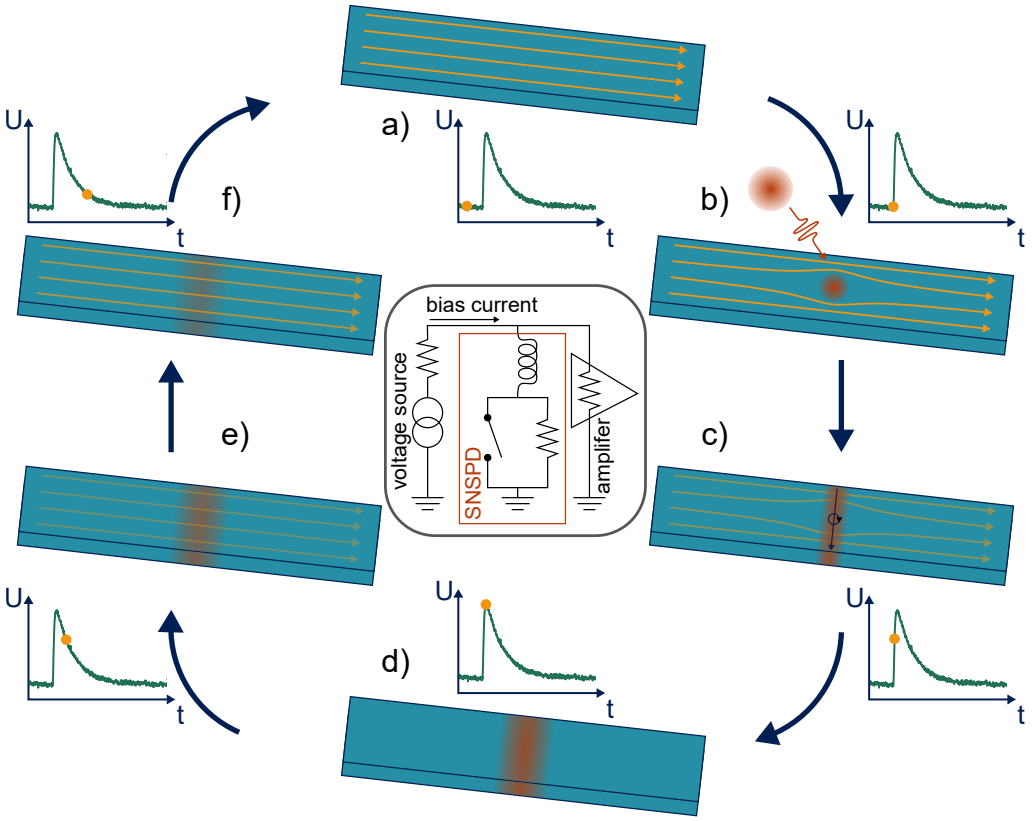

Figure 5.1: Schematic of the detection mechanism of SNSPDs. a) Prior to a detection event the nanowire is superconducting. b) When a photon is absorbed, a normal hotspot is created which is avoided by the bias current I_B. c) The increased current density lead to a vortex crossing, resulting in a normal state of the wire over the entire width. d) In the normal state the current is redirected to a load resistor. e)-f) the wire cools down again and turns back into the superconducting state. The current runs back into the wire and the detector is ready to detect another photon. The graphs added in the figure show a typical electronic response of a detection event, measured at the load resistor. The orange ball in the electronic response links it to the processes in nanowire at that time. In the box a typical readout circuit for SNSPDs is shown.

SNSPDs can not distinguish between one ore more photons simultaneously absorbed in the wire, they are considered as on-off detectors offering no photon-number resolution.

A typical trace obtained from a detection event can be seen in fig. 5.1. The rise time of the signal τ_{rise} is via $\tau_{\text{rise}} \propto L_{\text{K}}/R_{\text{N}}$ proportional to the kinetic inductance L_{K} and the normal-state resistance R_{N} of the SNSPD. The fall time of the electrical signal τ_{fall} is proportional to $L_{\text{K}}/R_{\text{L}}$ where R_{L} is the load resistor. If the fall time is too fast the current flows back into the nanowire before it is sufficiently cooled. In this so-called *latched* state, the detector does not reset itself to the superconducting state until the bias current is reset. Therefore, the detector needs to be designed with a sufficiently high kinetic inductance.

Important performance metrics for single-photon detectors are the system detection efficiency (SDE), the dark count rate, the timing jitter and the recovery time [144]. SNSPDs are often used for time-correlated single-photon counting experiments, which depend on the timing accuracy of the detector. The timing jitter characterizes the timing resolution, and is a measure of the fluctuations in the delay time (δt) between the registration of the photodetection pulse and the absorption of a photon in the detector.

In the photon-depleted environment of quantum applications, a high detection efficiency of the detector is of great importance to reduce the loss of a state under investigation. In the system detection, the collection efficiency (the photon must reach the detector), the absorption efficiency (the photon must be absorbed) and the internal efficiency (the absorbed photon leads to a signal) are included. With keeping this in mind, system detection efficiencies up to near unity were achieved [24, 25]. To reach these high SDEs the detectors are illuminated from a fiber, which is well aligned to the detector. A distributed Bragg reflector is build around the detector to increase the collection and absorption efficiency.

The geometry for integrated SNSPDs on a waveguide differs from the fiber packed solution. The light guided in the waveguide needs to couple through the evanescent field to the detector. A small overlap between the guided mode and the detector leads to lower SDEs [94] and vice versa. In Ti:LN, this effect is particularly visible. For integrated SNSPDs on Ti:LN a maximum system detection efficiency of 0.7 % could be measured [94].

To improve the on-chip detection efficiency, I investigated two different approaches. The first one is based on manipulating the guided mode of the waveguide with a high refractive index medium (see chapt. 5.2). With this, the light is guided closer to the interface between the waveguide and the superconducting detector and therefore the evanescent field coupling to the detector is increased. For a second approach (see chapt. 5.3) we can increase the SNSPD size and wire width to increase the detector absorption.

5.2 Mode Manipulation in Ti:LN with Silicon Tapers

Just like waveguiding can be achieved in a dielectric medium with a higher refractive index than its surrounding, we can use different materials with a wide scope of refractive indices to manipulate the spatial distribution of a waveguide mode. In qualitative terms,

the refractive index contrast is a measure of how strongly a spatial light distribution can be manipulated. A high refractive index contrast has a strong influence, while a smaller contrast causes only slight changes.

The use of additional layers to influence the spatial mode distribution has proven effective [145]. Especially in silicon photonics, where the mode size of waveguides is comparatively small, tapers have been used to increase the mode size so that the waveguide can be coupled to an optical fiber [145–147].

By applying a taper with a higher refractive index than the Ti:LN waveguides, we aim to achieve a stronger mode confinement. We choose silicon as the material for the taper. With its high refractive index of $n_{\mathrm{a-Si}} = 3.48$ and excellent patterning properties, it is a promising candidate for strong manipulation of the Ti:LN mode.

To verify the mode manipulation, FEM simulations were performed with the help of Lena Ebers [94]. The model and the results of the simulations are discussed below. The fabrication and experimental verification of the mode manipulation are then presented in more detail.

5.2.1 Simulation of Silicon Tapers

The structure we want to study is shown in fig. 5.2. A silicon layer is deposited on a Ti:LN waveguide, which is structured in the form of a linear taper. For the simulations, the silicon layer is encapsulated with a protective silicon dioxide layer. For the initial spatial mode distributions shown in fig. 5.2 a silicon thickness of $h = 60$ nm was picked.

Without tapering (i.e., $w_{\mathrm{Si}} = 0$ µm), the spatial mode distribution of the Ti:LN waveguide is determined as described in chap. 4.1.1. The mode distribution is shown in fig. 5.2 b). Looking at the end of the taper (i.e. $w_{\mathrm{Si}} = 3$ µm), the mode distribution has changed drastically (see fig. 5.2 c)). For the now so called silicon mode, mode sizes of $\mathrm{FWHM_x} = 1.8$ µm and $\mathrm{FWHM_y} = 0.6$ µm were calculated. Therefore, the mode size is reduced to 24 % and 11 % of the initial mode size.

The taper is now supposed to adiabatically couple the energy from the pure lithium niobate mode to the silicon mode. Therefore, the influence of the width and the height of the silicon stripe was analyzed. For the results in this chapter, we concentrate only on the TE mode since all structures were optimized for the TE polarization. If one would like to consider TM, the film thickness would need to be adjusted since the effective index of the mode changes.

In order to analyze the influence of the taper on the mode properties of the structure, we calculate the effective refractive index of the TE modes for different widths of the silicon stripe on-top of the waveguide. *Comsol* was used to perform these simulations. For the model we assume the theoretical refractive index of silicon and the refractive index profile of the 7 µm wide Ti:LN waveguide calculated in chap. 4.1.1. The results of the simulations

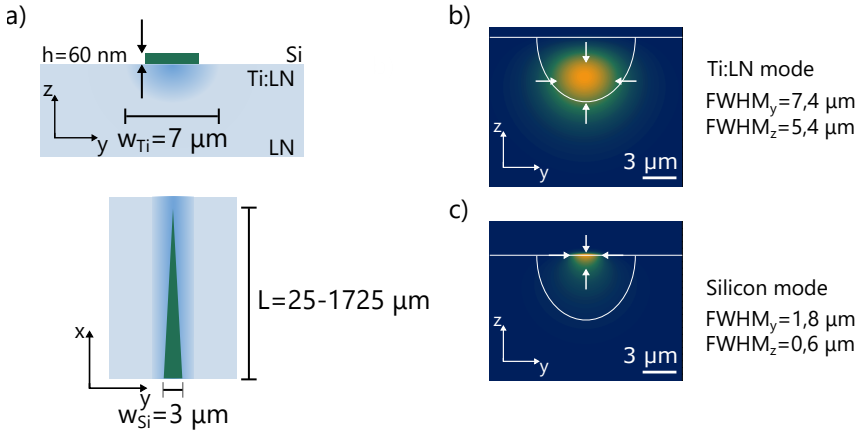

Figure 5.2: a) Titanium in-diffused waveguide with a 60 nm thick silicon taper on-top. The length of the taper is increased from 25 – 1725 µm. b) Simulated mode distribution of the titanium in-diffused waveguide without a taper. c) Simulated mode of the hybrid structure with the silicon taper and the titanium in-diffused waveguide. For each mode the full width at half maximum (FWHM) is given.

for the two different silicon stripe thicknesses of $h = 60$ nm and 65 nm can be seen in fig. 5.3.

For the following discussion, we will first concentrate on the structure with the thickness of 60 nm. When there is no additional taper ($w_{Si} = 0$), we obtain only a single mode, titled LN TE_0. The field distribution calculated is the TE mode of the Ti:LN waveguide. When increasing the width of the silicon stripe the effective refractive index increases since more light starts to propagate in the region of the silicon with the higher refractive index.

If the width of the silicon stripe is big enough, a hybridization of the mode can be obtained as is indicated by the avoided crossing section of the red and blue curve in fig. 5.3. The combined mode, where light propagates in the silicon and in the lithium niobate, is abbreviated with LN/Si TE_0. The light of the mode with the higher effective refractive index is mainly confined in the silicon and is therefore named Si TE_0. In the avoided crossing area, the two modes are phase matched and power can be transferred from one mode to the other. Keeping the taper at this width the energy will be transferred to the mode with the higher effective index (i.e. Si TE_0).

For long taper length, the width of the silicon strip increases only gradually. Therefore, the two modes Si TE_0 and LN/Si TE_0 remain in the coupling regime of the avoided crossing for a longer physical distance in the taper. As a result a higher amount of energy can be transferred to the Si TE_0 mode. Hence, we expect a stronger mode confinement when we increase the taper length at a fixed final width. This correlation is plotted in the inset of fig. 5.3 a).

Increasing the width of the silicon stripe further increases the effective refractive index of the silicon mode (Si TE_0), which will also reduce the coupling so that less power will

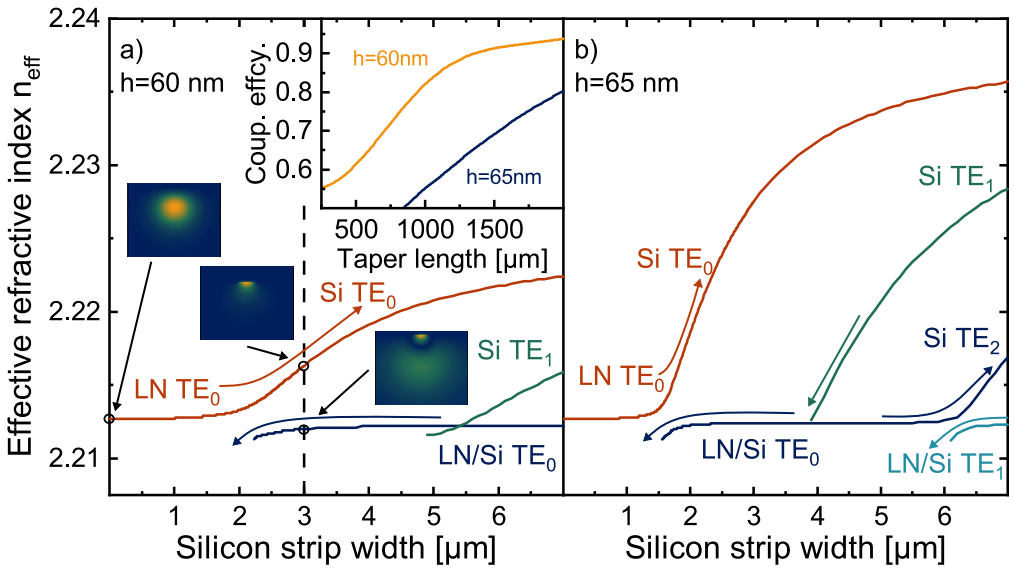

Figure 5.3: a) Calculated effective refractive index of hybrid structure based on titanium in diffused waveguides and a silicon stripe with the thickness of a) 60 nm and b) 65 nm. The width of the silicon stripe is changed leading to different modes appearing in the structure. The inset shows the coupling efficiency to the Si TE_0 mode when increasing the taper length. The arrows indicate the transition of the mode.

transfer back to the hybrid mode (LN/Si TE_0). For our purpose we want to confine the light close to the interface between the silicon and the lithium niobate, so that the light can couple to a superconducting detector placed in between the two structures. Comparing this with the mode pictures shown in fig. 5.3 a) we want the light to couple to the Si TE_0 mode. To decrease the number of possible supported modes, we limit ourselves to a final taper width of 3 µm.

Another parameter that can be changed is the thickness of the silicon stripe. The influence can be quantified from comparing fig. 5.3 a) and b). Although hybridization of the mode still occurs, the effective refractive index increases stronger with the width of the silicon stripe. This leads to a shorter effective coupling area where power can be transferred into the silicon mode. In the inset of fig. 5.3 a) it is clearly visible that an increase of the film thickness by 5 nm significantly decreases the coupling efficiency. Additionally, modes of higher order appear at smaller stripe width. Since the simulations indicate a strong influence of the film thickness on the taper performance, it is important that the silicon height can be controlled preciously and is homogeneous over the sample.

5.2.2 Fabrication of Silicon Tapers

To realize such a taper structure as shown in fig. 5.2 a) Ti:LN waveguides are fabricated with a width of 7 µm. The sample is cleaned with acetone and isopropanol for 10 min each

Table 5.1: PECVD process parameters used to deposit an amorphous silicon film.

Process Gas	Flowrate	Pressure	Temperature	RF-Power
SiH_4	400 sccm	1000 mTorr	300 °C	10 W

at 40 °C in an ultrasonic bath to remove residual impurities from previous fabrication steps. The remaining fabrication steps are depicted in fig. 5.4.

For the fabrication of the silicon tapers we deposited amorphous silicon (a-Si) with a plasma enhanced chemical vapor deposition (PECVD) process based on silane (SiH_4) as a process gas. Afterwards the negative resist AZ 15nXT is spin coated on the sample and exposed by a direct laser lithography. After developing, the silicon film is dry etched with a RIE-ICP (reactive ion etching inductive coupled plasma) system. In a final step, the taper is encapsulated with a protective silicon dioxide layer. The different process steps will be discussed in more detail in the following.

In a PECVD the process gas is ionized by an applied RF electric field. The radicals can be accelerated to the substrate surface placed in the system. The chemical reaction of silane to silicon that takes place in the chamber causes an amorphous silicon film to be deposited on the sample [148]. In the scope of this work, we used an established recipe for a-Si. The process parameters are listed in the tab. 5.1. For the deposition of silicon on lithium niobate the temperature of the substrate holder is slowly ramped up from 50 °C to 300 °C with roughly 3 °C/min to avoid pyroelectric effects from the lithium niobate.

To characterize the films, we performed ellipsometric measurements to determine the growth rate and the refractive index of the deposited silicon films. We investigated three different films with a process time of 308 s, 246 s and 231 s. The film thicknesses obtained by the ellipsometer were (80 ± 2) nm, (64 ± 2) nm and (60 ± 2) nm therefore resulting in a growth rate of (0.26 ± 0.01) nm/s. With the ellipsometric data we were also able to determine the refractive index of the films to be $n_{\mathrm{a-Si}} = 3.48$ which agrees with the expected value [149].

After film deposition the film needs to be patterned such that tapers, as displayed in fig. 5.2 a), remain on the waveguide. Therefore, negative *AZ 15nXT* resist is spin coated on top of the sample. We chose this resist due to its resistance against different etching processes and its relative thickness. We chose 6000 rpm as the spin coating parameters with a ramp of 5 s and a duration of 3 s, resulting in a resist thickness of 2.5 µm. The resist thickness was measured with a profilometer. The softbake is done at a temperature of 100 °C for 13 min in a convection oven.

After the softbake we determine the exposure parameter for the lithography process with the direct laser lithography system. For the patterning of the tapers the WM II is chosen to have accurate alignment to the waveguide and pattern the tip of the taper as precisely as possible. The optimized lithography can be determined with the same process as previously described in chap. 4.1.2 The parameters used for the final structure are listed in tab. 5.2.

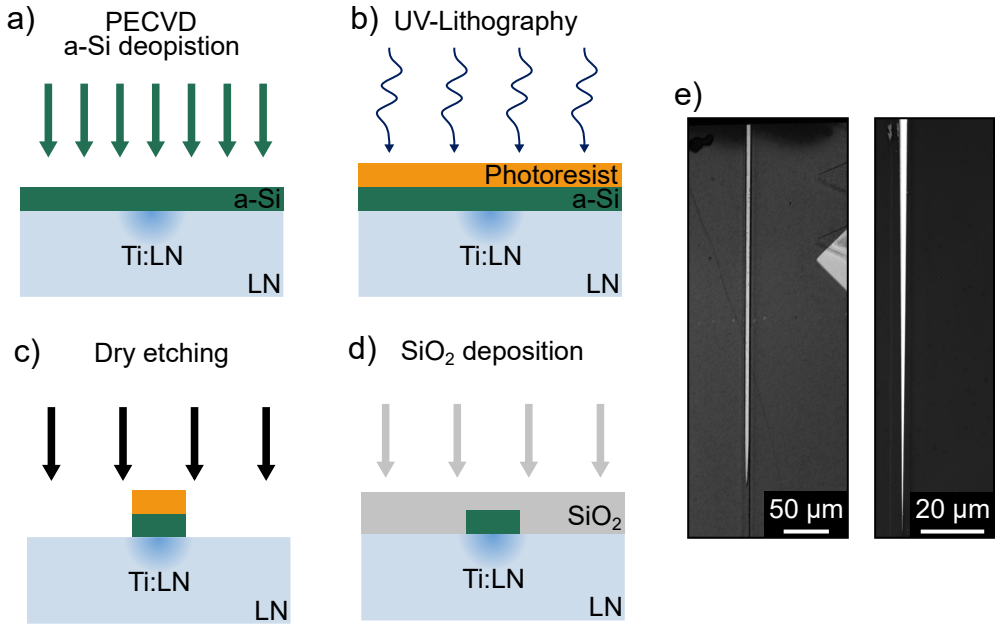

Figure 5.4: Fabrication process for silicon tapers on lithium niobate waveguides. a) Deposition of amorphous silicon (a-Si) by PECVD using SiH_4 as process gas. b) UV lithography with a direct laser writer. AZ 15nXT is the used negative photo resist. c) After developing, the remaining silicon film is anisotropically dry etched. d) In a last step a protective silicon dioxide (SiO_2) layer is deposited on the silicon taper. In e) laser microscope images of the two different taper designs are shown. The left has a fixed tip length of 50 µm. For the right taper design the length of the taper tip was varied.

For further processing of the resist, a post-exposure bake at 105 °C for 13 min is done. The developing of the resist is done with 85 % of the developer *AZ 726 MIF* diluted with 15 % of water. The developing time was determined to be 1 min 30 s.

The taper structure written in the resist can be transferred to the silicon film underneath with a dry etching process in a RIE-ICP machine. With the inductive coupled plasma a high anisotropic etching process of silicon can be realized leading to vertical sidewalls for the taper structures. For our structures an established etching process based on SF_6 and C_4F_8 as process gases is used. The parameters can be found in tab. 5.3.

Since lithium niobate has a high chemical stability, it is not attacked by the etching process of the silicon. To remove the unprotected silicon an etching time of 30 s is used. In the

Table 5.2: Lithography parameters of the negative photoresist *AZ 15nXT* for silicon on lithium niobate with the WM II.

Photo resist	Focus	Power	Filter
AZ 15nXT	−2 %	52 mW	12.5 %

Table 5.3: RIE-ICP process parameters for etching silicon on lithium niobate. During the etching process the helium backside cooling is turned on.

Process Gas	Flowrate	Pressure	Temperature	RF-Power
SF_6/C_4F_8	40/50 sccm	10.5 mTorr	900 °C	32 W

etching process SF_6 is used to etch the silicon while C_4F_8 passivates the etched surface of the silicon such that almost vertical sidewalls for deep etching (couple 100 nm) can be achieved [150].

In an additional step, the remaining resist is removed with *TechniStrip NI555*. For its proper functionality the *TechniStrip* is heated up to 70 °C in an ultra-sonic bath. After 10 min of *TechniStrip*, remaining residuals can be removed with an additional isopropanol step as described before.

As a protection layer a 400 µm thick silicon dioxide layer is deposited to the sample to cover the tapers and protect them from breaking during the polishing step (see fig. 5.4 d)). The silicon dioxide is deposited with an electron-beam evaporator.

To visualize the influence of the taper on the lithium niobate waveguide mode, we want to image the mode distribution of the waveguide in different taper positions. Therefore, we fabricate the tapers close to the edge of the sample. Markers are added alongside the tapers. I polished the end facet as close as possible to the markers that serve as a reference point for the length of the taper.

Two different taper designs were fabricated in the scope of this work. For a first design the taper length was kept at a constant length of 50 µm. The length of the straight silicon stripe was varied over multiple waveguide groups. A schematic of the design is depicted in fig. 5.5 a). A laser microscope image of an example taper is show on the left of fig. 5.4 e). In addition a tip of the marker is visible which was used for alignment during the polishing process.

A schematic of the second taper design is pictured in fig. 5.5 b). For this design the length of the taper tip is varied in the range from $0.08 - 1.75$ mm. With this design we expect to have a more efficient coupling to the desired Si TE_0, since the taper remains for a longer distance in the phase-matched condition. A laser microscope image of the fabricated taper can be seen on the right of fig, 5.4 e).

Although the resolution of the maskless lihtography limits the minimum tip size, the important taper width in the $2 - 3$ µm range, where hybridization and mode coupling occurs according to fig. 5.3 a), can be patterned with high accuracy. To experimentally verify the mode manipulation of the Ti:LN mode, mode images at the end of the tapers were taken. In the next section I will give a more detailed description of the setup used and discuss the obtained results.

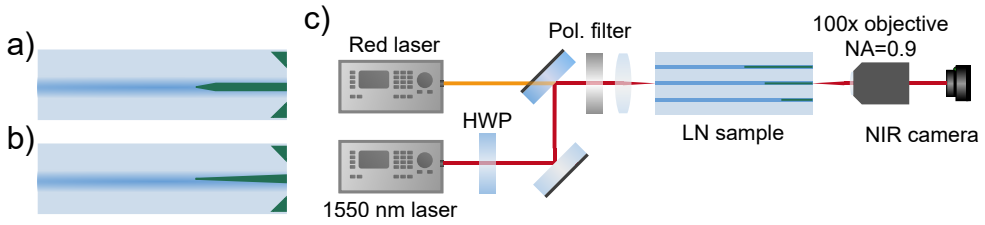

Figure 5.5: a) Schematic of the first tested taper design with a constant tip length of 50 µm and varying straight strip length. b) Second taper design with varying tip length and no straight strips. The markers used for polishing are also included. c) Setup used to image the mode at the end of the chip. A microscope objective with a 100-times magnification and a numerical aperture (NA) of 0.90 is used. The half-wave plate (HWP) and the polarization filter (Pol. filter) are used to set the input polarization to TE.

5.2.3 Mode Imaging of Silicon Tapers

For the first tested structure, we kept the tip of the taper at a constant length of 50 µm and changed the length of the straight silicon stripe. A schematic of the design is shown in fig. 5.5 a). Two samples were fabricated with the two different film thicknesses of 60 nm (sample A) and 64 nm (sample B).

The optical setup used to image the mode distribution is displayed in fig. 5.5 c). The waveguide coupling is executed with a red alignment laser, while a narrowband continuous wave (cw) linearly polarized laser at 1550 nm is used for mode imaging. Outcoupling of the chip was done with a microscope objective with a 100-times magnification and a numerical aperture of 0.90. The objective results in a minimal structure size of ≈ 1.7 µm.

Since different lengths of tapers were fabricated on different waveguide groups, the change in the spatial mode distribution can be mapped alongside the taper structure length. For the first design with a constant tip length and straight silicon strip with increasing length, different mode images that were taken along the taper can be mapped on a position line.

The two position lines for sample A and B are pictured in fig.5.6 a) and b). From measurements with the laser microscope the length of the taper was estimated. With this we can relate the mode images, to a specific location in the taper structure. The mode images shown in fig. 5.6 are placed such that they are roughly at their actual position.

Looking first at sample A with a silicon thickness of 60 nm, a clear mode manipulation can be seen. For a taper length of $\approx$ 600 µm the light is mostly confined in a narrow area with only small fractures of light remaining in the substrate. The transition form the LN TE_0 to the Si TE_0 can not be well identified. At $\approx$ 550 µm the spatial mode distribution is comparable with the hybrid LN/Si TE_0 from the previously performed simulations. When increasing the length of the silicon structure further, the light continuous to be strongly confined in the silicon mode.

To verify the influence of the silicon film thickness, sample B with $h = 64$ nm can be compared to the results obtained from sample A. The mode images alongside the position line are displayed in fig. 5.6 b). Since the mode images do not change with increasing structure length only three mode images are given, two at the beginning and one at the end of the structure. The spatial mode distribution of all mode images is comparable to the hybrid LN/Si TE_0 mode. The explanation can be given by the results from the simulations for a film thickness of 65 nm. Since the difference in the effective refractive index of the Si TE_0 and LN/Si TE_0 has now increased there is a reduced coupling between the two modes. It is expected that in order to improve the energy transfer to the Si TE_0 mode, the taper tip length needs to be increased.

For this reason, the structure will be simplified only to the taper tip and the tip length will be varied. In the next test the silicon film thickness will be 60 nm since a stronger mode manipulation was visible for this thickness. Before we continue with this, I want to consider the losses introduced by the tapers.

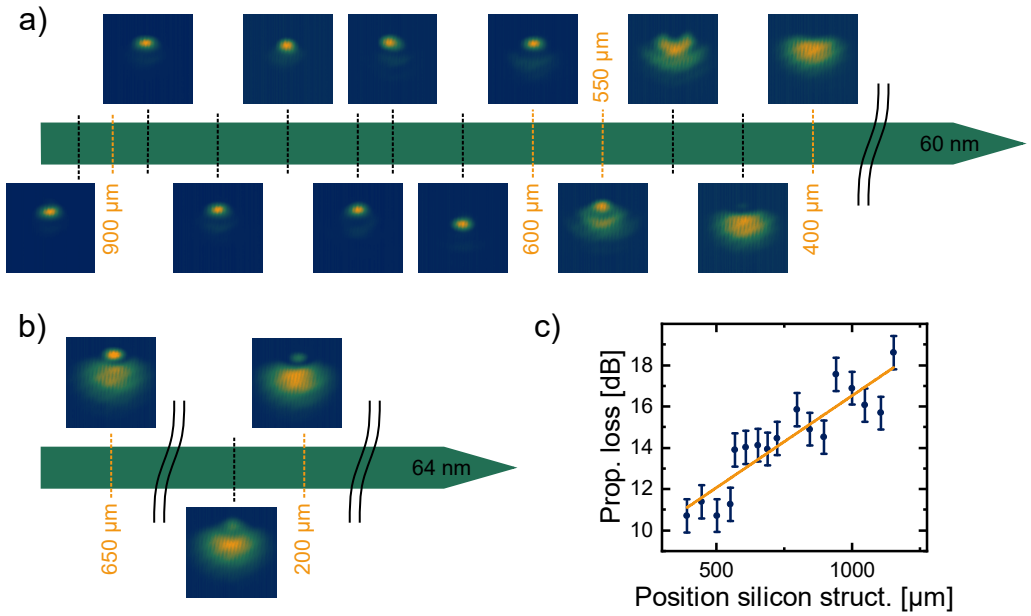

Figure 5.6: Two position lines for the two samples with a) $h = 60$ nm and b) $h = 64$ nm are shown. The mode images taken along the waveguide are placed so that they can be roughly related to their actual position in the silicon taper. For the smaller thickness the loss was estimated from the brightness of the mode images. The calculated loss in dependence of the silicon structure length is plotted in c).

Using the mode images taken for Sample A, an attempt can be made to estimate the losses caused by the taper. The mode images were taken with equal camera settings regarding the integration time. The integration time was set such that for the brightest mode image no overexposure of the camera was visible. Determining the total intensity of the guided mode

was done by summing up all data points in one mode image. To estimate the loss introduced by the taper, we compare the total intensity obtained for a specific taper structure to the average total intensity calculated for all Ti:LN waveguides without an additional taper on top.

The normally used method to determine the propagation losses of Ti:LN waveguides, based on Fabry-Pérot measurements is not suitable for the silicon tapers. The calculations of propagation losses must take into account the effective index of the guided mode. Since n_{eff} changes significantly along the waveguide due to the taper, we restrict ourselves to estimating the loss with the previously described method.

The calculated loss in dB in dependence of the position in the silicon taper is plotted in fig. 5.6 c). A clear increase of the propagation losses with increasing taper length can be identified. The error given for the propagation loss is ±0.8 dB and is estimated from the standard deviation when averaging the total intensity obtained for all Ti:LN waveguides without any additional tapers. Thus, we include the fluctuations in the Ti:LN waveguides and the uncertainty in the measurement setup in the error.

To quantify the introduced loss further we use a linear regression. This results in a propagation loss of (9 ± 1) dB/mm of silicon taper length. The rather high propagation loss should be seen as a rough estimation and an upper limit of the introduced losses. When looking at the structures with a laser microscope clear defects in the silicon taper structures were visible. They may result from resist inhomogeneities in the immediate proximity of the end facet of the sample, impurities on the sample, imperfect polishing or residuals of the polishing solution. Therefore, the propagation losses are expected to decrease drastically with increasing experience in sample handling. Especially in this case, where the light is strongly confinded, imperfections in the taper structure or impurities can drastically increase the propagation losses due to enhanced light scattering.

As previously mentioned for the second test the taper structure is further simplified and consists now only of the taper tip. The length of the taper tip is varied from 25 – 1725 µm. With more experienced sample handling the fabricated tapers are much cleaner with reduced amounts of imperfections. When attempting to estimate losses, the calculated intensity remains constant and varies within the error range estimated for the previous measurement. Therefore, there is no clear evidence of a significant loss increase when adding the tapers to the Ti:LN waveguide.

When analyzing the spatial mode distribution, an in-house software can be used to calculate the FWHM of a mode image. This can be done for all taper length ranging from 25 – 1725 µm in 25 µm steps. The results are shown in fig. 5.7. In the plot three different mode images are given for the three different cases of no mode manipulation (LN TE_0), a mode hybridization (LN/Si TE_0) and strong mode manipulation (Si TE_0). From the given results a clear transition from the unperturbed LN TE_0 to the strongly confined Si TE_0 is visible.

With a short taper length, the mode is clearly dominated by the hybridized mode with a larger mode size. For long taper length > 1250 µm, a decreased mode size is clearly visible. For the longest taper structure a minimum FWHM of $w_y = 2.3$ µm and $w_z = 1.9$ µm is

calculated. Thus, the mode has been reduced to 31 % and 35 % of its initial mode size. The long taper length results in a slowly increasing width of the silicon strip, allowing more light to couple to the silicon mode, when the width is in the avoided crossing region, as shown in fig. 5.3 a). With the given objective, the obtained results are restricted by its resolution. To determine the actual mode size and the spatial mode distribution more precisely, an objective with a higher numerical aperture would be required. Nevertheless, the detection efficiency of a SNSPD positioned between the Ti:LN waveguide and the silicon taper would increase due to the spatial mode changes.

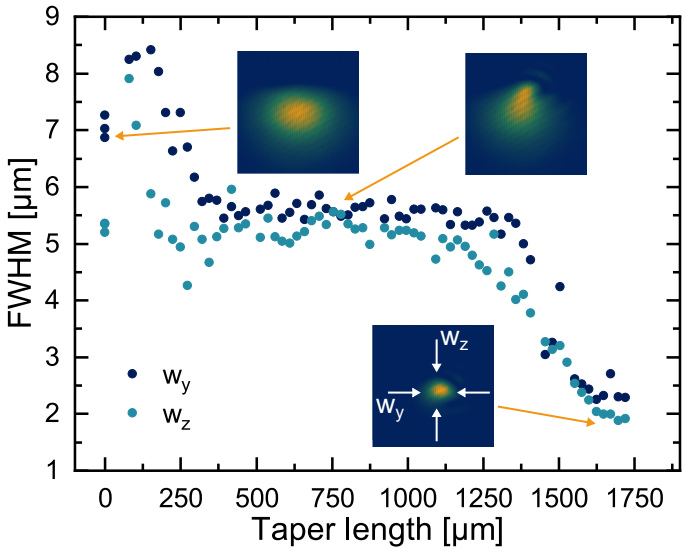

Figure 5.7: The FWHM obtained from the measured spatial mode distribution is plotted in dependence of the taper length. Mode distributions for the LN TE_0, LN/Si TE_0 and Si TE_0 mode are included in the figure.

Although there is a good agreement between the simulations and the experimental results regarding the strong mode manipulation, further efforts need to be made to understand the transition between the LN TE_0 and Si TE_0 mode. Therefore, one could include fabrication imperfections in the simulation to see how this results in the coupling of the different contributing modes.

In order to achieve a similar mode manipulation for shorter taper length, a more advanced design of a taper could be chosen. In this case a taper would consists of three sections: a short taper from $w = 0 - 1.5$ µm, a slowly changing taper from $w = 1.5 - 2.5$ µm, followed by a short taper from $w = 2.5 - 3$ µm. In this scenario, we focus on the width region where hybridization of the modes occurs and a more efficient coupling of energy to the silicon mode is achieved.

Although the results have shown that the spatial mode in Ti:LN waveguides can be

strongly influenced, this approach will not be pursued further. The tolerances that have to be achieved with respect to the layer thickness of the silicon cause difficulties with regard to the reproducibility of the results.

Both the experiments and the simulations show that a layer thickness deviation of > 4 nm already causes the behavior of the system to change drastically. The initially assumed advantage of using silicon, due to its high refractive index, now turns out to be more of a challenge. To overcome this, a medium with a lower refractive index can be used. Silicon nitride (Si_3N_4) is a promising candidate. To structure Si_3N_4, the same processes can be used as for silicon. In addition, experimental results have shown that with sufficient control over the PECVD process, silicon nitride can be produced with different silicon and nitrogen concentrations. For a high concentration of silicon, the refractive index approaches that of silicon [151]. This degree of freedom would create an interesting hybrid platform with a high degree of flexibility. Nevertheless, this requires excellent process control.

Of course, the stronger confinement by structures with a higher refractive index contrast also offers other advantages. With the stronger confinement of the $SiTE_0$ mode, significantly more components could be fabricated on a lithium niobate chip. Interesting components such as ring resonators or waveguide curvatures with small radii of curvature, which would otherwise not be feasible for Ti:LN waveguides, are thus imaginable. We expect that the combination of the presented tapers with SNSPDs on Ti:LN would improve the system detection efficiency. For systems with strong confinement like silicon photonics, on-chip SDE of 91 % were realized [132]. Nonetheless, since the current process lacks the required control to fabricate the taper structures in a reproducible fashion it is important to ask the question how the detector could perhaps be modified to increase the system detection efficiency? To gain insights on this question, micrometer-wide SNSPDs will be considered in the next section.

5.3 Realizing Micron-wide SNSPDs on Silicon

Single-photon detectors based on superconducting nanowire single-photon detectors (SNSPDs) have been previously introduced in the introduction (see. chap. 3 and in the beginning of this chapter (see chap. 5.1). Before delving into the experiments I have conducted in the scope of this work, I will first give a brief overview of the status quo regarding SNSPD fabrication.

SNSPDs composed of tungsten silicide (WSi) usually have a film thickness of $\approx$ 5 nm. The wire width can range from 80 – 200 nm. For the integration of SNSPDs on Ti:LN waveguides, a detector geometry of 160 nm wide and 400 µm long wires with 160 nm spacing was used [94]. With only 4 detector lines overlapping with the waveguide, the small overlap between the optical mode and the cross-section of the device results in a low system detection efficiency.

Recent experiments have shown that by decreasing the film thickness further, the wire width can be extended to the micrometer range, which may enable the fabrication with optical lithography [96, 98, 152–159]. The wider wires lead to a larger cross-section, increasing the on-chip SDE. In addition, optical lithography could lead to longer wire length and faster and cheaper manufacturing compared to conventional electron beam lithography.

With this advantages in mind, we wanted to show that micron-wide SNSPDs can be fabricated with a maskless laser lithography. To prove feasibility, the detectors were first patterned on silicon. The superconducting films used in the scope of this work were deposited with magnetron co-sputtering by our collaborators at NIST.

Since the fabrication of the detectors will be similar for silicon and lithium niobate as a substrate, I will give a brief description of the fabrication in this chapter. The parameters used for the optical patterning on lithium niobate will be given in this chapter.

5.3.1 Fabrication of Micron-wide SNSPDs with Direct Laser Lithography

The fabrication process starts as previously mentioned with magnetron co-sputtering a 2.6 nm thick tungsten silicide film on the desired substrate. Two separate targets of silicon an tungsten are used for this purpose. More details on the deposition process can be found in [155].

For the photoresist, the 0.9 µm thick negative *AZ nLof 2020* is used. The resist is spin coated with 6000 rpm for 3 s and a ramp of 5 s. Soft- and post-exposure bake are carried out at 110 °C for 15 min in a convection oven. The exposure parameters for both, silicon and lithium niobate, can be found in tab. 5.4. After the post-exposure bake the resist is developed with *AZ 726 MIF* which is diluted with 15 % of water. The developing time is 30 s. To be resistant against the dry etching process a hardbake at 120 °C for 15 min is done.

Table 5.4: Lithography parameters of the negative photoresist *AZ nLof 2020* for silicon and lithium niobate as a substrate. For the exposure the WM II was used.

Substrate	Focus	Power	Filter	Intensity
Silicon	17 %	58.06 mW	5 %	35 %
Lithium niobate	25 %	20 mW	5 %	100 %

To pattern the resist structure in the tungsten silicide layer, the same dry etching process is used as for the silicon tapers. The exact process parameters can be taken from tab. 5.3. In order to remove the residual resist the previously described standard process based on *TechniStrip* is used.

In the progress of designing and fabricating functional detectors that respond to single photons, different detector geometries and designs were tested. The differences and the concrete design parameters will be given, when the results are discussed in the following.

5.3.2 Experimental Testing of Micron-Wide SNSPDs

When it comes to the question on how to design a superconducting detector, there are a number of considerations. In the following we will consider different detector geometries and sizes and characterize their properties at room temperature. At cryogenic temperatures the performance of the detectors in terms of their ability to measure single photons is being tested. The results presented in this chapter were obtained together with Jan Philipp Höpker.

In this work, several samples with a variety of different detector geometries were fabricated and their influence on the detection performance was investigated. Basically, each detector consists of a long wire that can be oriented in any way. In our case, we have fabricated line detectors, meander detectors, and shorter line detectors with an inductor connected in series. A schematic representation of the detector geometries is shown in fig. 5.8. With the serial inductor design we can pattern detectors with a small active area, which will less likely be influenced by fabrication imperfections. The meander delivers a dense active area with possible long nanowires. The line detector is the simplest design with a largely spread out active area.

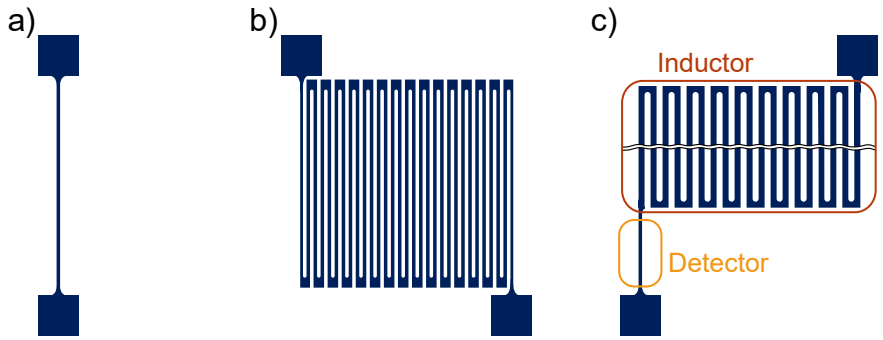

Figure 5.8: Different possible detector geometries. In a) a line detector is pictured. b) shows a meander detector. c) combines a shorter line detector with a much wider serial inductor. The The different detectors are not to scale.

In a first test, we focus on the line detector design. We fabricated detectors with widths of 2, 3 and 4 µm and lengths ranging from $1 - 6$ mm. Before cooling down the detector we measured the resistance of the detectors at room temperature. As expected the resistance was linear dependent on the wire length. To investigate the detectors at cryogenic temperatures the detectors were bonded and cooled down to temperatures < 0.8 K. In order

to characterize the responsivity of the detectors to impinging photons, an SMF-28-fiber at a distance of $\approx$ 2 mm from the fiber end to the sample surface is used for targeted flood illumination. In flood illumination, a sample with multiple devices is illuminated by a single light source. As a light source we used an attenuated pulsed lasers of 1550 nm wavelength with a repetition rate of 500 kHz. In contrast, for commercial detectors with high system detection efficiencies, the detectors are individually packaged with an optical fiber.

Due to the flood illumination, we may not reach high system detection efficiencies. However, in this case we are only interested in the internal efficiency, which quantifies the probability that an absorbed photon will result in a measurable detection signal. Collection and absorption performance can then be optimized by carefully designing the cavity surrounding the detector to achieve near unity SDE [24].

To quantify the internal detection efficiency, we apply a bias current to the detector. While the power at which we illuminate the detector remains constant, we sequentially increase the bias current and measure the count rate of the detected photons using a time-tagging module. Upon the detection of a photon an electrical response function as shown in fig. 5.1 is expected. If the voltage pulse exceeds the threshold set on the time tagger input, the time-tagging module registers this event as a detection event. For the time-tagging module a threshold of 50 mV is set. The typical electronic response of a SNSPDs is normally amplified to a peak voltage of $\approx$ 100 mV. With this we are able to measure the bias-dependent count rate of the detector. When characterizing the internal detection efficiency with this method it is important that the maximum of the measured count rate is significantly above the noise floor and below the repetition rate of the laser. By adjusting the attenuation of the laser, we can characterize the detectors in the ideal operation window.

It is expected that as the bias current increases, the count rate increases. Thus, an increase in the bias current ensures an increase in the internal detection efficiency. The count rate will saturate for high bias currents. If the bias current is increased, the probability of an electronic detection event occurring after the absorption of a detection event increases. Since the probability must be between 0 and 100% we can achieve a saturation of the count rate at high bias currents. At this point we conclude that every absorption of a photon leads to a measurable detection event. When the plateau is reached we talk of a saturated internal detection efficiency. We aim to achieve this saturated internal detection efficiency when characterizing the detectors, as it indicates that the internal detection efficiency is not limited by fabrication constraints that limit the maximum bias current.

Unfortunately, the line detectors bonded in the first test did enter the superconducting state, but an increase in bias current caused the detectors to latch immediately. We concluded, that this is due to the low kinetic inductance of the devices tested. As previously described, the kinetic inductance sets the timescale at which the current returns to the nanowire. If the kinetic inductance is two low, the current returns to the wire before it is superconducting and keeping it therefore in the normal state. To quantify the kinetic inductance of our device we can look at the number of squares ($\square$) the detector has. The number of squares

is defined as the length of the wire L divided by the width of the wire w (i.e. $\square = L/w$). The detectors used for the first test had a number of $\approx$ 2000 and $\approx$ 1700 squares.

Based on the results from the first test, we patterned larger detectors regarding the number of squares. We also changed the design of the detector to a meander, to have a denser detector. For the meander design, we hope to reduce the influence of inhomogeneities of the film and fabrication defects on the detectors, since the detector is patterned on a smaller surface area. The fill factor of the meander detectors was 25%. In this test three different detectors with a wire width of 2 µm and 7500, 13500 and 21000 squares were bonded and cooled down. An SEM image of the 7500 square detector is shown in fig. 5.9 a).

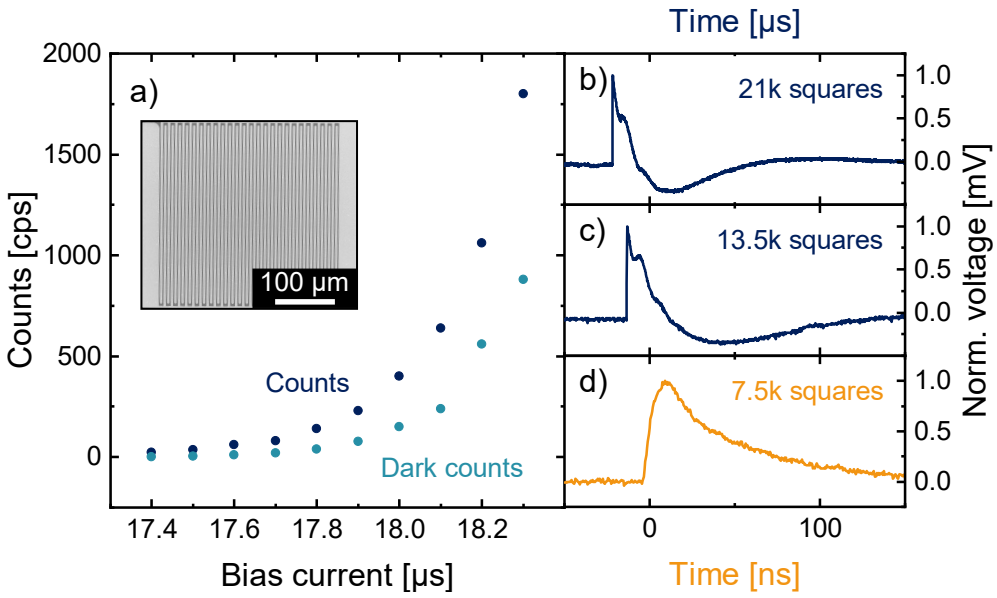

Figure 5.9: a) Bias-dependent count rate of detection events in a 2 µm wide meander detector with an unfolded length of 3.75 mm. b)-d) show the electrical detector response to impinging photons for three meander detectors of different size, all having a width of 2 µm. The SEM images shows the 7500 square meander detector. For the electrical response of b) and c) the time scale is three orders of magnitude larger. The error on the bias-current is derived from the count rate limited by Poisson noise, which is negligible.

All three detectors were sensitive to impinging photons. The electrical response of the three detectors can be seen in fig. 5.9 b)-d). For the smallest meander with 7500 squares, the trace looks like the expected electrical response also depicted in fig. 5.1. Upon the detection of a single photon, we have a rapid voltage increase on the load resister, followed by a slow decay dictated by the load resistor and the kinetic inductance of the detector. Even though we were able to measure a trace for the two bigger detectors (see. fig. 5.9 b) and c)), they latched after a few detection events. In addition, the electrical pulses are on a time scale that is three orders of magnitude larger than the results shown in d). The

slow ringing effects, that also occur in other larger detectors, as shown in [24], result from reflections at the readout electronics due to impedance mismatches. Therefore, we will limit ourselves to detectors with a square size ranging from $2000 - 7500$ squares for further testing.

Nevertheless, we were able to collect some data on the bias-dependend count rate of the smallest detector. The data is shown in fig. 5.9 a). In the bias-current window from $17.4 - 18.3$ µm the detector is sensitive to single photons and the count rate increases exponentially with the bias current. When turning of the light source we can measure the dark count rate of the detector. From the displayed data it is evident, that the counts are mainly dominated from the dark counts and that we are far from reaching a saturated internal detection efficiency.

The high dark count rate can be caused by shielding problems in the cryostat, fluctuations in the electrical signal or by imperfections in the patterned structures. In our case, we assume that the high dark count rate is mainly limited by fabrication imperfections. In [160] it was shown that bends an sharp corners can limit the performance of superconducting detectors due to current crowding effects. Therefore, an optimal design for restricting detector geometries has to be considered. To reduce current crowding effects in the bends, a second approach is to thicken them by an additional superconducting layer on top of the normal film [161]. This approach has not been considered in this work.

The two preliminary experiments already show that it can be a challenge to find the right detector parameters to achieve saturated internal detection efficiency. From the results obtained so far, I want to briefly conclude what needs to be considered in regards to the detector design.

1. For the detector to not latch and no ringing effects in the electrical response function we need to design the detector in the window of $2000 - 7500$ squares.
2. The film thickness can highly influence the wire width for which a saturated internal detection efficiency can be achieved. Therefore, we need to check a broad window of different wire width [155].
3. In order to reduce current crowding effects in the bends, we need to use an optimized design for the bends in the meander detector. For this we will use the *PHIDL GDS*-layout code [162] that includes an optimal design for 180° bends and taper designs for transitions between structures of different widths. Current crowding in curves or sharp corners can otherwise lead to increased dark count or detector latching.
4. The active area of the detector can influence the performance of the detector as well. A large active area will increase the optical coupling efficiency, but it will also increase the probability of imperfections along the nanowire. Therefore, we need to carefully choose the active area of the detector [144].

Based on the previous results, we patterned detectors based on all three geometries shown in fig. 5.8. We fabricated straight lines with a length ranging from $0.1 - 6$ mm and width variations ranging from $0.4 - 1.4$ µm in 100 nm steps. For the detector geometries that do

not exceed 4000 squares, we include an additional 10 µm wide 5000 square serial inductor. By introducing the serial inductor we can reduce the active area of the detector, while keeping a sufficient kinetic inductance. Therefore, we reduce the probability of fabrication imperfections in the nanowire of the detector. Instead the serial inductor will take up a 1.2×1.2 mm^2 space. Small constrictions in the inductor will most likely not influence the performance of the detector, since it is much wider than the nanowire and does not lead to detection events. An SEM image of a 920 nm wide 200 µm long detector with a serial inductor is shown in fig. 5.10 a). In fig. 5.10 c) and d) two close up SEM images of detectors are shown. In case of c) a set wire width of 400 nm was given. Since we are operating at the resolution limit of the system, the wire shown exhibits an increased sidewall roughness as seen in the image. In comparison, a wire with a set width of 700 nm is shown in d). The reduced sidewall roughness can be clearly identified.

In addition, we patterned a meander detector with 4000 squares, a wire width of 1 µm and an unfolded length of 4 mm (see. fig. 5.10 b)). In comparison to the line detectors and the detectors with the serial inductor, the design of the meander exceed the write-field dimensions of the WM II. Therefore, we have to check whether the meander is subject to stitching errors or whether the pattering process provides sufficient resolution. The inductor is of course also subject to stitching, but the same arguments apply here as for the discussed fabrication imperfections in the inductor.

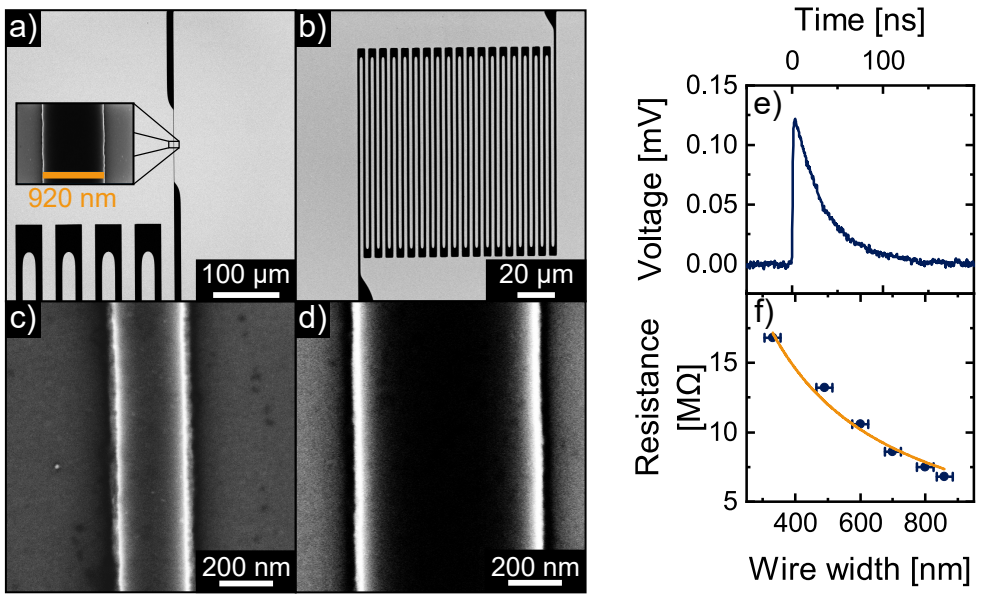

Figure 5.10: SEM images of a) a 920 nm wide 200 µm long detector wire with a serial inductor. e) shows the electric response function of this detector. A picture of a meander detector is given in b). For a set wire width of c) 400 nm an increased sidewall roughness is visible. Increasing the width to d) 700 nm results in a smaller sidewall roughness. f) shows the measured room temperature resistance of 6 mm long wires in dependence of the wire width.

All detectors were patterned in a single exposure step, including the detectors themselves, the inductors and the required bond pads. This clearly demonstrates the potential of fabricating micron-wide SNSPDs with direct laser lithography. It simplifies and accelerates the fabrication process and enables the patterning of large active-area detector systems.

In a first test we measured the room temperature resistance of the 6 mm long wires. The results obtained for the different wire widths ranging from $0.4 - 0.9$ µm are plotted in fig. 5.10 f). The inversely proportional relation between the wire width and the resistance is illustrated by the fit. At cryogenic temperatures the line detectors were sensitive to impinging photons down to a wire width of 0.5 µm. The measurement of the bias-dependent count rate for the long-wire detectors did not reveal a saturated internal detection efficiency. This is probably due to constriction in the long nanowire. Nevertheless, we were able to show functional detectors with a wire length up to 6 mm.

Therefore, in order to saturate the internal detection efficiency, the shorter line detectors with lengths of $100 - 400$ µm and an serial inductor are investigated in the following. The photoresponse pulse of a 0.92 µm wide and 200 µm long detector is shown in fig. 5.10 e). This first shows that the addition of an inductor has not degraded the performance of the detector. For said detector the normalized bias dependent count rate and the dark count rate are plotted in fig. 5.11 b). For the bias current range of $20 - 24$ µA the count rate saturates, leading to a saturated internal detection efficiency. Since reaching a plateau is mainly limited by the fabrication imperfections, the measured plateau indicates sufficient fabrication tolerances using direct laser lithography for device patterning. The statistical errors for the count rate are Poisson noise, which are too small in comparison to the data points to be visible. As already mentioned a saturated internal efficiency is essential for achieving high system efficiencies. In the scope of this work we have not taken any steps towards optimizing the collection and absorption efficiency to achieve a high SDE.

For the measurement of the bias-dependent count rate the detector response was measured in coincidence with the pulsed laser. In the active measurement time of 1 ms the number of dark counts was negligible. Therefore, we do not need to include a dark-count correction to the displayed data. The plotted dark count rate in fig. 5.11 b) was taken independently. Because the same coincidence window was used for all subsequent measurements, the dark counts will not be included in the following data.

Furthermore, we tested the performance of similar devices with wire width ranging from $0.59 - 1.43$µm. The width of the wires were measured with the help of an SEM. Measuring the width along the wire yields the error of the wire width shown in fig. 5.10 f) and 5.11 c). Since the absolute count rate of each detector varies due to different collection efficiencies under flood illumination the count rates are normalized. All tested devices show a saturated internal detection efficiency with an optimal operation window for wire width of (0.9 ± 0.2) µm.

In addition, we investigates the timing properties of the 0.92 µm wide and 200 µm long detector, which bias curve is depicted in fig. 5.11 b). The timing jitter is defined as the uncertainty in the arrival time of the detected photon. This is illustrated in the inset of

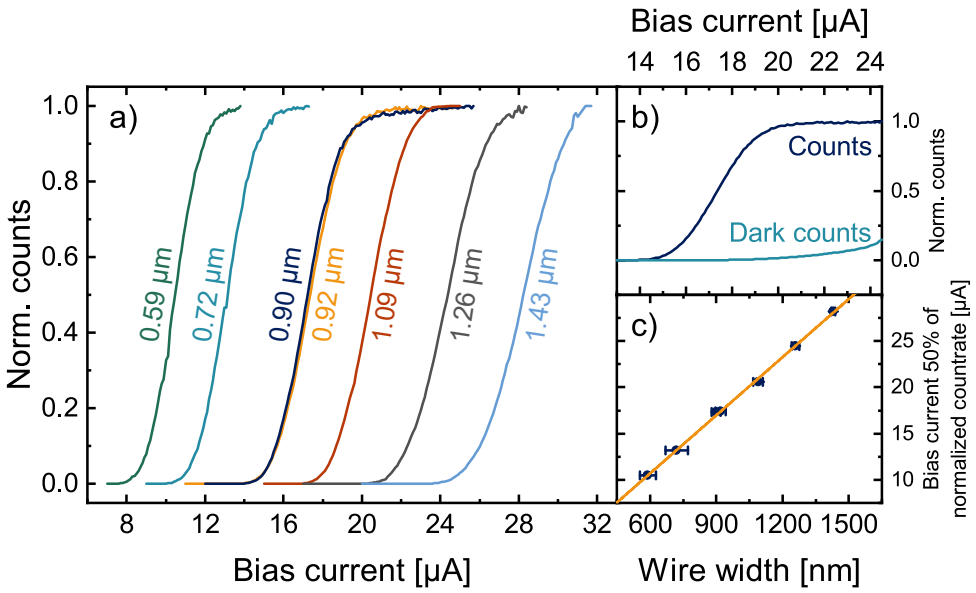

Figure 5.11: a) Bias-dependent count rate of detection events in line detectors with different widths. The count rates were measured in coincidence with the arrival time of the laser pulse and normalized to their maximum count rate. The graph for a width of 920 nm corresponds to the measurement data in b). In b) the dark counts are included. c) Bias current at 50 % of the maximum count rate based on the data from a). The error given for the width are based on SEM width measurements. The error on the bias-current is derived from the count rate limited by Poisson noise, which is negligible.

fig. 5.12 b). A detection event leads to a trace as presented previously. When we sum up multiple traces for multiple detection events, a collective trace with a finite width as shown in the insert of b) is obtained. The highlighted width in the illustration relates to the timing jitter t_j and the timing resolution of the detector. It can be measured by recording a histogram of the delay times between a picosecond laser pulse and an SNSPD pulse. Although SNSPDs based on NbN have shown a timing jitter down to 3 ps [27], typical detectors based on tungsten silicide exhibit a total jitter of ≈ 150 ps [163].

For the characterized detector we obtained a timing jitter of (227 ± 1) ps. The results shown in fig. 5.12 b), were obtained using a pulsed laser at 1550 nm with a pulse width of 9 ps. The peak can be fitted with a Gaussian peak and the FWHM from the fit gives the timing jitter of the detector. The given error arises from the fit.

The measured jitter is influenced by amplifier noise, the wiring, geometric jitter and intrinsic jitter. The intrinsic jitter arises from statistical variations in the time it takes to transition the wire into the normal state and depends on the material properties of the superconductor. It is further degraded by the kinetic inductance of the detector, which influences the rise time of the SNSPD pulse. For large detectors with long wires slow rise times are obtained. The intrinsic jitter has typically the smallest contribution to the total

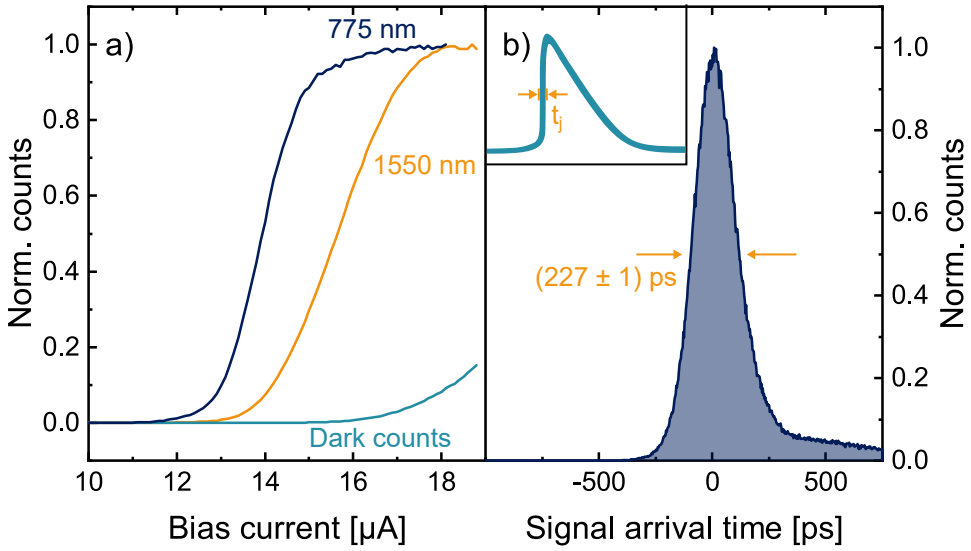

Figure 5.12: a) Bias-dependent count rate of a meander detector with a wire width of 1 µm and 4000 squares. The meander has an unfolded length of 4 mm. b) Timing jitter t_j of the 0.92 µm wide line detector, shown in fig. 5.11 b). The inset shows a schematic of an electrical response function. The timing jitter arises from the noise of the rise time.

measured jitter [19].

Geometric jitter arises from the geometry of the detector. Upon the absorption of a single photon the signal has a finite propagation time from the hot spot to the amplifier. Depending on where the photon is absorbed along the wire, the propagation time varies. The geometric jitter scales with the length of the nanowire. In this case the wire is considered short with a length of 200 µm, resulting in a relatively small contribution to the jitter. Nevertheless we additionally measured the jitter of a meander detector with unfolded length of 4 mm, for which we obtained a jitter of (360 ± 2) ps. The increase in the jitter could result from the increased size of the detector.

The biggest contribution to the jitter arises from the read out circuitry. The contributions from the 5 mm long wires bonds, the amplifier noise, the laser synchronization and the time tagger were not deconvoluted from the data. In this sense, the presented results can be considered as an upper bound for the timing jitter. A careful investigation of the individual factors would be necessary to quantify their contributions.

Since imperfections in the fabrication steps are especially critical for large active-area devices, we investigated the detector performance of a 1 µm wide and 4 mm long detector, which is folded into a meander shape. The bias-dependent count rate was measured for the two wavelength of 1550 nm and 775 nm. The results are shown in fig. 5.12 a). The device shows a plateau region for both wavelengths. Due to the higher photon energy at 775 nm the count rate increases already at smaller bias currents resulting in the longer plateau

region. In comparison to the short line detectors, the range of bias currents at which the count rate saturates is smaller for the meander design. This can most likely be attributed to limitations in the fabrication. Nevertheless, the results show that saturated internal detection efficiency can be achieved even with the stitching caused by the write-field size of the lithography. With this we can conclude that laser-lithographically written SNSPDs can be realized, enabling easy and fast prototyping as well as structuring of large active-area SNSPD arrays.

To the best of my knowledge, this is the first demonstration of SNSPDs with a maskless optical lithography. In recent years the fabrication of micron-wide SNSPDs have gained more interest [95, 153, 154, 157–159, 164]. With increasing the wire width a steady increase in the active-area of SNSPDs is observable [91, 159, 165, 166], which paves the way for new applications in the field of dark matter search. In the work, presented by Luskin et al. [159], they were able to show a saturated internal detection efficiency for a 1 mm^2 8-pixel area detector based on micron-wide SNSPDs. For the best performing devices the array was still fabricated with electron-beam lithography, which indicates that for the future research the interplay of pattering limitations and superconducting film properties have to carefully investigated and adjusted to the specific applications. So far, it has not really been investigated whether the performance of superconducting detectors in terms of their SDE, temporal properties, or dark count rates can exceed the demonstrated standard when moving to wider wires. Exploring the potential of micron-wide SNSPDs could be an interesting topic for the future.

Now that it has been successfully demonstrated that micron-wide SNSPDs can be fabricated using optical lithography, the task is to integrate them onto our waveguide system. Since Ti:LN waveguides have a weak confinement, micron-wide detectors can increase the efficiency of integrated SNSPDs. The work done in this direction will be presented in the following.

5.4 Micron-wide SNSPDs on z-cut Lithium Niobate

In previous work it was already shown that SNSPDs with their typical wire width of 160 nm can be realized on Ti:LN waveguides [94]. The low confinement of the waveguides and the resulting small overlap with the detector lead to the small system detection efficiencies of 0.7 % and 0.1 % for the two polarization modes. Increasing the wire width increases the absorption of light in the wire resulting in higher system detection efficiencies. Previously we have seen that micron-wide SNSPDs can be fabricated with optical lithography on silicon. We now also want to extend this to lithium niobate as a platform.

We will see in the scope of this work, that differentiating between z- and x-cut lithium niobate will highly influence the realization of superconducting detectors on lithium niobate. For the utilization of quasi-phase-matching by introducing period poling we rely on z-cut lithium niobate. Therefore, the work on z-cut lithium niobate is the focus of the presented work.

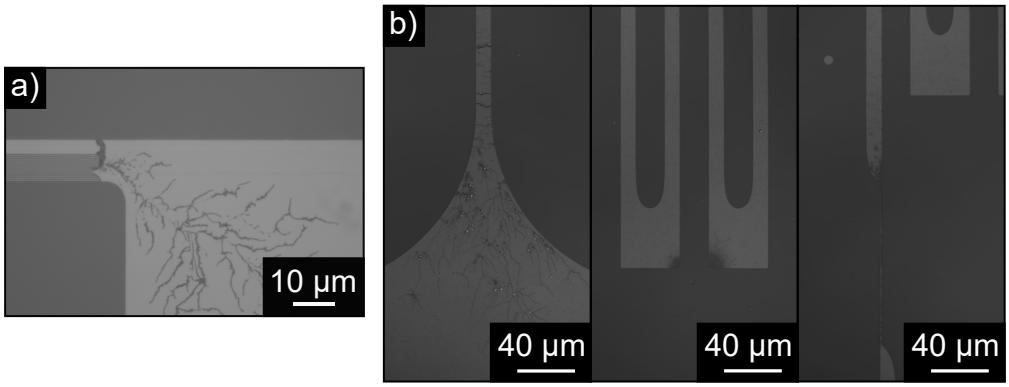

Figure 5.13: Pyroelectric damages to a) normal SNSPDs and b) micron-wide SNSPDs on lithium niobate. The picture for the normal SNSPD was taken from [94].

Already in [94] it was evident, that the pyroelectric properties of lithium niobate are most likely to harm the detector during the cool down. A picture of such a damage is visible in fig. 5.13 a). During the cool down from room temperature to < 0.8 K charges can accumulate on the $+c$ and $-c$ side of the sample surface. The surface of lithium niobate is not conducting. Therefore, areas with a dense carrier concentration can build up locally on the sample surface. If these charges build up underneath a detector it can result in a potential difference between the two ends of the detector. The nanowire itself is highly resistive above the critical temperature and has a high kinetic inductance L. According to $U_{\text{ind}} = -L\mathrm{d}I/\mathrm{d}t$, the rapid build up of pyroelectric charges therefore induces a potential difference in the detector. The resulting current over the wire is associated with the arc-like damages of the detector as shown in fig. 5.13 a). In previously conducted experiments, it was shown that the majority of pyroelectric events occur above 150 K. The following experiments were conducted together with Felix Dreher.

In a first test we wanted to see if the transition to micron-wide nanowires is sufficient to overcome the pyroelectric damages, due to the reduced resistance of wider wires (see fig. 5.10). For this, detectors were patterned on z-cut lithium niobate and cooled down to cryogenic temperatures. After the warm up, we investigate the detectors under a laser microscope to see potential pyroelectric damages. Example picture are shown in 5.13 b). The pictures include typical damages that occur when the superconducting wire is transitioning to smaller width, at sharp corners of the inductor or the wire itself. When comparing wires of different widths, it can be seen that wider wires are less easily damaged than narrow wires. However, the effect is not strong enough to overcome pyroelectric damage, so other ideas need to be explored.

In a first approach, we want to investigate if changing the detector geometry can reduce the damaging of the detectors. Therefore, we implemented a ground plane surrounding the detector. The ground plane is supposed to compensate the pyroelectric charges in the surrounding area of the detector. By connecting the ground plane to the ground potential we want to flush away the accumulated charges. Additionally, we rounded the corners

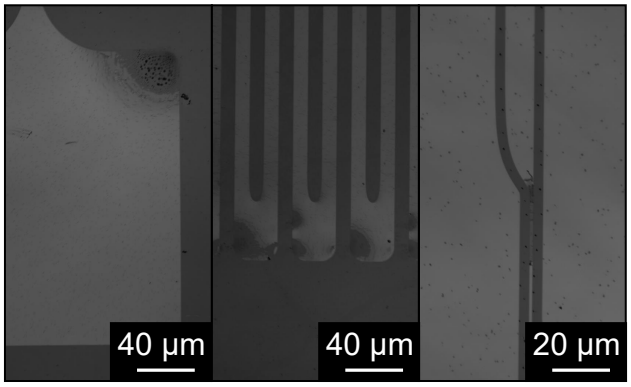

Figure 5.14: Laser microscope image of a bond pad, a nanowire and the inductor. Changing the geometry of the detector by rounding the corners or introducing a protection ring does not significantly reduce the pyroelectric damage.

of the bond pads and the serial inductor since arcing seemed to be more likely at sharp corners.

After a temperature cycle in the cryostat the structures are investigated with a laser microscope. Images of the typical damages are shown in fig. 5.14. Neither rounding the corners nor adding the ground plane helped to reduce the pyroelectric damage to the detector. The observations indicate that the detectors are exposed to an inner current running through the detector. It is assumed that the driving force behind the current is a potential difference between parts of the detector. The potential difference arises from a difference in the locally accumulated surface charges. It is assumed that the high current density exceeds a critical damage threshold of the tungsten silicide when the superconducting strip is narrowed. Thus, the ground plane does not help to prevent the narrow wire from a critical damage. The bond pads and inductor are assumed to be subjected to high electric fields that cause flashovers and damage to the detector.

We conclude that by just changing the geometry/design of the detector we cannot prevent the detector from a critical damage. The charges that build up during cooling must therefore be compensated by an additional structure that has a lower resistance than the detector. The current will then run through the additional structure and not the detector.

5.4.1 Coating with Carbon to Overcome Pyroelectric Damage

For the additional structure, we are now considering conducting materials that can be deposited onto lithium niobate. The conducting layer is supposed to flush the pyroelectric charges away so that they do not harm the detector. If a conducting layer based on a metal like gold would be used an additional insulating layer between the detector and the metal would be required. In addition, a metal layer deposited on top of a waveguide would drastically increase optical propagation losses. To keep the system as simple as possible we

would require a conducting material that stays conducting during the cool down until the critical temperature of a-WSi (≈ 3 K) is reached and then loses its conductivity. The material should also not drastically increase the propagation losses of optical waveguides.

First, we investigated the properties of a thin carbon layer for this purpose. The carbon layer is normally used in SEM imaging as a thin conducting layer for insulating substrates. The carbon layer can be easily deposited with a carbon coater on lithium niobate. At room temperature, we measured a lower resistance for a thin carbon film than for the detectors. When cooling down we could observe that the carbon losses its conductivity at cryogenic temperatures. This allows us to deposit the carbon directly on the detectors with a commercial carbon coater. The carbon can be later removed with oxygen plasma.

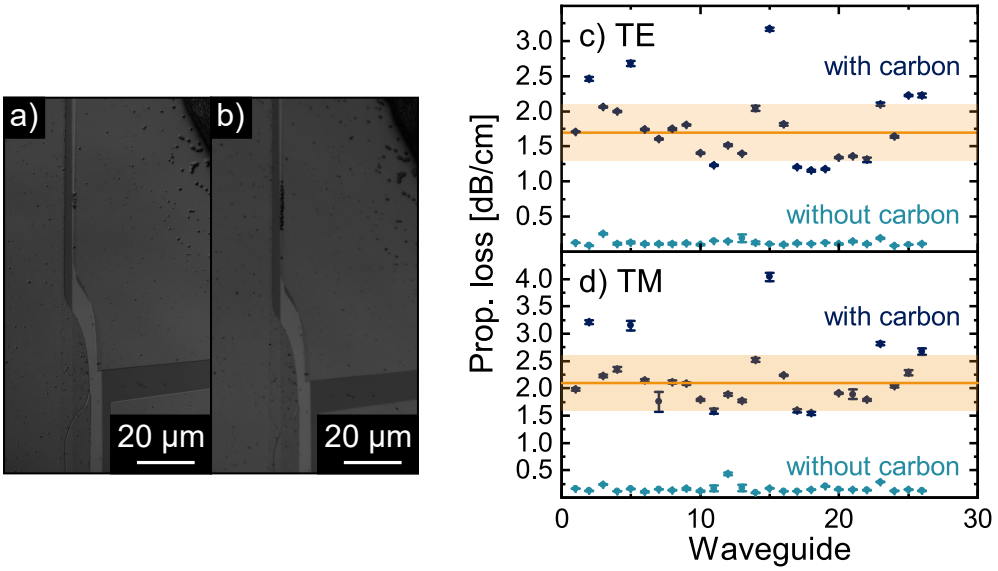

Figure 5.15: A part of the line detector after a) a first cool down and b) a second cool down. 25 pulses of carbon were deposited on the sample. The optical losses for c) TE and d) TM polarization before and after the deposition of the carbon. The losses drastically increase to a mean value of c) (1.7 ± 0.4) dB/cm and d) (2.1 ± 0.5) dB/cm.

To test the usefulness of carbon, four different samples were fabricated. They were coated with 15, 20, 25 and 30 pulses of carbon. The number of pulses correlate with the amount of carbon deposited on the sample. The used carbon coater is normally not suited for an accurate control over the amount of carbon deposited on the sample surface. Therefor, the actual film thickness is not determined and a rather qualitative investigation of the influence of the number of pulses is carried out. While for the 15 pulses the detectors were still damaged after a first cool down. The total amount of 127 detectors on the other three samples remained intact. A picture of a detector covered by 25 pulses of carbon after the first cool down can be seen in fig. 5.15 a). Since the majority of the pyroelectric effects occur above 150 K, a cryostat with a base temperature of 4 K was used. At this temperature,

the detectors are not yet superconducting, but if they were subject to pyroelectric damage, it would already be visible. The carbon layer has cracked, indicating different thermal expansion coefficients for the carbon layer and the substrate. Nevertheless, the underlying detector stayed intact.

In order to check the reproducibility of the samples, the sample with 20 pulses was cleaned and coated for a second time with 20 pulses of carbon. To see if the cracked film has an influence on the probability of detector destruction, the sample with the 25 pulses was cooled down for a second time, together with the freshly coated sample. After the second temperature cycle, no difference between the first and second cool down is visible. A picture of the same detector after the second temperature cycle is given in fig. 5.15 b).

The results of the sample with 20 pulses indicate that the carbon coating of the sample is inhomogeneous. During cooling, 7 out of 39 detectors were damaged, which is still a great improvement over the no carbon scenario. Since the damaged detectors were placed more towards one side of the sample, it is assumed that sample is not coated with a homogeneous thickness.

Since the application of carbon to the lithium niobate surface appears to overcome pyroelectric damage, the associated propagation losses are investigated. 25 pulses of carbon were deposited on a Ti:LN waveguide sample and the propagation losses where characterized as described in [81]. The measured additional propagation losses for multiple waveguides are shown in fig. 5.15 c) and d). The errors given for each individual measurement are determined from averaging over multiple Fabry-Pérot resonances. The mean propagation loss at 1550 nm is increased to (1.7 ± 0.4) dB/cm for TE and (2.1 ± 0.5) dB/cm for TM. The error is calculated from the standard deviation and is included by the highlighted area in fig. 5.15 c) and d). The high propagation losses do not make carbon an ideal candidate for future application of SNSPDs on lithium niobate. In quantum applications, it is important to minimize the loss introduced into the quantum state. To minimize the added propagation losses, we could deposit the carbon only on the required area of the SNSPDs in the future.

Because the carbon seems to solve the issue of pyroelectric damages, detectors are now patterned on Ti:LN waveguides and coated with 25 pulses of carbon. The detectors are bonded and cooled down to cryogenic temperatures. After the base temperature is reached, it is checked if the bonded detectors are in the superconducting state. Measurement of the resistance showed that all detectors were open, indicating that the carbon could not compensate for the pyroelectric effects that occur with bonded detectors. The investigation of the bonded detector under a laser microscope showed that all bonded detector were subject to damage. As it is visible from fig. 5.16 a) and b), arcing from bonded detectors to unconnected detectors leads to a destruction of the unconnected detector.

It is assumed that the bond wires act as a charge reservoir due to the free carriers in the wire. As a result, many more charges are available to compensate for the surface charge densities generated in the surrounding area. The additional charges and the arising potential difference on the surface can no longer be compensated by the carbon, causing the detector to break. As a simple solution we tried shorting the bonded detectors outside and

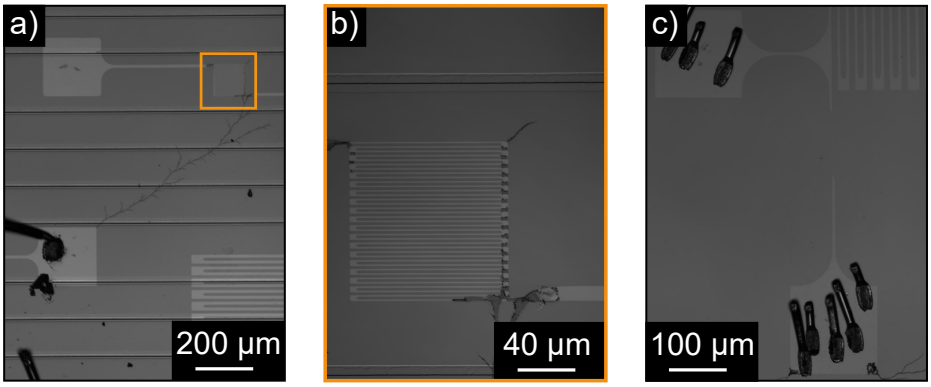

Figure 5.16: Bonding a detector results in a destruction of the detector even if it is coated with carbon. Arcs coming from a bonded detector can damage neighboring detectors as shown in a) and b). Shortening the detector inside the cyrostat as shown in c) reduces the pyroelectric damage.

inside the cryostat. It is assumed that due to the shorting the current avoids to flow through the nanowire, and is redirected through the short. When cooling down we observed that shorting the detector outside the cryostat did not reduce the pyroelectric damage. The dynamics of the pyroelectric charges building up is too fast for the long wires required to connect the detector outside the cryostat. Therefore, the currents keeps flowing through the detector and damages it.

As a last test, shorting the detector inside the cryostat was investigated. In fig. 5.16 c) a detector where both bond pads were connected to each other is shown. Here the bond wire is assumed to be short enough to compensate for the pyroelectric induced current. However, this is not a suitable solution, since for the proper functioning of the detector the shortening wire needs to be cut at the operation temperature to have signal and ground on the two bond pads. Moreover, in fig. 5.16 c) it is visible that still arcing from the bond pad away to other detector can occur.

In conclusion it can be stated that carbon is not a feasible solution to overcome the pyroelectric effects taking place in lithium niobate. It was shown that the micron-wide wires tend to be less damaged than nanowires. Changing the design of the detector did not reduce the damage significantly. Coating the sample with carbon clearly reduced the pyroelectric damage. The amount of carbon is decisive. Bonding the detectors has an significant influence on the damages, which can not be compensated by the carbon. Thus, a different solution has to be considered.

5.4.2 Characterizing Indium Tin Oxide as a Conductive Layer

It was already mentioned that conducting layers that stay conducting underneath the detector may reduce the pyroelectric damage. Normal metal conductors like gold or silver

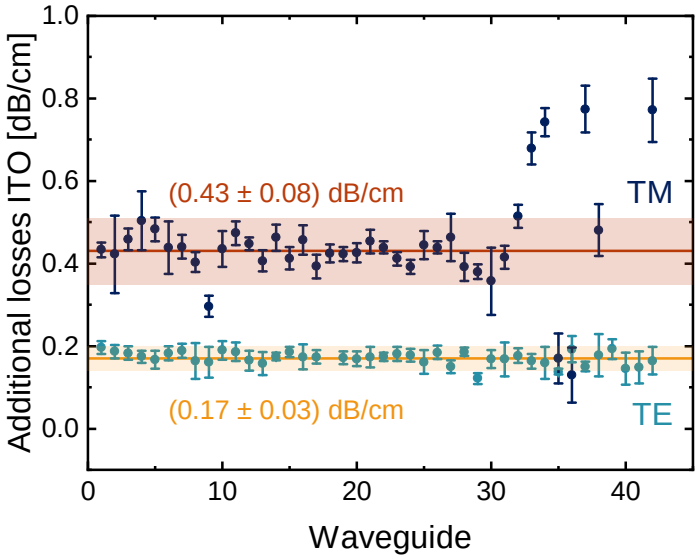

Figure 5.17: Additional introduced propagation losses from depositing (56 ± 3) nm of ITO on Ti:LN waveguides. For TM we measure an additional loss of (0.43 ± 0.08) dB/cm. TE is subject to a smaller increase in propagation losses, with (0.17 ± 0.03) dB/cm.

have the issue of drastically increasing the propagation losses when deposited on optical waveguides. A promising candidate for a conducting but transparent medium is indium tin oxide (ITO).

To test the conduction and absorption properties, (56 ± 3) nm of ITO are deposited on-top of a Ti:LN waveguide sample with an electron-beam evaporator. At the power of 2.7 % a growth rate of 2 Å/s was measured. The layer thickness was checked with ellipsometry measurements with the help of Max Albert. To turn the ITO layer transparent it is oxidized in a oven under oxygen atmosphere at 350 °C. The heat up is done on a 4 h timescale to avoid pyroelectric damaging of the LN sample. The temperature is kept constant for 4 h and is cooled down to room temperature in another 4 h.

The resistivity is measured by contacting the sample surface with probing needles and measuring the resistance with a multimeter. On two different samples a resistivity of (310 ± 30) Ω/cm and (370 ± 30) Ω/cm is measured. The error results from the uncertainty in measuring the separation between the contact needles. During a cool down to the operation temperatures of the SNSPDs the ITO layer stays conducting with a slight increase in resistivity. Potentially the ITO layer will be able to compensate the pyroelectric charges occurring in lithium niobate.

As a last test, the additional losses introduced by the ITO layer are measured. The results are shown in fig. 5.17. For both polarizations we measure a slight increase of the propagation losses. TE experiences a mean increase of (0.17 ± 0.03) dB/cm. The error is given by

averaging over different waveguide groups. Due to the close proximity of TM to the surface, an average increase of (0.43 ± 0.08) dB/cm is obtained for the orthogonal polarization. It has to be further investigated why the propagation losses increase for TM polarization and larger waveguide numbers.

The additional loss introduced by the ITO is much smaller than for the carbon. With the additional conductivity it is a promising candidate for overcoming the pyroelectric damage. For the following realization of SNSPDs, an insulation layer of silicon dioxide needs to be deposited on the ITO layer. Afterwards the superconducting film has to be deposited and patterned. Since parameters like the surface roughness of the ITO layer have not been considered yet, it might be beneficial to first test the presented idea with normal SNSPDs which require a thicker a-WSi film (≈ 4.5 nm). Therefore, a patterning process of SNSPDs with an e-beam lithography has to be developed. This will be a prospect for future work.

Chapter Summary: The goal of this thesis was to combine the technology from all three sections in fig. 3.3 to perform an integrated homodyne experiment and explore the capabilities of SNSPDs in the scope of strong-field homodyne. Previously in chap. 4 I have presented the work done on integrating the necessary waveguide components in Ti:LN.

This chapter focused on the realization of superconducting nanowire single-photon detectors on Ti:LN waveguides and increase their performance in regards of their on-chip system detection efficiency which is required for a fully integrated homodyne detection experiment. In a first series of experiments, the idea of manipulating the waveguide mode was pursued. A thin silicon taper was patterned on-top of the waveguide. Due to the high refractive index of silicon the mode could be reduced to 31 % and 35 % in the y- and z-direction of its initial mode size without a clear evidence to drastically increase propagation losses. The reproducibility of the results turned out to be challenging, since the system is highly sensitive to variations in the silicon thickness due to the high refractive index. A promising alternative could be the utilization of silicon-rich silicon nitride. By varying the concentration of silicon in the compound the refractive index could be potentially tuned. The presented work on the tapers can also be expanded to other waveguide platforms to increase on-chip SDE.

A second approach was to increase the width of the detector nanowires to the micrometer range. Reducing the thickness of the superconducting layer to 2.6 nm enables the fabrication of SNSPDs with optical lithography.

Previous experiments have shown that the pyroelectric properties of lithium niobate make it challenging to fabricate SNSPDs with a high yield on LN [94]. Different ways to overcome this issue have been investigated. While changing the design of the detector did not significantly reduce the damage, it was shown that a conducting layer of carbon, normally used in SEM imaging, reduces the damage significantly. The properties of the carbon film in regards to its additional optical loss have been investigated. A significant increase of the losses was measured. Upon bonding the detectors we could investigate that the carbon can not compensate for the additional effects appearing due to the bonding of the detector.

A promising alternative with ITO was suggested and first steps into characterizing thin ITO layers have been presented. The knowledge gained in the context of these experiments has contributed to a deeper understanding of the pyroelectric effects of lithium niobate. These may not only be of use for Ti:LN, but may also be of interest for LNOI.

Nevertheless, we were able to show that micron-wide SNSPDs can be fabricated by direct laser-writing. This first demonstration was done on silicon and shows that the detectors are not fundamentally limited by the fabrication method. We presented saturated internal detection efficiencies for different detector geometries and different wire widths. Since the demonstration of micron-wide SNSPDs, the research field has gained more interested due to the applications in fields like dark matter research, for which detectors with large active areas are required [159].

This first demonstration of SNSPDs with a maskless lithography shows that the fabrication of detectors with active areas up to $0.1 \times 0.1\text{mm}^2$ is possible. In this context, Luskin et al. [159] have already demonstrated a detector array with the size of $1\ \text{mm}^2$ and investigated different film compositions for the usage of micron-wide detectors. Wollman et al. [165] even patterned detectors with a size of $3.1 \times 3.1\ \text{mm}^2$ with optical lithography. Although the performance of this detector has not been described in detail, this represents the largest detector that has been fabricated to date. To fully exploit the potential of these large-area detectors, the film composition and detector geometry must be optimally matched. My work contributes to the fabrication of SNSPDs with a larger active area and show the potential of fabricating them with optical lithography.

Especially for the integration on waveguide systems the transition to wider detectors can be of great benefit. The mode sizes of optical waveguides can differ significantly. In this regard, strip waveguides based on silicon on insulator and Ti:LN are two examples that form two complete opposite systems. This work contributes to show that SNSPDs can be fabricated with detector widths up to 1 µm, which could increase the SDE of waveguide systems with lower confinement. Together with the optimization of the superconducting layer for a given operating window in terms of detector size, it is imaginable that detectors can be tailored to different waveguide platforms to achieve high system detection efficiencies.

With this we have demonstrated that all parts from fig. 3.3, including nonlinear optical processes, electro-optical modulators and single-photon detectors can be realized with single patterning tool. The maskless optical lithography used in this context allows the rapid prototyping of these components.

Using the results from chap. 4 and 5, it is now intended to conduct a homodyne experiment. Since optical losses are of great importance in this context, detectors with a high system efficiency are required. To ensure this, off-chip detectors will be used from now on. For further research, it is therefore not only crucial to increase the yield of the detectors on lithium niobate, but also to significantly improve the system efficiency. Until this is achieved, the use of off-chip detectors in conjunction with homodyne detection is the sensible way forward.

Integrated Homodyne Detection with SNSPDs

6

In the previous chapter I have discussed different integrated components that can be realized in titanium in-diffused lithium niobate. In this chapter, I will combine several individual components on a single chip to perform a partially integrated homodyne experiment with SNSPDs. Before we make the transition to the few-photon environment of experiments with SNSPDs, I want to discuss how homodyne detection works in case of a bright local oscillator and how homodyne detection reveals insights on a quantum state.

6.1 A Brief Introduction to Homodyne Detection

Homodyne detection consists of three different building blocks: the state preparation, the interference and the detection of the signal after interference. The schematic setup of homodyne detection is pictured in fig. 6.1 a). On a balanced beam splitter the signal (e.g. a quantum state) is interfered with a bright local oscillator. The local oscillator originates from a laser source. The signal is an arbitrary state that we want to characterize by its phase-space distribution. The theoretical background will be given in more detail in the following and is mainly taken from [12, 60, 61].

In quantum optics, the Hamiltonian of a single-mode electromagnetic field with unit frequency can be written as the Hamiltonian of a quantum harmonic oscillator

$$\hat{H} = \hat{n} + \frac{1}{2} = \frac{1}{2}(\hat{X}_2^2 + \hat{X}_1^2). \tag{6.1}$$

Here we set Plank's constant $\hbar = 1$. The Hermitian operator $\hat{n} = \hat{a}^\dagger \hat{a}$ is defined as the photon number operator and is given by the annihilation operator $\hat{a}$ and creation operator $\hat{a}^\dagger$. We can calculate the expectation value of $\hat{n}$ for a state $|\Psi\rangle$ by $\langle\Psi|\,\hat{n}\,|\Psi\rangle$, which is abbreviated with $\langle\hat{n}\rangle$. The annihilation and creation operators can be considered as subtracting/adding a photon to the mode. The number operator can be used to determine the optical power in a state since the power is proportional to the number of photons.

The eigenvalues of the quantum harmonic oscillator are given by $E_n = n + 1/2$, with n photons occupying the mode. From the Hamiltonian and the eigenvalues we can conclude that there exists a vacuum mode with finite energy that is occupied with no photons (i.e. $n = 0$). This state is defined as the vacuum state $|0\rangle$.

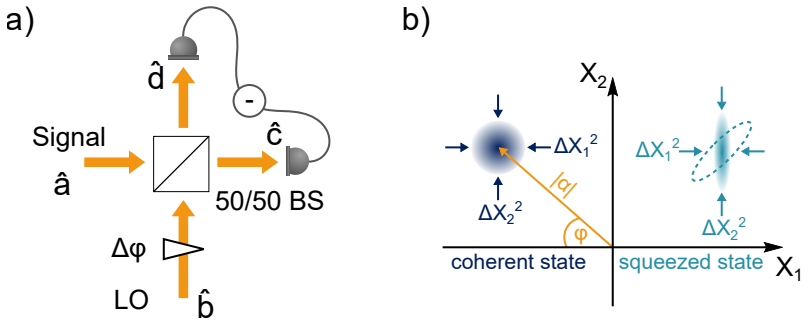

Figure 6.1: In a) a schematic of the homodyne detection scheme is pictured. b) Illustration of phase space of the two quadratures X_1 and X_2. Depicted is a coherent state (dark blue), where the noise is equal for both quadratures. In contrary, for the squeezed state (light blue), the noise for X_1 is pushed below the quantum-noise limit, while for X_2 it is increased in order to not violate the uncertainty principle.

We can also write the Hamiltonian in terms of the two dimensionless quadratures $\hat{X}_1$ and $\hat{X}_2$. The quadratures are observables that can be used to describe a quantum state. Due to the analogy to the harmonic oscillator the two quadratures are often referred to as position and momentum of the electromagnetic oscillator. They do not appear in real space and have nothing to do with the position and momentum of the photon, but define the electromagentic oscillator in its phase-space representation. The phase space spanned by the two quadratures is pictured in fig. 6.1 b). When introducing the electric field operator $\hat{E}_x$ of an electromagnetic wave polarized in the x-direction

$$\hat{E}_x = 2E_0 \sin(kz)\,[\hat{X}_1 \cos\omega t + \hat{X}_2 \sin\omega t], \tag{6.2}$$

we see that the electric field can be expressed in terms of the two quadratures. It is obvious that $\hat{X}_1$ and $\hat{X}_2$ can be treated as field amplitudes oscillating out of phase with each other. The above expression can be simplified by introducing the quadrature component

$$\hat{X}_\varphi = \hat{X}_1 \cos\varphi + \hat{X}_2 \sin\varphi \tag{6.3}$$

with the optical phase φ. Since the two quadrature operators do not commutate they have to obey the Heisenberg uncertainty principle. Therefore, the states take up a certain area in phase space as pictured in fig. 6.1 b) for the two examples of a coherent state and a squeezed state. The quadrature operators can according to

$$\begin{aligned} \hat{X}_1 &= \frac{1}{2}(\hat{a}^\dagger + \hat{a}) \text{ and} \\ \hat{X}_2 &= i\frac{1}{2}(\hat{a}^\dagger - \hat{a}) \end{aligned} \tag{6.4}$$

be written in terms of the annihilation and creation operator. Their mean value gives the position of the state in phase space. The size of the state is related to the uncertainty ΔX_1^2

and ΔX_2^2 of the quadratures. The uncertainty is also often referred to as the variance of the state. In general we can calculate the variance V of any operator $\hat{G}$ with

$$V(\hat{G}) = \Delta G^2 = \langle \hat{G}^2 \rangle - \langle \hat{G} \rangle^2. \tag{6.5}$$

The simplest state to consider is the vacuum state which is located around the origin. For such a state the variance of the two quadratures is given by

$$\Delta X_{1,\text{vac}}^2 = \frac{1}{4} = \Delta X_{2,\text{vac}}^2. \tag{6.6}$$

In literature the uncertainty of the vacuum is often referred to as the minimum uncertainty a state can have.

A second state that is of great importance is the coherent state, depicted in fig. 6.1 b). The coherent state $|\alpha\rangle$ is the quantum mechanical description which is closest to a classical laser source. In phase space, it is pictured as ball whose uncertainty is uniformly distributed. For a coherent state the variance of the quadratures are given by

$$\Delta X_{1,\alpha}^2 = \frac{1}{4} = \Delta X_{2,\alpha}^2 \tag{6.7}$$

which shows that coherent states exhibit the minimum fluctuations of the vacuum. The derivation of eq. 6.6 and 6.7 is shown in the appendix A.5. A coherent state is used in homodyne detection as the local oscillator. If we measure the minimum uncertainty for a coherent state, emitted by a laser, we know that the laser source is quantum-noise limited and is not influenced by other noise sources like intensity noise. The fluctuations in the light field are than governed by Heisenberg's uncertainty principle.

While a coherent state describes rather classical light, squeezed states, as shown in Fig. 6.1 b), are considered highly non-classical light sources. If there is no loss, it is also a state of minimal uncertainty. It differs from a coherent state in the sense that the two quadratures do not have the same uncertainty. While in one quadrature the uncertainty can be below the vacuum limit, the other quadrature shows an increase in uncertainty. The ellipse in fig. 6.1 b) pictures a state that is squeezed in the $\hat{X}_1$ quadrature and is anti-squeezed in the $\hat{X}_2$ quadrature. The orientation of the squeezing can be changed as indicated by the dotted line. The amount of squeezing quantifies by how much the noise in one quadrature is dropped below the noise of the vacuum state. If the squeezed state is influenced by optical loss, which can occur from many different processes such as absorption and scattering, the amount of measurable squeezing is reduced [61].

Due to the presence of the vacuum state, loss can have a large impact on quantum states. Loss in quantum experiments is modeled by mixing the quantum state on a beam splitter with the vacuum state. The process is pictured in fig. 6.2. The transmittivity η of the beam splitter quantifies the loss introduced to the electric field of the input mode $\hat{A}$. Assuming that the input mode is a bright field we can write it in its linearized form $\hat{A} = \alpha + \delta\hat{\alpha}$ where α is the amplitude of the field and $\delta\hat{\alpha}$ the noise on the field. In quantum mechanics,

linearization is done by expanding the operators by their stationary values and then linearizing the expression to the first order fluctuation terms. The first demonstration in the context of quantum optics was done by Yurke [167] to model squeezing in a cavity. The linearization can be used to derive analytical solutions in an experimental setup. The output field after the beam splitter is then written as

$$\hat{A}_{\text{out}} = \sqrt{\eta}\hat{A} + \sqrt{1-\eta}\delta\hat{v} \tag{6.8}$$

where $\delta\hat{v}$ is the noise of the vacuum field. The remaining field, leaving the other arm is considered to be removed from the system and is unmeasurable, thus labeled as loss. From eq. 6.8 it is evident, that loss couples noise from the vacuum field into the input field. In squeezing experiments, the noise on the vacuum field is larger than that of the squeezed input field. Therefore, the squeezing of the input field is lower after the influence of losses. The effect on the measurable squeezing is best visible when calculating the normalized variance of the intensity, $V_{\text{I}}^{\text{norm}}$, measured after the beam splitter. which is given by

$$V_{\text{I}}^{\text{norm}} = \eta V_{A_{\text{in}}} + (1-\eta). \tag{6.9}$$

$V_{A_{\text{in}}}$ is defined as the variance of the input signal. Form eq. 6.9 we see that in the ideal case (i.e. $\eta = 1$) the variance of the input state remains unchanged. The effect of increasing loss $(1-\eta)$ on a squeezed state is illustrated in Fig. 6.2 b) for the three different cases of $-10, -6$, and -3 dB of initial squeezing. The reduction of noise is always given relative to the shot-noise limit measured with vacuum. We see that the amount of measurable squeezing is highly influenced by the amount of loss. Thus, we require minimal optical loss when squeezed states are investigated.

With the help of homodyne detection we are now able to measure the quadratures and the variance of an arbitrary quantum state and thus obtain its phase-space representation. A conventional homodyne setup used for this purpose is shown in fig. 6.1 a). On a balanced beam splitter the two input modes $\hat{a}$ and $\hat{b}$ are interfered. The input modes are the signal state under investigation and a bright local oscillator. In an experimental setting the local oscillator is provided by a laser light source. The two output modes $\hat{c}$ and $\hat{d}$ of the beam splitter are measured with two linear detectors. This is done with photodiodes whose signals are linearly proportional to the photon number of the state. Therefore, the intensities I_c and I_d can be related to the mean photon number $\langle\hat{n}_c\rangle$ and $\langle\hat{n}_d\rangle$ of the beam splitter output modes. $\langle\hat{n}_c\rangle$ and $\langle\hat{n}_d\rangle$ are defined as

$$\begin{aligned} \langle\hat{n}_c\rangle &= \langle\hat{c}^\dagger\hat{c}\rangle \text{ and} \\ \langle\hat{n}_d\rangle &= \langle\hat{d}^\dagger\hat{d}\rangle \end{aligned} \tag{6.10}$$

in terms of the mode operators

$$\begin{aligned} \hat{c} &= 2^{-1/2}(\hat{a} + i\hat{b}) \text{ and} \\ \hat{d} &= 2^{-1/2}(i\hat{a} + \hat{b}). \end{aligned} \tag{6.11}$$

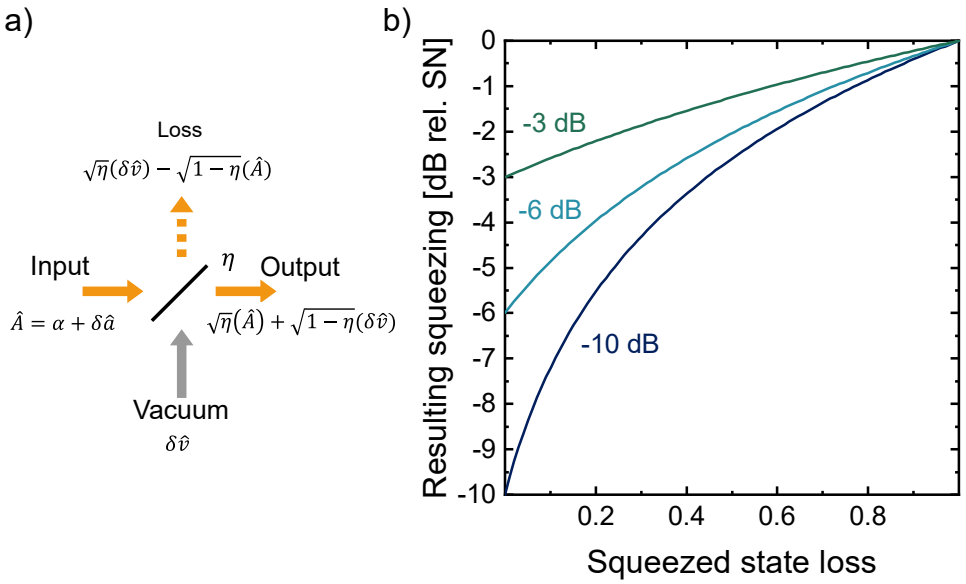

Figure 6.2: a) Graphical representation of loss treatment in quantum optics. The input field $\hat{A}$ is mixed with the vacuum state $\delta\hat{v}$ on a beam splitter. The resulting output mode $\hat{A}_{\text{out}}$ contains noise from the vacuum field. η is defined as the beam splitter transmittance. b) shows the influence of loss on the measurable squeezing if the state has −10, −6 or −3 dB of initial squeezing. The noise reduction is given relative to the shot-noise limit (SN).

$\hat{a}$ and $\hat{b}$ denote the input operator of the signal state and the local oscillator. In homodyne detection we take the difference I_{cd} of the two signals measured by the photodiodes. The difference photon current is given by

$$I_{cd} \propto \langle \hat{n}_{cd} \rangle = \langle \hat{n}_c - \hat{n}_d \rangle = \langle \hat{c}^\dagger \hat{c} - \hat{d}^\dagger \hat{d} \rangle = i \langle \hat{a}^\dagger \hat{b} - \hat{a} \hat{b}^\dagger \rangle. \tag{6.12}$$

Assuming that the input mode $\hat{b}$ is in a coherent state $\left|\beta e^{-i\omega t}\right\rangle$ with the complex amplitude $\beta = |\beta| e^{-i\Psi}$, eq. 6.12 rewrites to

$$\langle \hat{n}_{cd} \rangle = |\beta| [\hat{a} e^{i\omega t} e^{-i\varphi} + \hat{a}^\dagger e^{-i\omega t} e^{i\varphi}] \tag{6.13}$$

with $\varphi = \Psi + \pi/2$. φ expresses the optical phase of the local oscillator in reference to the signal state in input $\hat{a}$. The additional phase shift of $\pi/2$ comes from the reflection on the beam splitter. The expression $e^{i\omega t}$ includes the phase due to the evolving of the state in time. Assuming that mode $\hat{a}$ is at the same frequency ω as the coherent state we can set $\hat{a} = \hat{a}_0 e^{-i\omega t}$. From this we can derive

$$\langle \hat{n}_{cd} \rangle = 2|\beta| \langle \hat{X}_\varphi \rangle. \tag{6.14}$$

with the expression 6.3 for the quadrature operator $\hat{X}_\varphi$. The phase angle φ can be varied

by changing the relative phase of the local oscillator as pictured in fig. 6.1 a). Thus, the quadrature values of the signal can be measured.

Taking a closer look at eq. 6.14, we see that the signal scales with the amplitude of the local oscillator $|\beta|$. Thus, the quadrature of the quantum state scales with the strength of the LO and exceeds the electronic noise of the photodiodes. Additionally, it can be concluded that phase control is required to perform a homodyne experiment. The phase difference between the local oscillator and the signal determine what quadrature angle is measured. If phase fluctuations dominate the detection process no clear investigations of the quadratures can be made.

Homodyne detection is often used to characterize squeezed states and the noise reduction of the squeezed quadrature. The variance is measured by calculating the variance of the difference signal $\langle \hat{n}_{cd} \rangle$. When looking at the expression for the variance of the photon number difference operator

$$\langle \Delta \hat{n}_{cd}^2 \rangle = 4|\beta|^2 \langle \Delta \hat{X}_\varphi^2 \rangle, \tag{6.15}$$

it is clear that the variance of the quadrature can be measured. For a squeezed state we measure a variance $\langle \Delta \hat{X}_\varphi^2 \rangle < 1/4$ at a specific phase angle φ. Thus we have $\langle \Delta \hat{n}_{cd}^2 \rangle < |\beta|^2$. $|\beta|^2$ is defined as the quantum-noise limit of the homodyne detector and is equal to the intensity of the local oscillator. Therefore, if we want to detect squeezing, we expect the measured noise of the difference signal to be below the shot-noise limit.

In order to measure squeezing we therefore need to know the power of the LO. Since the LO is a coherent state subject to Poisson's statistics, the mean photon number $\langle \hat{n} \rangle = |\beta|^2$ is equal to its variance. Therefore, when measuring squeezing, we expect the noise to be reduced below the variance of a quantum-noise limited LO. In this context the quantum-noise limit is also often referred to as the shot-noise limit. We can verify that the detector is shot-noise limited by blocking the signal arm of the beam splitter. In this case, we interfere the local oscillator with the vacuum state, which has a quadrature variance of $\langle \Delta \hat{X}_\varphi^2 \rangle = 1/4$. Thus, if one varies the intensity of the LO, one expects a linear increase in the measured variance, according to equation 6.15.

In order to check the feasibility of SNSPDs for strong-field homodyne detection we need to verify the linearity of the SNSPDs and show with their help that the used light source is shot-noise limited.

6.2 Presenting the Concept Behind the Homodyning Experiment

The experimental setup for the continuous wave (cw) homodyne measurement of a coherent state is depicted in fig. 6.3. The laser source is a tunable fiber-coupled cw laser with spectral width of 400 kHz. The wavelength can be tuned to fit the wavelength dependent behavior

of the integrated components. For the majority of the setup the light propagates through optical fiber to reduce phase fluctuations from environmental influences. The fibers that are colored in blue are polarization-maintaining (PM) fibers, which preserve the input polarization. The yellow fibers are single-mode (SM) fibers in which the polarization can change, due to twisting of the fiber. The signal is split on a 50:50 PM fiber beam splitter (BS). One arm will be the local oscillator, the other can be used for a signal state.

Fiber polarization controllers are used in both arms for polarization control of signal and LO. By changing the polarization of the signal by 90°, signal and LO have orthogonal polarization and can co-propagate through the same waveguide without interfering. It is also assumed that when co-propagating through a waveguide, the phase variations of the signal and LO are the same, so that phase stabilization is required only for the parts where the signal and LO take different paths. In the path of the signal a fixed fiber attenuation of 40 dB can be placed to obtain a weak coherent state as a signal. Without any additional attenuation in the signal arm, the setup is used to measure the visibility of the interference.

In the arm of the LO a variable optical attenuator (VOA) is used to change the power of the local oscillator which is required for showing the shot-noise limit of the homodyne detector. The polarization control in the arm of the LO is used to compensate for the polarization scrambling in the single-mode glass fibers of the VOA. The two arms of signal and LO are combined on a PM fiber polarizing beam splitter (PBS), where signal and LO leave the output port of the PBS in orthogonal polarization.

Both signals are split on a 99:1 fiber BS. The arm containing 99% of the light is used for the phase stabilization with a proportional-integral-derivative (PID) controller. For stabilization, the light is coupled into free space with a collimation package. A half-wave plate (HWP) and a free-space PBS is used to interfere signal and LO. The fluctuation in the interference due to phase noise is measured with a free-space photodiode. A commercial PID controller is used to stabilize the phase in the fiber interferometer with the fiber stretcher in the signal arm. The effect of phase fluctuation and the reduction due to the PID controller is shown in fig. 6.4. In this case we interfered the LO with a weak signal on the homodyne chip and recorded the counts measured in one arm over 20 s. After $\approx$ 10 s we switched in the PID controller.

Without any phase stabilization we see a clear fluctuation in the signal arising from the varying phase difference between the LO arm and the signal arm of the fiber interferometer. When the PID controller is turned on, there is a clear stabilization of the counts. We reduce the standard deviation in the counts to $(20 \pm 1)\%$ of the deviations without any phase stabilization.

The light in the 1% arm of the BS is coupled into free-space with a collimation package, where it is attenuated by additional 60 dB. An aspheric lens with an anti-reflection coating (1050 − 1700 nm), with an effective focal length of 18.4 mm and an NA = 0.15 is used to couple the light into the lithium niobate chip, which is then used for LO and signal

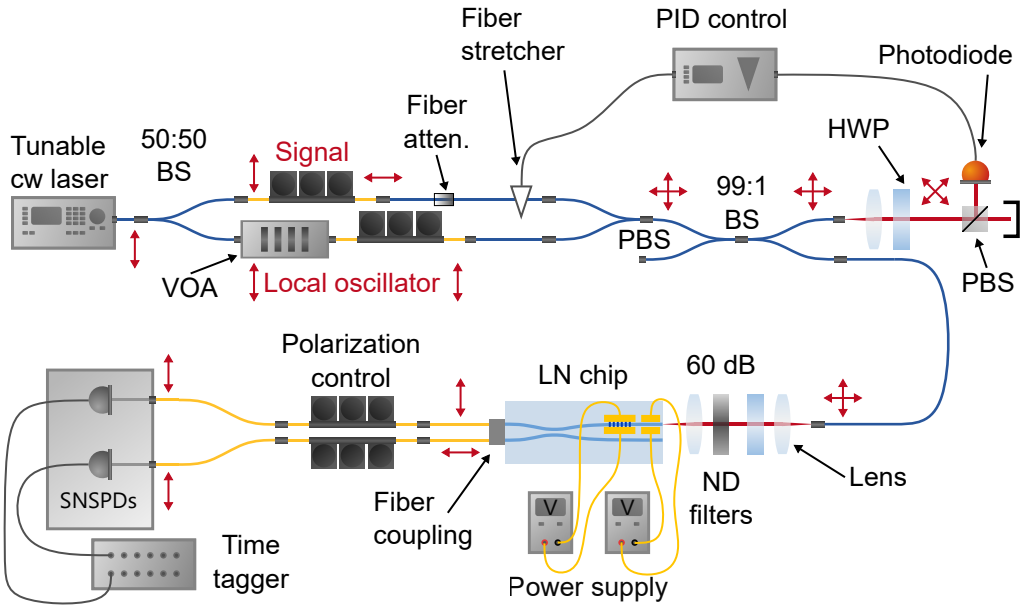

Figure 6.3: Setup used for the continuous wave homodyne detection of a weak coherent state. If the signal arm is blocked we can verify if the laser is shot-noise limited and the SNSPDs can be treated as linear detectors. With the variable optical attenuator (VOA) we can vary the intensity of the LO. A fiber attenuator (Fiber atten.) is used to attenuate the signal that is investigated.

interference. The lens is mounted on a 3-axis stage to optimize the coupling. It matches the lens used in the collimation package.

When coupled to the chip, the signal and LO are still orthogonally polarized, so they do not interfere with each other. When performing homodyne detection we require control over the relative phase difference between LO and signal. Thus, an integrated phase shifter (PS) is required. To interfere signal and LO, a polarization converter (PC) is implemented on the chip in combination with a PBS. The tunability of the PC gives us the flexibility to study the signal and the LO separately or to combine them in a homodyne scenario. When the PC is operated in the correct configuration as a half-wave plate at 22.5° the integrated PBS acts as a balanced BS. A schematic of the chip is shown in fig. 6.3. The exact layout and design parameters are given in the appendix A.4. The PC and PS are wire-bonded, and a power supply can be used to apply a voltage in the range of −60 to 60 V to both structures individually. The performance of the PBS and the PC was previously described in chap. 4.1.4 and 4.3.3. The polarization converter allows the signal and LO to co-propagate in a waveguide with orthogonal polarization, which distinguishes this approach from the classical homodyne setup shown in fig. 6.1 a).

The two output ports of the directional coupler are coupled out with a fiber array. The end of a fiber ferule with multiple fiber cores spaced 127 µm is brought near the end facet of the waveguide chip. Light then couples from the two waveguides into two separate

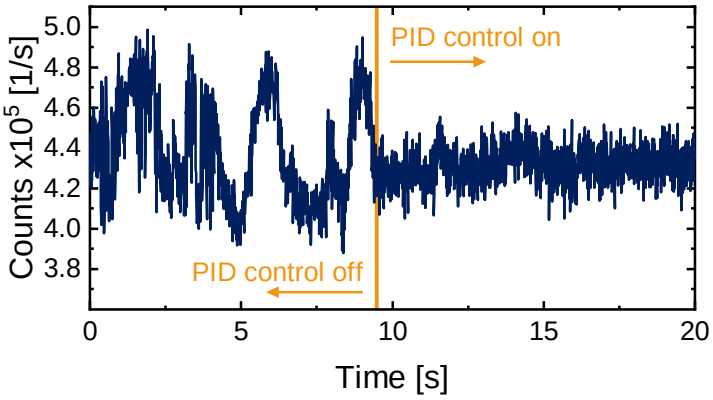

Figure 6.4: Measured counts at one detector over a time scale of 20 s. For the measured signal the LO and signal arm are closed. The fluctuations visible for the first 10 s arises from phase fluctuations between the signal and the LO in the two arms of the fiber interferometer. When the PID control is turned on the phase is stabilized. The standard deviation in the counts is reduced to $(20 \pm 1)\%$ of the deviation without any phase stabilization.

fiber cores. The fiber ferule is mounted on a 6-axis stage with a customized holder so that all degrees of freedom can be used to optimize the coupling of the chip to the fiber. Assuming symmetric in and out-coupling we achieve $(79 \pm 4)\%$ of coupling efficiency for a single side. The multicore fiber is coupled to two commercial SNSPDs with detection efficiencies of $(85 \pm 5)\%$ and $(92 \pm 5)\%$ when uniformly biased at 6 µA. Since the SNSPDs are polarization sensitive, the two fiber polarization controllers in front of the SNSPDs can be used to maximize the signal measured on the SNSPDs. The detection events occurring on the SNSPDs are recorded with a time tagging module. The threshold voltage for a detection event was set to 0.05 V. To eliminate false detection events on the falling edge of the SNSPDs electronic signal, the detector dead time was artificially set to 100 ns. After 100 ns the detector is reset to its initial state. Therefore, it is not reasonable to consider a detector speed of more than 10 MHz. With this setup, we can verify the feasibility of SNSPDs in the context of homodyne detection.

6.3 Experimental Characterization of Homodyne Detection with SNSPDs

The results presented in this section were obtained with the help of Timon Schapeler. For the following experiments only one waveguide group from the previously presented results (see chap. 4.1.4 and chap. 4.3.3) was picked. Since the PC has a limited spectral bandwidth due to periodic poling, all experiments are performed at a single wavelength of 1545.8 nm, which is the center of the phase-matching curve of the bonded polarization

converter. With the spectral bandwidth of 400 kHz the laser light is significantly narrower than the polarization converter.

6.3.1 Interference Visibility

For a first test, we must show that we are able to interfere signal and LO using the polarization converter and the PBS. Since the light coming out of the collimation package is not aligned to the coordinate system of the waveguide, a random linear polarization is coupled out of the collimation package. The HWP in front of the chip can be used to align the linear polarization coming out of the fiber with the coordinate system of the LN chip. For this purpose we just consider the light from the LO. With the HWP we can switch between the two output ports of the PBS. We measure a polarization extinction of $(2.4 \pm 0.5)\%$ and $(0.7 \pm 0.5)\%$ for the two input polarizations TM and TE, which agrees well with the previously measured polarization extinction of 20 dB for the PBS in chap. 4.1.4. The extinction shown in chap. 4.1.4 was measured before the poling process performed for the polarization converter. Due to the periodic poling introduced, even if there is no voltage applied to the electrodes of the PC, some part of the polarization can be converted due to the intrinsic electric fields in lithium niobate, as it is a piezoelectric material. This can lead to a reduced polarization extinction for the integrated PBS.

When both signal and LO are coupled to the chip, the signal is in the TE polarization and the LO is in the TM polarization of the waveguide modes. Since the directional coupler on-chip acts as a PBS, minimal interference should be visible at the two detectors. When sampling the voltage of the PC, portions of the signal and LO convert to the other waveguide polarization. Therefore, interference should increase as the voltage increases. When 50% of both signal and LO are converted, we expect the strongest interference effects. To make the interference visible we need a way to vary the phase difference between signal and LO. For this we use a fiber stretcher, which is connected to a function generator. By applying a sinusoidal voltage with an amplitude of 1 V and a frequency of 2 Hz, we can periodically modulate the phase in the fiber interferometer. The applied voltage leads to an elongation of $\approx$ 6.8 µm which ensures a complete phase shift over more than 2π. While scanning through the phase the measured counts of the SNSPDs are recorded for a measurement time of 10 s.

For the data evaluation the counts are integrated over a time window τ_{int} which sets the bandwidth and the bin size of the detector. For the measurement of the visibility we set the integration window to 10 ms which leads to a detector bandwidth of 100 Hz and 1000 samples over the measurement time of 10 s. To achieve a more pronounced oscillation of the interference, the signal and LO were set to the same power. The resulting count rates in counts/bin are shown for the two different voltage settings of $V_{\text{PC,min}} = 4$ V and $V_{\text{PC,max}} = 17$ V in fig. 6.5 a) and b). In both plots the raw data of the count rates are shown in the background of the solid lines. Since we want to consider the maximum I_{max} and the

minimum I_{min} of the count rate for calculating the visibility $\mathcal{V}$ according to

$$\mathcal{V} = \frac{I_{\text{max}} - I_{\text{min}}}{I_{\text{max}} + I_{\text{min}}}, \tag{6.16}$$

we take the moving average over 11 values. The moving average reduces the noise of the count rate and decreases its influence on the visibility calculation. The smoothed curves are highlighted in orange and red in fig. 6.5 a) and b). The reduced noise is clearly visible. From the smoothed data we calculate the visibility according to eq. 6.16. In fig. 6.5 d) the resulting visibility for each voltage set on the PC is shown. When changing the PC voltage a clear modulation of the visibility can be seen. The errors are calculated by a Monte Carlo routine, where we assume a Poissonian distribution for the raw count rate. The Monte Carlo routine works as follows:

1. The maximum and the minimum of the smoothed count rate is calculated.
2. Since we assume a Poissonian distribution for the count rate (coherent states have Poissonian statistics), we calculate the standard deviation of the maximum and minimum by taking the square root of the values.
3. We calculate a normal distribution for maximum and minimum, where the width is given by the calculated standard deviation.
4. We randomly sample 1×10^7 values of the maximum and minimum.
5. For each sample we calculate the visibility and receive a histogram for the visibility.
6. The error for the visibility is then given by FWHM of the visibility distribution.

From fig. 6.5 d) it is evident that we achieve the maximum visibility of $\mathcal{V}_{\text{max}} = 0.950^{+0.013}_{-0.014}$ at a PC voltage of $V_{\text{max,PC}} = 17$ V. For the further conducted experiments, we set the PC to 17 V to achieve optimal interference conditions. A minimal visibility of $\mathcal{V}_{\text{min}} = 0.066^{+0.042}_{-0.041}$ is measured at $V_{\text{min,PC}} = 4$ V. At higher PC voltages the visibility does not reach the minimum measured at $V_{\text{min,PC}} = 4$ V. The applied electric field does not only address the tensor element r_{42} responsible for the conversion, but also changes the refractive index with the weaker tensor element r_{22}. The resulting refractive index change is different for TE and TM and therefore may shift the phase-matching condition, resulting in a reduced conversion efficiency.

The resulting visibility is most likely limited by the integrated chip and the preparation of signal and LO. The used fiber PBS to combine signal and LO in orthogonal polarization is specified with an polarization extinction of 20 dB. Thus, the LO and signal are not necessarily perfectly orthogonally polarized. For the integrated PBS we measured a polarization extinction of $(2.4 \pm 0.5)\%$ for the TM polarization. This additionally limits the measurable visibility. The slight asymmetry in the visibility can be due to a difference in the performance of the PBS with respect to the polarization.

After we determined the maximum visibility, the PC is operated at 17 V and the signal arm is blocked. Since the detectors have different detection efficiencies and the two arms of the

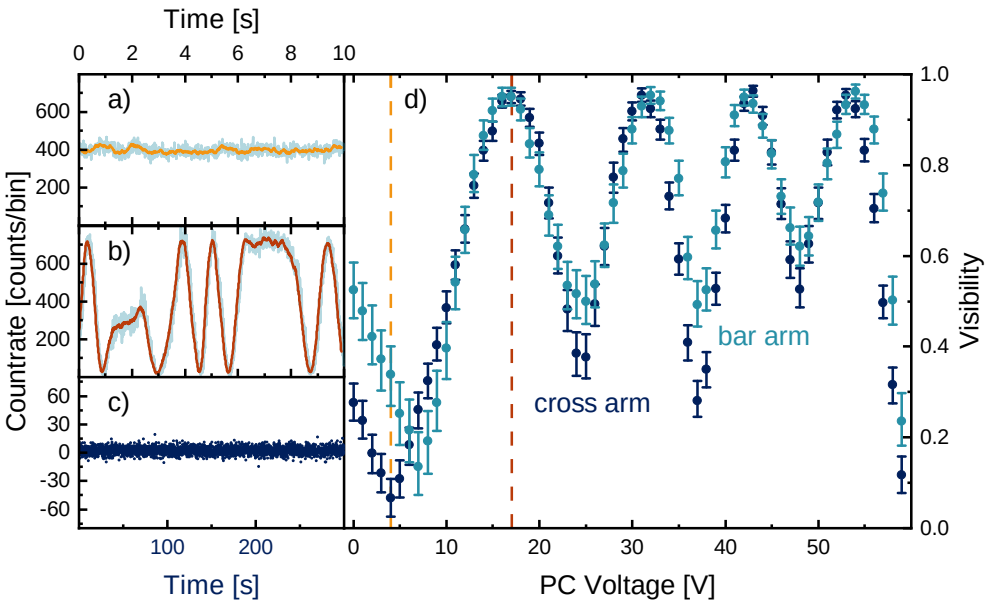

Figure 6.5: a) Fluctuations in the count rate for the minimal visibility at the PC voltage of $V_{PC} = 4$ V. b) shows the count rate for the maximum visibility of interference at $V_{PC} = 17$ V. In each plot the raw data plus the data which was smoothed by a moving average over 11 values is given. From the maximum and the minimum in the count rate the visibility of the interference is calculated. In d) the interference visibility for each PC voltage is given. The uncertainty is determined by a Monte Carlo routine under the assumption of a Poissonian distribution for the raw count rate. c) shows a stability measurement of the difference in the count rate over 5 min.

on-chip PBS have different propagation losses we adjust the efficiency of the detector such that the two count rates are equal. Therefore, we reduce the bias current of one detector to 3.7 µA. We adjusted the threshold level of the time tagger to 0.04 V due to the reduce trace amplitude. Since the detectors are polarization sensitive we can fine tune the efficiency of the SNSPD with the polarization control.

In order to cancel out noise sources in the laser light of the LO, equal count rates for both detectors are required. In this case the subtraction of the count rates cancels out the noise from the LO and only the quantum-noise limit of the signal (i.e. the vacuum state) remains. In classical homodyne detection with photodiodes this can be done by a variable gain design of the detector [168]. In this case each photodiode has a variable gain which can adjust for the difference in the signal strength of the two photodiodes. For the commercial SNSPDs used in this work we have to adjust the efficiency of the brighter detector to level the two count rates. This solution is not ideal since high efficiencies are required, when the detector is used to measure squeezing.

To solve this problem, I propose a superconducting readout circuit that acts as an integrator

for the signal generated by the SNSPDs. In this concept, the signal from the SNSPD generates a current that is stored in a superconducting loop. The amount of current stored in the loop can be adjusted by setting the bias voltage of a superconducting current integrator that controls the amount of current generated by the SNSPD signal. We can inductively couple the combination of SNSPD and current integrator to the superconducting storage loop. When connecting two SNSPDs to the superconducting storage loop, we can design them such that the two currents generated by the SNSPDs offset each other in the storage loop. When the gain introduced by the current integrator is adjusted so that the two currents from two SNSPDs offset each other in the storage loop, this can be treated as the equivalent of two photodiodes with variable gain. For the implementation, we require further superconducting electronics like Josephson junctions and inductors to couple the different superconducting circuits. The proposed circuitry is closely related to the research field of superconducting optoelectronic neurons discussed in the series of papers by Shainline et al [169–173]. Khan et al. [174] have recently demonstrated the combination of SNSPDs with superconducting current integrators. For now, we restrict ourselves to reducing the detector efficiency to level the two count rates of the SNSPDs.

Before we try to show the linearity of the SNSPDs and investigate their shot-noise limit, we want to verify the stability of the difference signal. For this we decrease the bin width to 100 µs resulting in a detector bandwidth of 10 kHz. The count rate is measured over a duration of 5 min. The difference in the count rate is calculated per bin and shown in fig. 6.5 c). For the duration of the 5 minutes no drift in the signal is visible showing a stable operation of the polarization converter.

6.3.2 Linearity and Shot-Noise Limit

In the next step we are interested in characterizing the linearity of the homodyne detector with the off-chip SNSPDs. Therefore, we keep the signal arm open. According to equation 6.15 we then measure the noise of the vacuum, which scales linearly with the intensity $|\alpha_{\mathrm{LO}}|^2$ of the local oscillator. We operate the detector at a bandwidth of 2 MHz since it is well below the maximum bandwidth of 10 MHz set by the dead time of the detector and equal to the homodyne detector presented in [50] which showed the highest reported shot-noise clearance for an integrated homodyne detector. The bandwidth of 2 MHz results in an integration time of 500 ns over which the measured counts are integrated. The integration window defines the temporal mode of our LO which is important for calculating the photon flux of the LO. The photon flux is equal to the intensity of the LO, thus the measured variance of the difference signal should linearly scale with the photon flux of the local oscillator.

Before the chip we measure an optical power of (18 ± 1) µW for the LO. The error arises from the accuracy of the power meter. With the variable optical attenuators we can vary the intensity of the LO. In addition, the setup includes the free-space attenuation of 60 dB. The VOA is scanned from $4 - 80$ dB in steps of 1 dB. The overall attenuation in the setup is chosen so that the SNSPDs latch below the set attenuation of 4 dB, so that the resulting

count rate at 4 dB is the maximum intensity that the detectors can handle. A set attenuation of 4 dB corresponds to a photon flux of $\approx 6 \times 10^6$ photons/s. At the maximum attenuation only the dark counts are measured on the detector ($\approx$ 30 photons/s). From this we can conclude that we can cover the entire operating window of the detectors with the VOA. For the polarization converter we set the voltage to $V_{\mathrm{PC}} = 17$ V to have the maximum visibility.

In the next step we calculate the difference signal of the two count rates. From the difference signal, which is proportional to $\langle \hat{n}_{21} \rangle$, we calculate the variance. Since the measurement time is 5 s we have 10 MSamples (MSa) over which we can calculate the variance. The calculated variance is shown in fig. 6.6. The power of the LO is given in terms of the photon flux with the unit photons/s.

Loss Consideration for the Local Oscillator Power

First, we want to investigate whether the measured variance is shot-noise limited. This means that the actual measured variance is given by the quantum noise of the signal state. On a logarithmic scale the variance of the investigated vacuum state should scale linearly with the slope of 1. If the laser light is shot-noise limited the line should additionally go through the origin. In the inset of fig. 6.6 the calculated variance and the estimated shot noise limit is given. The plotted shot-noise limit is calculated from the LO power before the chip (i.e. (18 ± 0.1) µW) on which we have to add the 60 dB of free-space attenuation.

Plotting the variance of the difference signal versus the estimated shot-noise limit, we see that the actual measured noise is less than the expected noise. This means that the actual LO power is weaker than the measured power before the chip plus the additional attenuation in free space. This is not really surprising since we have not included coupling losses, the on-chip propagation losses and the detection efficiency. We want to see if we can calculate the addition loss based on the deviation of the measured variance to the shot-noise limit. This of course assumes, that we are shot-noise limited, which we will verify after the loss estimation.

To quantify the additional loss, the required attenuation is calculated such that the linear fit obtained from the raw variance passes through the origin. The attenuation by which we have to offset the data is 9.64 dB. By measuring the intensity behind the chip we calculate a total throughput of (28 ± 5)%, which includes the coupling loss and propagation losses of the chip. Thus, the remaining loss of (39 ± 5)% must come from the detectors and the fiber connections to the detector. We estimated the efficiency of one detector by measuring the count rate of the lower biased detector at two different bias points. For the bias of 6 µA we know the efficiency of (92 ± 5)%. When we compare the count rate at the lower bias current of 3.7 µA to the count rate at (92 ± 5)%, we estimate a detector efficiency of (36 ± 5)% which fits to the estimated loss from the previous calculation.

We can try to quantify the loss introduced by the chip further. After every fabrication step the propagation losses were characterized. After the patterning of the electrodes a clear increase of the optical propagation losses of $\Delta\alpha_{\mathrm{prop,TE}} = (0.86 \pm 0.03)$ dB and

$\Delta\alpha_{\mathrm{prop,TM}} = (1.72 \pm 0.3)$ dB were measured. The additional loss can arise from a coupling of the guided light to the overlying electrodes or remaining impurities after the lift-off process. To reduce coupling, the thickness of the silica buffer layer can be adjusted. The additional loss results in a total propagation loss of $\alpha_{\mathrm{prop,TE}} = (1.8 \pm 0.03)$ dB and $\alpha_{\mathrm{prop,TM}} = (3.1 \pm 0.3)$ dB for the two waveguide polarizations. Due to the difference in the propagation loss we had to adjust the bias current of the SNSPDs to arrive at equal count rates in both arms. Additionally, it has to be mentioned, that the propagation loss is only derived from the straight waveguide next to the investigated coupler structure. The used method for calculating the propagation losses can only be used for straight waveguides [81]. The losses introduced in the bends of the coupler could additionally introduce propagation losses which can add to the already asymmetric losses of TE and TM. Additional losses can also arise from the coupling to the chip, which results in the estimated loss of 9.64 dB. The estimated loss is used to calculate the actual LO power, which is then used for the x-axis in the main plot of fig. 6.6.

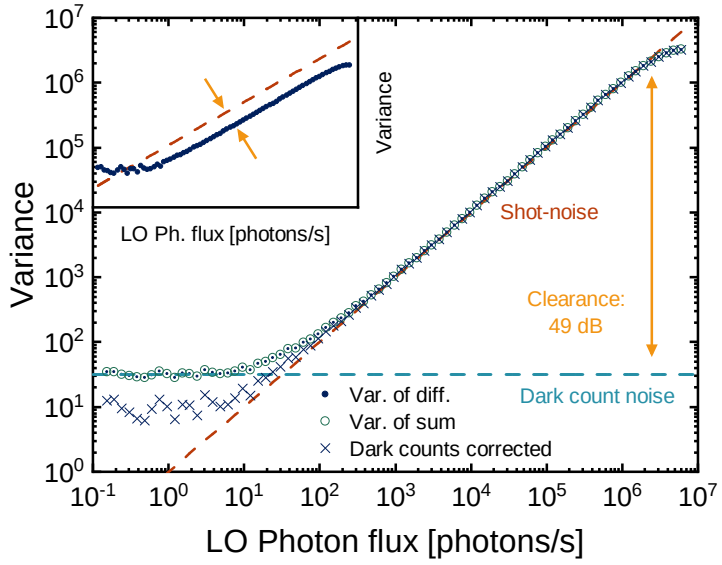

Figure 6.6: Measured variance of the difference and the sum of two SNSPD count rates. Because the variance of the sum is equal to the difference the detector is shot-noise limited. For a LO photon flux below 30 photons/s the variance is dominated by dark counts. When correcting the difference by subtracting the dark counts we can extend the linear regime. The SNSPDs can be considered as linear detectors for LO powers ranging from $30 - 2 \times 10^6$ photons/s. This leads to a maximum clearance of 49 dB. The inset shows the raw variance for a photon flux estimated with only the free-space attenuation of 60 dB.

Linearity and Shot-Noise Clearance

For the above procedure, we have assumed that the measured variance is indeed shot-noise

limited and not affected by additional noise such as the intensity noise of the laser source. In order to verify that the variance is actually limited by the quantum noise of the vacuum state, we compare the variance calculated for the subtracted signal of the two SNSPDs and the sum of both signals. It is known from literature [60] that when we calculate the variance of the sum, we measure the variance of the local oscillator regardless of the efficiency. If the laser light emitted from the laser source is not shot-noise limited and is influenced by additional noise sources like intensity noise, the variance of the sum and the difference should not be equal. They are only equal if the coherent state of the LO is quantum-noise limited and thus equal to the variance of a vacuum state. In fig. 6.6 the variance of the sum and the difference are plotted. When comparing the two curves, no clear difference can be seen, indicating that the tunable laser used is quantum-noise limited. Since we have demonstrated that the laser does not introduce any additional noise into the system, the previously described calculation for the LO power is valid considering the additional losses due to the chip.

With the correct estimation of the photon flux, we see that under a photon flux of 30 photons/s we measure the noise of the dark counts. When increasing the LO power, the measured noise increases linearly with the slope of 1, as predicted by eq. 6.15. By subtracting the dark count noise from the raw variance we can extend the linear regime of the detector down to the noise floor. In general the difference signal of the SNSPDs is linear over the range from $30 - 2 \times 10^6$ photons/s. For high powers we see a drop of in the variance since at this point the detector is not linear anymore. The fact that SNSPDs can be treated as linear detectors arises from the strongly attenuated laser light we consider. Because of the strong attenuation, we reduce the probability of two photons arriving at the detector within the detector's dead time to almost zero. So even if the detector is a click detector, it can count the number of photons that arrive at the detector in a given time window. As the photon flux increases, the probability of two photons arriving at the detector at the same time increases. Since one of the two cannot be detected, the detection events of SNSPDs are no longer linearly proportional to the actual photon count (i.e. the LO power). The described process is illustrated in fig. 6.7. For this reason we could increase the linear regime of the detector by using SNSPDs with shorter dead times.

From the data we can calculate the shot-noise clearance η_{SNC} of the homodyne detector which is given by

$$\eta_{\mathrm{SNC}} = \frac{V_{\mathrm{DN}}}{V_{\mathrm{max}}}. \tag{6.17}$$

V_{DN} is defined as the variance of the dark noise and V_{max} is the variance of the measured signal at the highest intensity of the LO where the detector is still linear. For the measured data we achieve a shot-noise clearance of $\eta_{\mathrm{SNC}} = 49$ dB. The measured shot-noise clearance is, to the best of my knowledge, the highest reported clearance for an optical homodyne detector. The high clearance suggests that SNSPDs may be of interest for measuring large amounts of squeezing. In this case we are interested in reduction of noise in comparison to the shot-noise limit. One can only measure as much squeezing as your clearance, since

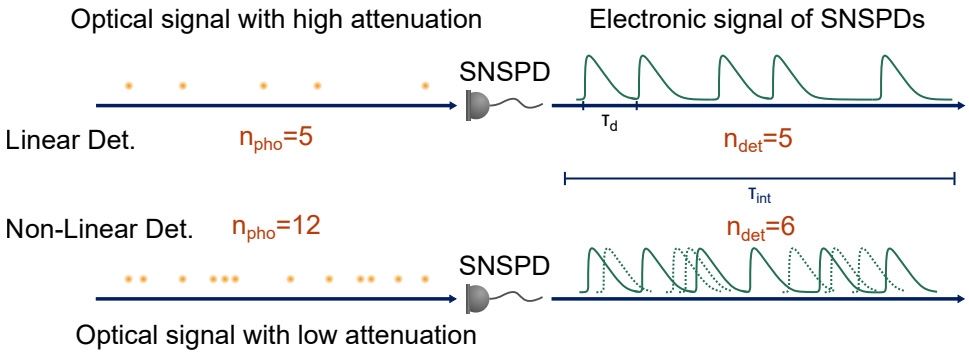

Figure 6.7: Schematic of the detection process with an SNSPDs with a high and low attenuation of a contentious wave (cw) laser source. At high attenuation, the detector is treated linearly since there are no two photons within the dead time τ_d of the detector. Over the integration time τ_{int} all 5 photons absorbed by the detector (n_{pho}) are recorded (n_{det}). For a low attenuation, not every photon can be detected by the SNSPD. Therefore, the detector signal is no longer linearly proportional to the power of the signal.

we cannot measure a noise reduction below the noise floor given by the dark counts. By using SNSPDs with even lower dark count rates and faster recovery times, we would be able to increase the clearance even further. If we do not consider additional optical losses, the utilized SNSPDs could in principle be used to measure squeezing up to 49 dB. The use of SNSPDs specifically designed for homodyne detection could further increase the measurable squeezing.

For this to be a viable application in the future, we need a system efficiency that is close to unity, including all components required to perform a homodyne experiment. To put this in perspective, assuming infinite squeezing, we would need a homodyne detector with an overall efficiency of 99.999% to measure 49 dB squeezing. SNSPDs have not reached these figures of merit. Nevertheless, with the reported 98% SDE of SNSPDs [24] we would be able to measure already $\approx$ 17 dB of squeezing. This does not include additional loss from other optical components.

In the presented experiment, the limiting factor for the application of measuring squeezing is the loss introduced by the combination of the integrated chip and the off-chip SNSPDs. The asymmetric loss leads to unequal bias of the detectors, which further reduces the efficiency of the detector. Considering the derived losses of the system, we could measure less than 0.5 dB of squeezing. Nevertheless, this does not limit the performance of the SNSPDs. To show the full potential of SNSPDs, they should be investigated individually in a conventional bulk optics homodyne setup. The combination with squeezed light can also be used to determine the efficiency of detectors. If we have a well known squeezing source, we can derive the detector efficiency from the measured squeezing with the SNSPDs. For example Vahlbruch et al. [175] have demonstrated calibration of photodiodes with 15 dB squeezing.

The Influence of the Number of Samples

In a next step, I would like to discuss the influence of the number of samples used to calculate the variance. For the above measurement we used a detector bandwidth of 2 MHz and a total measurement time of 5 s for each set attenuation. For an actual homodyne detection we would restrict ourselves to a single LO power. This is ideally a high LO power where we can still treat the SNSPDs as linear detectors to be well above the noise floor of the detectors. To then quantify the variance of a single state at a certain point in phase space we need to define a measurement window over which we can calculate the variance. In the previous measurement, this would have been 5 s, resulting in 10 MSa over the entire measurement time. But do you really require that many samples? To answer this questions we calculated the variance for different samples sizes. In fig. 6.8 the variance for different sample sizes ranging from 5 kSa to 10 MSa are plotted. For each curve, the data is shifted by one order of magnitude to make the difference in the data more visible.

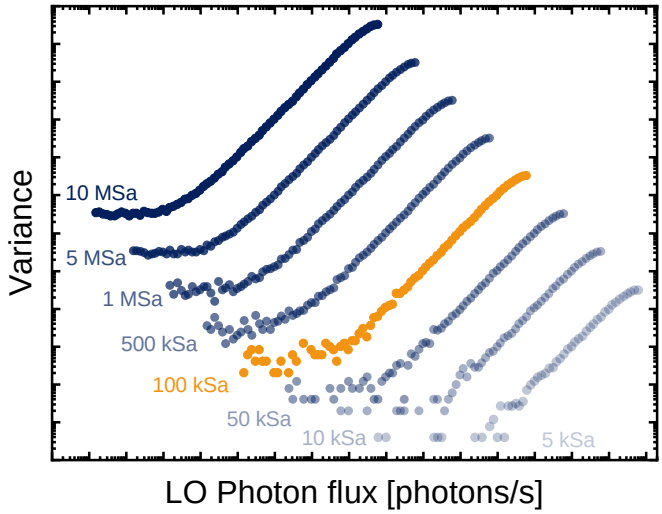

Figure 6.8: The measured quantum noise of the vacuum state is plotted for different sample sizes. For a sample size of 100 kSa the linear behavior of the detector is still well preserved.

From the different graphs we see that the linear behavior of the detector is still well preserved for the highlighted sample size of 100 kSa. For the given integration window of 500 ns this would lead to a total required measurement time of 50 ms. The reduced measurement time is beneficial when it comes to measuring phase-dependent signals like squeezed states, where drifts in the phase could potentially decrease the measured squeezing due to low-frequency noise. For smaller sample sizes the detector can still be used with a reduced linearity which will ultimately limit the total amount of measurable squeezing. For 5 kSa we still calculate a linear regime of 23 dB, limiting the measurable squeezing to 23 dB. For this setting we would only require a measurement time of 2.5 ms. In addition to reducing the effects of low-frequency noise, decreasing the measurement time

has the practical advantage of reducing the amount of data stored based on the recorded time stamps.

If we want to continue using the homodyne detector to characterize a state in phase space, we now need control over the phase between the quantum state under investigation and the LO. With a precise control we would be able to characterize the state in phase space and reconstruct its Wigner function. Therefore, I want to investigate the influence of the integrated phase shifter.

6.3.3 Phase-Dependent Loss

When we consider the homodyne detection of a vacuum state, we do not expect any phase dependency on the vacuum state. In phase space, the phase is defined as the angle between the amplitude vector of the state and the quadrature axis (see fig. 6.1 a)). Because the vacuum state is at the origin, the phase is not defined and therefore the signal should have no phase dependence.

Nevertheless, when scanning through the phase with the integrated phase shifter a clear modulation of the signal is visible (see. fig. 6.9). To quantify the magnitude of the fluctuation, we measure the counts at both detectors over 1 s and calculate the sum for each set voltage of the phase shifter V_{PS} and the polarization converter V_{PC}. We scanned the voltage for both modulators in the range of $0 - 30$ V. We normalized the calculated sum to the counts measured for $V_{\mathrm{PC}} = 17$ V and $V_{\mathrm{PS}} = 0$ V, since this is the operating point of the previously performed measurements. The resulting map of the normalized sum is shown in fig.6.9 a).

From the previous investigations we could already conclude that the chip has a polarization dependent loss resulting from the different propagation losses of TE and TM. This leads to a significant modulation of the sum when sampling the voltage of the PC. However, from the plot shown in fig. 6.9 a), we can see a clear modulation that depends on V_{PS}. Since it occurs in the sum of the two outputs of the beam splitter, the modulation is interpreted as an additional loss term for the LO. To ensure that this is an effect of the on-chip phase modulator, we connected the fiber stretcher to the arm of the LO. By applying a voltage to the fiber stretcher, we can additionally modulate the phase off-chip. In this case, no modulation can be seen in the sum.

In phase space, the phase-dependent loss can be thought of as the distance of the LO from the origin changing as a function of the voltage applied to the PS. For a homodyne experiment this is a crucial issue since depending on the phase/loss the measured variance changes. In a subsequent analysis of the data to reconstruct the Wigner function, it would not be clear whether the measured change in difference signal or variance results from the actual quantum state under investigation or the loss caused by the change in phase.

To solve this problem, we tried to calibrate the detector by measuring the map shown in Fig. 6.9 and taking the loss into account when post-processing the measured data. To check the stability of this calibration, we measured the phase-dependent loss several times

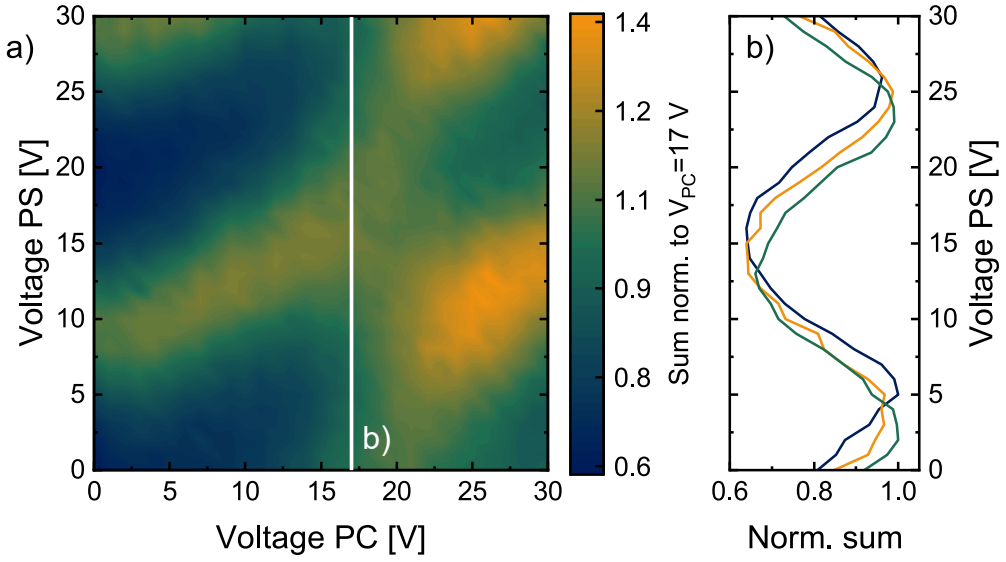

Figure 6.9: a) shows the normalized sum over both output arms of the integrated PBS for different voltages applied to the polarization converter (PC) and the phase shifter (PS). A clear modulation in the sum is visible. In b), three different measurement runs for the in white highlighted setting of the polarization converter are shown. The three measurements were taken over the course of 5 minutes.

for $V_{PC} = 17$ V, since this will be the operating point of the polarization converter. Three different measurements made over the course of 5 minutes are shown in Fig. 6.9 b). It can be seen that the phase-dependent loss changes depending on the measurement run, which makes it difficult to calibrate the phase-dependent loss.

The origin of this phase-dependent loss is still unclear. One could assume that the fluctuations visible in the sum are due to the modulation of a Fabry-Pérot resonator. Due to the refractive index contrast at the end facets of the chip, the chip itself forms a Fabry-Pérot resonator. By applying a voltage to the phase shifter, we change the optical path length of the chip and thus the interference conditions of the resonator. This can lead to a modulation as shown in the fig. 6.9 b). When calculating the contrast K for a titanium in-diffused waveguide according to [81]

$$K = \frac{I_{max} - I_{min}}{I_{max} + I_{min}} = \frac{2\tilde{R}}{1 - \tilde{R}^2} \tag{6.18}$$

we have an estimated contrast of 0.26. For the given contrast, it is assumed that the reflectance $\tilde{R} = R \exp \alpha$ of the end facet takes into account only the reflectance R without considering the total propagation losses α. In this case the approximated contrast would fit well to the measured contrast of $\approx 22\%$. Adding the additional propagation losses in the calculation for the contrast would significantly reduce the 26%. In order to verify, if the

visible effects arise from the chip resonator, we could potentially tune the temperature of the chip to see if the measured fluctuations have the same order of magnitude. Tuning the temperature would result in a change of the optical path length, just like the modulation of the refractive index. In this case, an anti-reflection coating would be required on one end facet of the chip to break the resonator.

Although we have not used phase modulation to reconstruct the Wigner function of a weak coherent state as a signal, we have been able to demonstrate the potential of SNSPDs in the context of strong-field homodyne detection. The long linearity and resulting high shot-noise clearance make them an ideal candidate for measuring large amounts of squeezing. To exploit the full potential, the overall efficiency of the homodyne detector needs to be further improved so that losses do not limit the performance of the homodyne detector with SNSPDs.

Chapter Summary: The goal of this section was to investigate the feasibility of SNSPDs in the context of strong-field homodyne detection. While SNSPDs are normally used to investigate the particle-like nature of light and measure photon-counting statistics, homodyne detection is a method that measures the wave-like nature of light. By combining standard homodyne detection with SNSPDs, we could develop a versatile detector capable of switching between the wave-like and particle-like nature of light.

To verify the feasibility of SNSPDs in this context, we combined off-chip SNSPDs with an integrated interferometer in Ti:LN. Although losses due to chip coupling and propagation limit the usability of the chip in terms of squeezing measurement, we demonstrated that SNSPDs can act as a linear detector and can be used for strong-field homodyne. We were able to measure a shot-noise clearance of $\eta_{\mathrm{SNC}} = 49$ dB at 2 MHz, which is to the best of my knowledge the highest reported clearance for an optical homodyne detector [51]. Even with a sample size of 5 kSa (resulting in 2.5 ms) measurement time) we calculate a clearance of 23 dB which is comparable to other detectors [51]. When using detectors with lower dark counts and shorter recovery time, we could even increase the clearance further.

The high clearance enables the measurement of high amounts of squeezing. One challenge that we encountered during the experiments is the unequal efficiency of our detectors. In standard homodyne detection the photodiodes have a separate variable gain which can be adjusted so that the signal of both photodiodes is equal. In our case we had to reduce the efficiency of one detector by biasing it at a different current. In the context of homodyne detection, this is treated as loss, which is not ideal when characterizing squeezed light. The proposed idea based on superconducting electronics could solve this problem and further improve the versatile use of SNSPDs in the context of homodyne detection.

Conclusion and Outlook 7

In this work, I have presented the progress I have made on developing the patterning process for different types of devices in lithium niobate, so that in the end they could be combined to demonstrate the first homodyne experiment with superconducting nanowire single-photon detectors. The device toolbox consists of low-loss Ti:LN waveguides, periodic poling for quasi-phase matching and electro-opitic modulators. All of them were fabricated with a maskless direct laser lithography which allows for fast and rapid prototyping. The presented results can be understood as proof-of-principle experiments, to see if the fabricated components achieve a standards of performance, known for Ti:LN waveguides.

The results achieved for the periodic poling are especially noteworthy. The high precision and accuracy may enable the fabrication of smaller poling periods or aperiodic poling for customizing the phase-matching condition. Not only Ti:LN may benefit from this in the future but also other nonlinear material platforms like potassium titanyl phosphate (KTP). The efficient generation of single photons and squeezed states will find use in many quantum applications. Fabricating these with a high degree of flexibility is beneficial for matching the versatile requirements of future experiments. Using direct laser writing, we were able to show phase-matching conditions for SHG that were within 0.3 nm of the expected phase-matching wavelength. The average effective pole length, a measure of the uniformity of the periodic poling, is $(79 \pm 2)\%$.

Nevertheless, the fabrication can be further improved and further evaluated. Whether the presented accuracy and precision can be achieved on a longer time scale and over several samples must still be investigated. The presented modulators have not been tested regarding their modulation speed. To achieve high modulation speeds (i.e. in the GHz range), electrodes with thicknesses of a few micrometers or greater will be required [176]. For these, the fabrication process would need to be reoptimized.

The presented toolbox can not only be used for classical optics experiments but also for the research field of quantum optics where we consider particle-like photons to describe the light. State-of-the-art SNSPDs can be used to measure these quanta of light. I presented the first demonstration of micron-wide SNSPDs on silicon fabricated with a maskless optical lithography. Even though I could show a saturated internal detection efficiency for these detectors on silicon, realizing these on z-cut lithium niobate remains a challenge. I have shown different approaches to enhance the performance and the yield of SNSPDs. ITO is an especially promising candidate to overcome the pyroelectric damage of detectors. Further research needs to be done in the future to show the feasibility of SNSPDs on ITO. I believe that SNSPDs should therefore be considered with a thicker film first. Even though this increases the demands on the structuring process, it reduces the demands on film homogeneity and surface roughness.

Still, mircon-wide SNSPDs and their fabrication with optical lithography enables the patterning of large-area detectors that could be used for applications in dark matter search [159] or increasing the system detection efficiencies for integrated detector on low-contrast waveguides [94]. With the transition to the micrometer scale we gain the possibility to combine the detectors with other structures at the same scale to boost the performance of SNSPDs for specific applications. SNSPDs, for example, do not offer an intrinsic spectral resolution of an incoming light signal. Many approaches have been investigated to encode spectral information in the signal of SNSPDs [177]. Cheng et al. [178] demonstrated a spectrometer based on a dispersive grating, while Kong et al. changed the detector geometry to encode spectral information in the signal information [179]. A last example was demonstrated by Zheng et al. [177] that used the meta surfaces to gain spectral information.

Up to this point there has been no combination of micron-wide SNSPDs with plasmonic nanoantennas to boost the spectral responsivity of these detectors. Heath et al. [180] demonstrated the combination of normal SNSPDs with nanorods to increase the system detection efficiency. Arranging the plasmonic nanoantennas in an array with a lattice resonance close to the resonance of the nanoantenna narrows the bandwidth of the nanoantenna and enhances the field localization around the nanorod [181], which would also lead to an increase in the system detection efficiency [180]. The dimensions of a micron-wide meander detector and the lattice constant of the nanoantennas are on the same scale, which is beneficial when it comes to combining the two structures. By combining them, we would impose the spectral characteristics of the nanoantennas on the SNSPDs. The presented idea could be interesting to pursue in the future.

In the scope of this work, SNSPDs were additionally used to demonstrate a strong-field homodyne experiment for the first time. Strong-field homodyne is seen as an experiment conducted in the wave-like picture of light. Here we utilized detectors, normally used to reveal particle-like phenomena of light, to demonstrate an interference experiment. The combination of the components realized in the first part of this work with off-chip SNSPDs showed that the SNSPDs can be used as a linear detector for strong-field homodyne detection. Due to the excellent signal-to-noise ratio of SNSPDs we could investigate a linear behavior of the detector down to a photon flux of 30 photons/s. This can be interpreted as the minimal laser power for which strong-field homodyne detection can be performed. The long linearity of the SNSPDs leads to a shot-noise clearance of 49 dB at 2 MHz, which is the highest reported clearance for a homodyne detector [51]. Thus, SNSPDs are an interesting candidate when a high degree of squeezing must be measured. By using SNSPDs with quasi-photon-number resolution and reducing the power of the LO, we have a set of detectors that can be used for strong-field and weak-field homodyne detection.

If we want to pick up the thread we started in the introduction, we have shown with the recent homodyne experiment that SNSPDs can be used in this context. This makes them a versatile detector that can be used to gain insights on light on both sides of the wave-particle duality.

Bibliography 8

[1] T. Young, I. The Bakerian Lecture. Experiments and calculations relative to physical optics, Philosophical Transactions of the Royal Society of London **94**, 1–16 (1804).

[2] D. P. Hampshire, A derivation of Maxwell's equations using the Heaviside notation, Philosophical Transactions of the Royal Society A: Mathematical, Physical and Engineering Sciences **376**, 20170447 (2018).

[3] K. Okamoto, "Planar optical waveguides", in *Fundamentals of optical waveguides* (Academic Press, 2006), pp. 13–55.

[4] E. Agrell et al., Roadmap of optical communications, Journal of Optics **18**, 063002 (2016).

[5] M. Planck, Zur Theorie des Gesetzes der Energieverteilung im Normalspectrum, Physik Journal **4**, 146–151 (1948).

[6] N. Bohr, The quantum postulate and the recent development of atomic theory, Nature **121**, 580–590 (1928).

[7] H. S. Zhong et al., Quantum computational advantage using photons, Science **370**, 1460–1463 (2020).

[8] L. S. Madsen et al., Quantum computational advantage with a programmable photonic processor, Nature **606**, 75–81 (2022).

[9] N. Hosseinidehaj, Z. Babar, R. Malaney, S. X. Ng, and L. Hanzo, Satellite-based continuous-variable quantum communications: State-of-the-art and a predictive outlook, IEEE Communications Surveys and Tutorials **21**, 881–919 (2019).

[10] S. Wang et al., Twin-field quantum key distribution over 830-km fibre, Nature Photonics **16**, 154–161 (2022).

[11] J. Aasi et al., Enhanced sensitivity of the LIGO gravitational wave detector by using squeezed states of light, Nature Photonics **7**, 613–619 (2013).

[12] C. Gerry and P. Knight, *Introductory quantum optics* (Cambridge University Press, 2004).

[13] H.-A. Bachor and T. C. Ralph, *A guide to experiments in quantum optics*, 2nd (Wiley, 2019).

[14] K. Laiho, M. Avenhaus, K. N. Cassemiro, and C. Silberhorn, Direct probing of the Wigner function by time-multiplexed detection of photon statistics, New Journal of Physics **11**, 043012 (2009).

[15] K. Laiho, K. N. Cassemiro, D. Gross, and C. Silberhorn, Probing the negative wigner function of a pulsed single photon point by point, Phys. Rev. Lett. **105**, 253603 (2010).

[16] G. Harder, C. Silberhorn, J. Rehacek, Z. Hradil, L. Motka, B. Stoklasa, and L. L. Sánchez-Soto, Local sampling of the wigner function at telecom wavelength with loss-tolerant detection of photon statistics, Physical Review Letters **116**, 133601 (2016).

[17] D. Achilles, C. Silberhorn, and I. A. Walmsley, Direct, loss-tolerant characterization of nonclassical photon statistics, Physical Review Letters **97**, 1–4 (2006).

[18] R. H. Hadfield, Single-photon detectors for optical quantum information applications, Nature Photonics **3**, 696–705 (2009).

[19] J. A. Lau, V. B. Verma, D. Schwarzer, and A. M. Wodtke, Superconducting single-photon detectors in the mid-infrared for physical chemistry, Chemical Society Reviews **52**, 921–941 (2023).

[20] A. J. Miller, B. Cabrera, R. W. Romani, E. Figueroa-Feliciano, S. W. Nam, and R. M. Clarke, Development of wide-band, time and energy resolving, optical photon detectors with application to imaging astronomy, Nuclear Instruments and Methods in Physics Research, Section A: Accelerators, Spectrometers, Detectors and Associated Equipment **444**, 445–448 (2000).

[21] G. N. Gol'tsman, O. Okunev, G. Chulkova, A. Lipatov, A. Semenov, K. Smirnov, B. Voronov, A. Dzardanov, C. Williams, and R. Sobolewski, Picosecond superconducting single-photon optical detector, Applied Physics Letters **79**, 705 (2001).

[22] A. E. Lita, A. J. Miller, and S. W. Nam, Counting near-infrared single-photons with 95% efficiency, Optics Express **16**, 3032 (2008).

[23] L. You, Superconducting nanowire single-photon detectors for quantum information, Nanophotonics **9**, 2673–2692 (2020).

[24] D. V. Reddy, R. R. Nerem, S. W. Nam, R. P. Mirin, and V. B. Verma, Superconducting nanowire single-photon detectors with 98% system detection efficiency at 1550 nm, Optica **7**, 1649–1653 (2020).

[25] J. Chang et al., Detecting telecom single photons with $\left(99.5^{+0.5}_{-2.07}\right)$ % system detection efficiency and high time resolution, APL Photonics **6**, 036114 (2021).

[26] J. Chiles et al., New constraints on dark photon dark matter with superconducting nanowire detectors in an optical haloscope, Physical Review Letters **128**, 231802 (2022).

[27] B. Korzh et al., Demonstration of sub-3 ps temporal resolution with a superconducting nanowire single-photon detector, Nature Photonics **14**, 250–255 (2020).

[28] M. J. Fitch, B. C. Jacobs, T. B. Pittman, and J. D. Franson, Photon-number resolution using time-multiplexed single-photon detectors, Physical Review A **68**, 043814 (2003).

[29] D. Achilles, C. Silberhorn, C. Śliwa, K. Banaszek, and I. A. Walmsley, Fiber-assisted detection with photon number resolution, Optics Letters **28**, 2387 (2003).

[30] E. Dauler, B. Robinson, A. Kerman, J. Yang, E. Rosfjord, V. Anant, B. Voronov, G. Gol'tsman, and K. Berggren, Multi-element superconducting nanowire single-photon detector, IEEE Transactions on Applied Superconductivity **17**, 279–284 (2007).

[31] D. Gottesman and J. Preskill, "Secure quantum key distribution using squeezed states", in *Quantum information with continuous variables* (Springer, Dordrecht, 2003), pp. 317–356.

[32] A. I. Lvovsky, Squeezed light, Photonics: Scientific Foundations, Technology and Applications **1**, 121–163 (2015).

[33] U. L. Andersen, G. Leuchs, and C. Silberhorn, Continuous-variable quantum information processing, Laser and Photonics Reviews **4**, 337–354 (2010).

[34] M. Hillery, Quantum cryptography with squeezed states, Physical Review A **61**, 022309 (2000).

[35] Y.-C. Zhang, Z. Li, S. Yu, W. Gu, X. Peng, and H. Guo, Continuous-variable measurement-device-independent quantum key distribution using squeezed states, Physical Review A **90**, 052325 (2014).

[36] U. Leonhardt and H. Paul, Measuring the quantum state of light, Progress in Quantum Electronics **19**, 89–130 (1995).

[37] S. L. Braunstein, Homodyne statistics, Physical Review A **42**, 474 (1990).

[38] M. G. Raymer, J. Cooper, H. J. Carmichael, M. Beck, and D. T. Smithey, Ultrafast measurement of optical-field statistics by dc-balanced homodyne detection, Journal of the Optical Society of America B **12**, 1801 (1995).

[39] G. Breitenbach, S. Schiller, and J. Mlynek, Measurement of the quantum states of squeezed light, Nature **387**, 471–475 (1997).

[40] E. Wigner, On the quantum correction for thermodynamic equilibrium, Physical Review **40**, 749–759 (1932).

[41] A. I. Lvovsky, H. Hansen, T. Aichele, O. Benson, J. Mlynek, and S. Schiller, Quantum state reconstruction of the single-photon Fock state, Physical Review Letters **87**, 050402 (2001).

[42] G. Puentes, A. Datta, A. Feito, J. Eisert, M. B. Plenio, and I. A. Walmsley, Entanglement quantification from incomplete measurements: applications using photon-number-resolving weak homodyne detectors, New Journal of Physics **12**, 033042 (2010).

[43] G. Donati, T. J. Bartley, X. M. Jin, M. D. Vidrighin, A. Datta, M. Barbieri, and I. A. Walmsley, Observing optical coherence across Fock layers with weak-field homodyne detectors, Nature Communications **5**, 5584 (2014).

[44] G. S. Thekkadath et al., Tuning between photon-number and quadrature measurements with weak-field homodyne detection, Physical Review A **101**, 031801 (2020).

[45] G. S. Thekkadath, B. A. Bell, I. A. Walmsley, and A. I. Lvovsky, Engineering Schrödinger cat states with a photonic even-parity detector, Quantum **4**, 239 (2020).

[46] A. I. Lvovsky and M. G. Raymer, Continuous-variable optical quantum-state tomography, Reviews of Modern Physics **81**, 299–332 (2009).

[47] S. L. Braunstein and P. van Loock, Quantum information with continuous variables, Reviews of Modern Physics **77**, 513–577 (2005).

[48] N. C. Menicucci, P. van Loock, M. Gu, C. Weedbrook, T. C. Ralph, and M. A. Nielsen, Universal quantum computation with continuous-variable cluster states, Physical Review Letters **97**, 110501 (2006).

[49] U. L. Andersen, J. S. Neergaard-Nielsen, P. Van Loock, and A. Furusawa, Hybrid discrete- and continuous-variable quantum information, Nature Physics **11**, 713–719 (2015).

[50] X. Jin, J. Su, Y. Zheng, C. Chen, W. Wang, and K. Peng, Balanced homodyne detection with high common mode rejection ratio based on parameter compensation of two arbitrary photodiodes, Optics Express **23**, 23859 (2015).

[51] C. Bruynsteen, M. Vanhoecke, J. Bauwelinck, and X. Yin, Integrated balanced homodyne photonic–electronic detector for beyond 20 GHz shot-noise-limited measurements, Optica **8**, 1146–1152 (2021).

[52] E. Diamanti, H.-K. Lo, B. Qi, and Z. Yuan, Practical challenges in quantum key distribution, npj Quantum Information **2**, 16025 (2016).

[53] C. Porto, D. Rusca, S. Cialdi, A. Crespi, R. Osellame, D. Tamascelli, S. Olivares, and M. G. A. Paris, Detection of squeezed light with glass-integrated technology embedded into a homodyne detector setup, Journal of the Optical Society of America B **35**, 1596–1602 (2018).

[54] L. Huang and H. Zhou, Integrated Gbps quantum random number generator with real-time extraction based on homodyne detection, Journal of the Optical Society of America B **36**, B130–B136 (2019).

[55] F. Mondain, T. Lunghi, A. Zavatta, E. Gouzien, F. Doutre, M. De Micheli, S. Tanzilli, and V. D'Auria, Chip-based squeezing at a telecom wavelength, Photonics Research **7**, A36–A39 (2019).

[56] F. Raffaelli, G. Ferranti, D. H. Mahler, P. Sibson, J. E. Kennard, A. Santamato, G. Sinclair, D. Bonneau, M. G. Thompson, and J. C. Matthews, A homodyne detector integrated onto a photonic chip for measuring quantum states and generating random numbers, Quantum Science and Technology **3**, 25003 (2018).

[57] F. Kaiser, B. Fedrici, A. Zavatta, V. D'Auria, and S. Tanzilli, A fully guided-wave squeezing experiment for fiber quantum networks, Optica **3**, 362 (2016).

[58] F. Lenzini et al., Integrated photonic platform for quantum information with continuous variables, Science Advances **4**, eaat9331 (2018).

[59] G. Zhang et al., An integrated silicon photonic chip platform for continuous-variable quantum key distribution, Nature Photonics **13**, 839–842 (2019).

[60] B. C. Buchler, "Electro-optic control of quantum measurements", PhD thesis (2001).

[61] M. S. Stefsky, "Generation and detection of low-frequency squeezing for gravitational-wave detection", PhD thesis (Australian National University, 2012).

[62] J. Wang, F. Sciarrino, A. Laing, and M. G. Thompson, Integrated photonic quantum technologies, Nature Photonics **14**, 273–284 (2020).

[63] G. Moody et al., 2022 Roadmap on integrated quantum photonics, J. Phys. Photonics **4**, 012501 (2022).

[64] H. Wang et al., High-efficiency multiphoton boson sampling, Nature Photonics **11**, 361–365 (2017).

[65] R. Prevedel, P. Walther, F. Tiefenbacher, P. Böhi, R. Kaltenbaek, T. Jennewein, and A. Zeilinger, High-speed linear optics quantum computing using active feed-forward, Nature **445**, 65–69 (2007).

[66] J. W. Silverstone, D. Bonneau, J. L. Obrien, and M. G. Thompson, Silicon quantum photonics, IEEE Journal of Selected Topics in Quantum Electronics **22**, 390–402 (2016).

[67] L. M. Rosenfeld, D. A. Sulway, G. F. Sinclair, V. Anant, M. G. Thompson, J. G. Rarity, and J. W. Silverstone, Mid-infrared quantum optics in silicon, Optics Express **28**, 37092–37102 (2020).

[68] J. Biele, J. F. Tasker, J. W. Silverstone, and J. C. F. Matthews, Shot-noise limited homodyne detection for MHz quantum light characterisation in the 2 μm band, Optics Express **30**, 7716 (2022).

[69] M. W. Puckett et al., 422 Million intrinsic quality factor planar integrated all-waveguide resonator with sub-MHz linewidth, Nature Communications **12**, 934 (2021).

[70] R. Kumar, J. R. Ong, M. Savanier, and S. Mookherjea, Controlling the spectrum of photons generated on a silicon nanophotonic chip, Nature Communications **5**, 5489 (2014).

[71] E. Timurdogan, C. V. Poulton, M. J. Byrd, and M. R. Watts, Electric field-induced second-order nonlinear optical effects in silicon waveguides, Nature Photonics **11**, 200–206 (2017).

[72] A. Mittelstädt, A. Schliwa, and P. Klenovský, Modeling electronic and optical properties of III–V quantum dots—selected recent developments, Light: Science & Applications **11**, 17 (2022).

[73] P. Schnauber, A. Singh, J. Schall, S. I. Park, J. D. Song, S. Rodt, K. Srinivasan, S. Reitzenstein, and M. Davanco, Indistinguishable photons from deterministically integrated single quantum dots in heterogeneous GaAs/Si3N4 quantum photonic circuits, Nano Letters **19**, 7164–7172 (2019).

[74] C. P. Dietrich, A. Fiore, M. G. Thompson, M. Kamp, and S. Höfling, GaAs integrated quantum photonics: Towards compact and multi-functional quantum photonic integrated circuits, Laser and Photonics Reviews **10**, 870–894 (2016).

[75] A. W. Elshaari, W. Pernice, K. Srinivasan, O. Benson, and V. Zwiller, Hybrid integrated quantum photonic circuits, Nature Photonics **14**, 285–298 (2020).

[76] M. Catti, "Physical properties of crystals: Phenomenology and modelling", in *Fundamentals of crystallography* (Oxford University Press, 2011), pp. 776–830.

[77] T. Kashiwazaki, N. Takanashi, T. Yamashima, T. Kazama, K. Enbutsu, R. Kasahara, T. Umeki, and A. Furusawa, Continuous-wave 6-dB-squeezed light with 2.5-THz-bandwidth from single-mode PPLN waveguide, APL Photonics **5**, 036104 (2020).

[78] K. Luke, P. Kharel, C. Reimer, L. He, M. Loncar, and M. Zhang, Wafer-scale low-loss lithium niobate photonic integrated circuits, Optics Express **28**, 24452–24458 (2020).

[79] S. Kang, R. Zhang, Z. Hao, D. Jia, F. Gao, F. Bo, G. Zhang, and J. Xu, High-efficiency chirped grating couplers on lithium niobate on insulator, 2021 Conference on Lasers and Electro-Optics, CLEO 2021 - Proceedings **45**, 6651–6654 (2021).

[80] R. V. Schmidt and I. P. Kaminow, Metal-diffused optical waveguides in LiNbO3, Applied Physics Letters **25**, 458 (1974).

[81] R. Regener and W. Sohler, Loss in low-finesse Ti:LiNbO3 optical waveguide resonators, Applied Physics B Photophysics and Laser Chemistry **36**, 143–147 (1985).

[82] P. R. Sharapova, K. H. Luo, H. Herrmann, M. Reichelt, T. Meier, and C. Silberhorn, Toolbox for the design of LiNbO3-based passive and active integrated quantum circuits, New Journal of Physics **19**, 123009 (2017).

[83] J. P. Höpker et al., Integrated transition edge sensors on titanium in-diffused lithium niobate waveguides, APL Photonics **4**, 056103 (2019).

[84] N. Montaut, L. Sansoni, E. Meyer-Scott, R. Ricken, V. Quiring, H. Herrmann, and C. Silberhorn, High-efficiency plug-and-play source of heralded single photons, Physical Review Applied **8**, 024021 (2017).

[85] W. Sohler et al., Integrated optical devices in lithium niobate, Optics and Photonics News **19**, 24–31 (2008).

[86] K.-H. Luo, S. Brauner, C. Eigner, P. R. Sharapova, R. Ricken, T. Meier, H. Herrmann, and C. Silberhorn, Nonlinear integrated quantum electro-optic circuits, Science Advances **5**, eaat1451 (2019).

[87] S. Miki, M. Takeda, M. Fujiwara, M. Sasaki, A. Otomo, and Z. Wang, Superconducting NbTiN nanowire single photon detectors with low kinetic inductance, Applied Physics Express **2**, 14–17 (2009).

[88] X. Yang, L. You, L. Zhang, C. Lv, H. Li, X. Liu, H. Zhou, and Z. Wang, Comparison of superconducting nanowire single-photon detectors made of NbTiN and NbN thin films, IEEE Transactions on Applied Superconductivity **28**, 2200106 (2018).

[89] E. E. Wollman et al., UV superconducting nanowire single-photon detectors with high efficiency, low noise, and 4 K operating temperature, Optics Express **25**, 26792–26801 (2017).

[90] D. Y. Vodolazov, Current dependence of the red boundary of superconducting single-photon detectors in the modified hot-spot model, Physical Review B **90**, 054515 (2014).

[91] E. E. Wollman, V. B. Verma, A. E. Lita, W. H. Farr, M. D. Shaw, R. P. Mirin, and S. Woo Nam, Kilopixel array of superconducting nanowire single-photon detectors, Optics Express **27**, 35279–35289 (2019).

[92] V. B. Verma et al., Single-photon detection in the mid-infrared up to 10 μm wavelength using tungsten silicide superconducting nanowire detectors, APL Photonics **6**, 056101 (2021).

[93] I. Esmaeil Zadeh, J. Chang, J. W. Los, S. Gyger, A. W. Elshaari, S. Steinhauer, S. N. Dorenbos, and V. Zwiller, Superconducting nanowire single-photon detectors: A perspective on evolution, state-of-the-art, future developments, and applications, Applied Physics Letters **118**, 190502 (2021).

[94] J. P. Höpker et al., Integrated superconducting nanowire single-photon detectors on titanium in-diffused lithium niobate waveguides, JPhys Photonics **3**, 034022 (2021).

[95] J. Chiles, S. M. Buckley, A. Lita, V. B. Verma, J. Allmaras, B. Korzh, M. D. Shaw, J. M. Shainline, R. P. Mirin, and S. W. Nam, Superconducting microwire detectors based on WSi with single-photon sensitivity in the near-infrared, Applied Physics Letters **116**, 242602 (2020).

[96] A. E. Lita, V. B. Verma, J. Chiles, R. P. Mirin, and S. W. Nam, Mo_xSi_{1-x} a versatile material for nanowire to microwire single-photon detectors from UV to near IR, Superconductor Science and Technology **34**, 054001 (2021).

[97] E. E. Wollman et al., Recent advances in superconducting nanowire single-photon detector technology for exoplanet transit spectroscopy in the mid-infrared, Journal of Astronomical Telescopes, Instruments, and Systems **7**, 011004 (2021).

[98] M. Protte, V. B. Verma, J. P. Höpker, R. P. Mirin, S. Woo Nam, and T. J. Bartley, Laser-lithographically written micron-wide superconducting nanowire single-photon detectors, Superconductor Science and Technology **35**, 055005 (2022).

[99] N. A. Lange, J. P. Höpker, R. Ricken, V. Quiring, C. Eigner, C. Silberhorn, and T. J. Bartley, Cryogenic integrated spontaneous parametric down-conversion, Optica **9**, 108–111 (2022).

[100] F. Thiele et al., Cryogenic electro-optic modulation in titanium in-diffused lithium niobate waveguides, JPhys Photonics **4**, 034004 (2022).

[101] R. S. Weis and T. K. Gaylord, Lithium niobate: Summary of physical properties and crystal structure, Applied Physics A Solids and Surfaces **37**, 191–203 (1985).

[102] K. K. Wang, *Properties of lithium niobate*, 28th ed. (IET, 2002).

[103] N. A. Lange, T. Schapeler, J. P. Höpker, M. Protte, and T. J. Bartley, Degenerate photons from a cryogenic spontaneous parametric down-conversion source, arXiv, quant–ph, 2303.17428 (2023).

[104] F. Thiele, T. Hummel, A. N. McCaughan, J. Brockmeier, M. Protte, V. Quiring, S. Lengeling, C. Eigner, C. Silberhorn, and T. J. Bartley, All optical operation of a superconducting photonic interface, arXiv, quant–ph, 2302.12123 (2023).

[105] K. Okamoto, "Wave theory of optical waveguides", in *Fundamentals of optical waveguides* (Academic Press, 2006), pp. 1–12.

[106] B. D. Guenther, "Electromagnetic theory", in *Modern optics simplified*, 33rd ed. (Oxford University Press, 2019), pp. 20–52.

[107] K. Kawano and T. Kitoh, *Introduction to optical waveguide analysis* (John Wiley & Sons, Inc., New York, USA, 2001).

[108] M. Bartnick, M. Santandrea, J. P. Höpker, F. Thiele, R. Ricken, V. Quiring, C. Eigner, H. Herrmann, C. Silberhorn, and T. J. Bartley, Cryogenic second-harmonic generation in periodically poled lithium niobate waveguides, Physical Review Applied **15**, 024028 (2021).

[109] Thorlabs, *SMF-28-J9 optical fiber*, 2023.

[110] M. Bazzan and C. Sada, Optical waveguides in lithium niobate: Recent developments and applications, Applied Physics Reviews **2**, 040603 (2015).

[111] T. Rinke and C. Koch, *Fotolithografie: Grundlagen der Mikrostrukturierung*, Vol. 2 (2020), p. 143.

[112] A. Yariv, Coupled-Mode theory for guided-wave optics, IEEE Journal of Quantum Electronics **9**, 919–933 (1973).

[113] J. P. Höpker, "Integrated measurement-induced nonlinearity with superconducting detectors", PhD thesis (Paderborn University, 2022).

[114] R. Loudon and T. von Foerster, The quantum theory of light, American Journal of Physics **42**, 1041–1042 (1974).

[115] R. W. Boyd, *Nonlinear optics* (Academic press, 2008).

[116] D. N. Nikogosyan, *Nonlinear optical crystals: A complete survey* (Springer-Verlag, New York, 2005).

[117] V. Y. Shur, A. R. Akhmatkhanov, and I. S. Baturin, Micro- and nano-domain engineering in lithium niobate, Applied Physics Reviews **2**, 040604 (2015).

[118] S. Helmfrid, G. Arvidsson, and J. Webjörn, Influence of various imperfections on the conversion efficiency of second-harmonic generation in quasi-phase-matching lithium niobate waveguides, Journal of the Optical Society of America B **10**, 222–229 (1993).

[119] M. Santandrea, M. Stefszky, V. Ansari, and C. Silberhorn, Fabrication limits of waveguides in nonlinear crystals and their impact on quantum optics applications, New Journal of Physics **21**, 033038 (2019).

[120] M. Santandrea, PyNumericalPhasematching v1.0, doi : 10 . 5281 / zenodo . 3538004 (2019).

[121] V. K. Shukla and J. Ghosh, Generation of two different polarization-entangled biphoton states in a potassium titanyl phosphate waveguide device with multiple periodic poling, Physical Review A **101**, 023832 (2020).

[122] A. Warke and K. Thyagarajan, Direct generation of two-pair frequency entanglement via dual periodic poling in lithium niobate waveguides, European Physical Journal Plus **137**, 697 (2022).

[123] C. Wang, C. Langrock, A. Marandi, M. Jankowski, M. Zhang, B. Desiatov, M. M. Fejer, and M. Lončar, Ultrahigh-efficiency wavelength conversion in nanophotonic periodically poled lithium niobate waveguides, Optica **5**, 1438–1441 (2018).

[124] J. Lu, J. B. Surya, X. Liu, A. W. Bruch, Z. Gong, Y. Xu, and H. X. Tang, Periodically poled thin-film lithium niobate microring resonators with a second-harmonic generation efficiency of 250,000%/W, Optica **6**, 1455–1460 (2019).

[125] J. Zhao, C. Ma, M. Rüsing, and S. Mookherjea, High quality entangled photon pair generation in periodically poled thin-film lithium niobate waveguides, Physical Review Letters **124**, 163603 (2020).

[126] P. R. Sharapova, K. H. Luo, H. Herrmann, M. Reichelt, T. Meier, and C. Silberhorn, Toolbox for the design of LiNbO3-based passive and active integrated quantum circuits, New Journal of Physics **19**, 123009 (2017).

[127] C. Kießler, H. Conradi, M. Kleinert, V. Quiring, H. Herrmann, and C. Silberhorn, Fiber-coupled plug-and-play heralded single photon source based on Ti:LiNbO3 and polymer technology, arXiv, quant–ph, 2302.10976 (2023).

[128] A. Migdall, S. V. Polyakov, J. Fan, and J. C. Bienfang, *Single-photon generation and detection*, Vol. 45 (2013).

[129] L. A. Jiang, E. A. Dauler, and J. T. Chang, Photon-number-resolving detector with 10 bits of resolution, Physical Review A **75**, 062325 (2007).

[130] K. Takemoto, Y. Nambu, T. Miyazawa, Y. Sakuma, T. Yamamoto, S. Yorozu, and Y. Arakawa, Quantum key distribution over 120km using ultrahigh purity single-photon source and superconducting single-photon detectors, Scientific Reports **5**, 14383 (2015).

[131] G. Reithmaier, S. Lichtmannecker, T. Reichert, P. Hasch, K. Müller, M. Bichler, R. Gross, and J. J. Finley, On-chip time resolved detection of quantum dot emission using integrated superconducting single photon detectors, Scientific Reports **3**, 1901 (2013).

[132] W. H. Pernice, C. Schuck, O. Minaeva, M. Li, G. N. Goltsman, A. V. Sergienko, and H. X. Tang, High-speed and high-efficiency travelling wave single-photon detectors embedded in nanophotonic circuits, Nature Communications **3**, 1325 (2012).

[133] O. Kahl, S. Ferrari, V. Kovalyuk, G. N. Goltsman, A. Korneev, and W. H. Pernice, Waveguide integrated superconducting single-photon detectors with high internal quantum efficiency at telecom wavelengths, Scientific Reports **5**, 10941 (2015).

[134] E. Lomonte, M. A. Wolff, F. Beutel, S. Ferrari, C. Schuck, W. H. Pernice, and F. Lenzini, Single-photon detection and cryogenic reconfigurability in lithium niobate nanophotonic circuits, Nature Communications **12**, 6847 (2021).

[135] M. A. Wolff, S. Vogel, L. Splitthoff, and C. Schuck, Superconducting nanowire single-photon detectors integrated with tantalum pentoxide waveguides, Scientific Reports **10**, 17170 (2020).

[136] C. M. Natarajan, M. G. Tanner, and R. H. Hadfield, Superconducting nanowire single-photon detectors: physics and applications, Superconductor Science and Technology **25**, 063001 (2012).

[137] A. Engel, J. J. Renema, K. Il'In, and A. Semenov, Detection mechanism of superconducting nanowire single-photon detectors, Superconductor Science and Technology **28**, 114003 (2015).

[138] G. N. Gol'tsman, O. Okunev, G. Chulkova, A. Lipatov, A. Semenov, K. Smirnov, B. Voronov, A. Dzardanov, C. Williams, and R. Sobolewski, Picosecond superconducting single-photon optical detector, Applied Physics Letters **79**, 705 (2001).

[139] F. Marsili et al., Hotspot relaxation dynamics in a current-carrying superconductor, Physical Review B **93**, 094518 (2016).

[140] Y. Korneeva, I. Florya, S. Vdovichev, M. Moshkova, N. Simonov, N. Kaurova, A. Korneev, and G. Goltsman, Comparison of hot spot formation in NbN and MoN thin superconducting films after photon absorption, IEEE Transactions on Applied Superconductivity **27**, 2201504 (2017).

[141] A. D. Semenov, P. Haas, B. Günther, H. W. Hübers, K. Il'in, and M. Siegel, Energy resolution of a superconducting nanowire single-photon detector, Journal of Low Temperature Physics **151**, 564–569 (2008).

[142] M. Hofherr, D. Rall, K. Ilin, M. Siegel, A. Semenov, H.-W. Hübers, and N. A. Gippius, Intrinsic detection efficiency of superconducting nanowire single-photon detectors with different thicknesses, Journal of Applied Physics **108**, 014507 (2010).

[143] L. N. Bulaevskii, M. J. Graf, and V. G. Kogan, Vortex-assisted photon counts and their magnetic field dependence in single-photon superconducting detectors, Physical Review B **85**, 014505 (2012).

[144] R. H. Hadfield and G. Johansson, *Superconducting devices in quantum optics* (Springer International Publishing, 2016).

[145] M. Pu, L. Liu, H. Ou, K. Yvind, and J. M. Hvam, Ultra-low-loss inverted taper coupler for silicon-on-insulator ridge waveguide, Optics Communications **283**, 3678–3682 (2010).

[146] I. Krasnokutska, J.-L. J. Tambasco, and A. Peruzzo, Nanostructuring of LNOI for efficient edge coupling, Optics Express **27**, 16578–16585 (2019).

[147] L. He, M. Zhang, A. Shams-Ansari, R. Zhu, C. Wang, and L. Marko, Low-loss fiber-to-chip interface for lithium niobate photonic integrated circuits, Optics Letters **44**, 2314–2317 (2019).

[148] E. Unger, Die Erzeugung dünner Schichten. Das PECVD-Verfahren: Gasphasenabscheidung in einem Plasma, Chemie in unserer Zeit **25**, 148–158 (1991).

[149] D. T. Pierce and W. E. Spicer, Electronic structure of amorphous Si from photoemission and optical studies, Physical Review B **5**, 3017 (1972).

[150] C. Chang, Y. F. Wang, Y. Kanamori, J. J. Shih, Y. Kawai, C. K. Lee, K. C. Wu, and M. Esashi, Etching submicrometer trenches by using the Bosch process and its application to the fabrication of antireflection structures, Journal of Micromechanics and Microengineering **15**, 580 (2005).

[151] D. K. Ng, Q. Wang, T. Wang, S. K. Ng, Y. T. Toh, K. P. Lim, Y. Yang, and D. T. Tan, Exploring high refractive index silicon-rich nitride films by low-temperature inductively coupled plasma chemical vapor deposition and applications for integrated waveguides, ACS Applied Materials and Interfaces **7**, 21884–21889 (2015).

[152] J. M. Shainline, S. M. Buckley, N. Nader, C. M. Gentry, K. C. Cossel, J. W. Cleary, M. Popović, N. R. Newbury, S. W. Nam, and R. P. Mirin, Room-temperature-deposited dielectrics and superconductors for integrated photonics, Optics Express **25**, 10322–10334 (2017).

[153] G.-Z. Xu, W.-J. Zhang, L.-X. You, Y.-z. Wang, J.-M. Xiong, D.-H. Fan, L. Wu, H.-Q. Yu, H. Li, and Z. Wang, Millimeter-scale active area superconducting microstrip single-photon detector fabricated by ultraviolet photolithography, Optics Express **31**, 16348 (2023).

[154] Y. P. Korneeva, N. N. Manova, I. N. Florya, M. Y. Mikhailov, O. V. Dobrovolskiy, A. A. Korneev, and D. Y. Vodolazov, Different single-photon response of wide and narrow superconducting MoxSi1-x strips, Physical Review Applied **13**, 024011 (2020).

[155] J. Chiles, S. M. Buckley, A. Lita, V. B. Verma, J. Allmaras, B. Korzh, M. D. Shaw, J. M. Shainline, R. P. Mirin, and S. W. Nam, Superconducting microwire detectors based on WSi with single-photon sensitivity in the near-infrared, Applied Physics Letters **116**, 242602 (2020).

[156] G.-Z. Xu et al., Superconducting microstrip single-photon detector with system detection efficiency over 90% at 1550 nm, Photonics Research **9**, 958–967 (2021).

[157] M. Ejrnaes, C. Cirillo, D. Salvoni, F. Chianese, C. Bruscino, P. Ercolano, A. Cassinese, C. Attanasio, G. P. Pepe, and L. Parlato, Single photon detection in NbRe superconducting microstrips, Applied Physics Letters **121**, 262601 (2022).

[158] M. Yabuno, S. Miki, and H. Terai, Large-area niobium titanium nitride superconducting microstrip single-photon detector fabricated using a photolithography process, IEEE Transactions on Applied Superconductivity **33**, 2200104 (2023).

[159] J. S. Luskin et al., Large active-area superconducting microwire detector array with single-photon sensitivity in the near-infrared, arXiv, physics.ins–det, 2303.10739 (2023).

[160] J. R. Clem and K. K. Berggren, Geometry-dependent critical currents in superconducting nanocircuits, Physical Review B **84**, 174510 (2011).

[161] J.-M. Xiong et al., Reducing current crowding in meander superconducting strip single-photon detectors by thickening bends, Superconductor Science and Technology **35**, 055015 (2022).

[162] A. N. McCaughan, A. N. Tait, S. M. Buckley, D. M. Oh, J. T. Chiles, J. M. Shainline, and S. W. Nam, PHIDL: Python-based layout and geometry creation for nanolithography, Journal of Vacuum Science & Technology B **39**, 062601 (2021).

[163] F. Marsili et al., Detecting single infrared photons with 93% system efficiency, Nature Photonics **7**, 210–214 (2013).

[164] Y.-Z. Wang, W.-J. Zhang, G.-Z. Xu, J.-M. Xiong, D.-H. Fan, Z.-G. Chen, X.-Y. Zhang, Z. Wang, and L.-X. You, Characterization of a superconducting microstrip single-photon detector shunted with an external resistor, Superconductor Science and Technology **36**, 065004 (2023).

[165] E. E. Wollman et al., Recent advances in superconducting nanowire single-photon detector technology for exoplanet transit spectroscopy in the mid-infrared, Journal of Astronomical Telescopes, Instruments, and Systems **7**, 011004 (2021).

[166] S. Steinhauer, S. Gyger, and V. Zwiller, Progress on large-scale superconducting nanowire single-photon detectors, Applied Physics Letters **118**, 100501 (2021).

[167] B. Yurke, Use of cavities in squeezed-state generation, Physical Review A **29**, 408–410 (1984).

[168] M. S. Stefszky, C. M. Mow-Lowry, S. S. Y. Chua, D. A. Shaddock, B. C. Buchler, H. Vahlbruch, A. Khalaidovski, R. Schnabel, P. K. Lam, and D. E. McClelland, Balanced homodyne detection of optical quantum states at audio-band frequencies and below, Classical and Quantum Gravity **29**, 145015 (2012).

[169] J. M. Shainline, S. M. Buckley, A. N. McCaughan, J. Chiles, R. P. Mirin, and S. W. Nam, Superconducting optoelectronic neurons I: General principles, arXiv, cs.NE, 1805.01929 (2018).

[170] J. M. Shainline, S. M. Buckley, A. N. McCaughan, M. Castellanos-Beltran, C. A. Donnelly, M. L. Schneider, R. P. Mirin, and S. W. Nam, Superconducting optoelectronic neurons II: Receiver circuits, arXiv, cs.NE, 1805.02599 (2018).

[171] J. M. Shainline, A. N. McCaughan, S. M. Buckley, C. A. Donnelly, M. Castellanos-Beltran, M. L. Schneider, R. P. Mirin, and S. W. Nam, Superconducting optoelectronic neurons III: Synaptic plasticity, arXiv, cs.NE, 1805.02599 (2018).

[172] J. M. Shainline, S. M. Buckley, A. N. McCaughan, M. Castellanos-Beltran, C. A. Donnelly, M. L. Schneider, R. P. Mirin, and S. W. Nam, Superconducting optoelectronic neurons IV: Transmitter circuits, arXiv, cs.NE, 1805.02599 (2018).

[173] J. M. Shainline, J. Chiles, S. M. Buckley, A. N. McCaughan, R. P. Mirin, and S. W. Nam, Superconducting optoelectronic neurons V: Networks and scaling, arXiv, cs.NE, 1805.01942 (2018).

[174] S. Khan et al., Superconducting optoelectronic single-photon synapses, Nature Electronics **5**, 650–659 (2022).

[175] H. Vahlbruch, M. Mehmet, K. Danzmann, and R. Schnabel, Detection of 15 dB squeezed states of light and their application for the absolute calibration of photoelectric quantum efficiency, Physical Review Letters **117**, 110801 (2016).

[176] E. L. Wooten et al., Review of lithium niobate modulators for fiber-optic communications systems, IEEE Journal on Selected Topics in Quantum Electronics **6**, 69–82 (2000).

[177] J. Zheng et al., Photon counting reconstructive spectrometer combining metasurfaces and superconducting nanowire single-photon detectors, Photonics Research **11**, 234 (2023).

[178] R. Cheng, C.-L. Zou, X. Guo, S. Wang, X. Han, and H. X. Tang, Broadband on-chip single-photon spectrometer, Nature Communications **10**, 4104 (2019).

[179] L. Kong et al., Probabilistic energy-to-amplitude mapping in a tapered superconducting nanowire single-photon detector, Nano Letters **22**, 1587–1594 (2022).

[180] R. M. Heath, M. G. Tanner, T. D. Drysdale, S. Miki, V. Giannini, S. A. Maier, and R. H. Hadfield, Nanoantenna enhancement for telecom-wavelength superconducting single photon detectors, Nano Letters **15**, 819–822 (2015).

[181] M. Protte, N. Weber, C. Golla, T. Zentgraf, and C. Meier, Strong nonlinear optical response from ZnO by coupled and lattice-matched nanoantennas, Journal of Applied Physics **125**, 193104 (2019).

Appendix A

A.1 Publications

(1) Laser-lithographically written micron-wide superconducting nanowire single-photon detectors
Maximilian Protte, Varun B. Verma, Jan Philipp Höpker, Richard P. Mirin, Sae Woo Nam and Tim J. Bartley
Supercond. Sci. Technol. ***35****, 055055 (2022)*

(2) Opto-electronic bias of a superconducting nanowire single photon detector using a cryogenic photodiode
Frederik Thiele, Thomas Hummel, Maximilian Protte and Tim J. Bartley
APL Photonics ***7****, 081303 (2022)*

(3) Cryogenic electro-optic modulation in titanium in-diffused lithium niobate waveguides
Frederik Thiele, Felix vom Bruch, Julian Brockmeier, Maximilian Protte, Thomas Hummel, Raimund Ricken, Viktor Quiring, Sebastian Lengeling, Harald Herrmann, Christof Eigner, Christine Silberhorn and Tim J. Bartley *J. Phys. Photonics* ***4****, 034004 (2022)*

(4) Integrated superconducting nanowire single-photon detectors on titanium in-diffused lithium niobate waveguides
Jan Philipp Höpker, Varun B. Verma, Maximilian Protte, Raimund Ricken, Viktor Quiring, Christof Eigner, Lena Ebers, Manfred Hammer, Jens Förstner, Christine Silberhorn, Richard P. Mirin, Sae Woo Nam and Tim J. Bartley
J. Phys. Photonics ***3****, 034022 (2021)*

(5) Compact metasurface-based optical pulse-shaping device
René Geromel, Philip Georgi, Maximilian Protte, Shiwei Lei, Tim J. Bartley, Lingling Huang and Thomas Zentgraf
Nano Lett. ***23****, 3196-3201 (2023)*

(6) A versatile metasurface enabling superwettability for self-cleaning and dynamic color response
Jinlong Lu, Basudeb Sain, Philip Georgi, Maximilian Protte, Tim J. Bartley and Thomas Zentgraf
Adv. Optical Mater ***10****, 2101781 (2022)*

(7) **Selective area growth of cubic gallium nitride on silicon (001) and 3C-silicon carbide (001)**
Falco Meier, Maximilian Protte, Elias Baron, Martin Feneberg, Rüdiger Goldhahn, Dirk Reuter and Donat As
*AIP Advances **11**, 075013 (2021)*

A.2 Preprints

(1) **All optical operation of a superconducting photonic interface**
Frederik Thiele, Thomas Hummel, Adam N. McCaughan, Julian Brockmeier, Maximilian Protte, Victor Quiring, Sebastian Lengeling, Christof Eigner, Christine Silberhorn and Tim J. Bartley
*arXiv:2302.12123 **[quant-ph]** (2023)*

(2) **Degenerate photons from a cryogenic spontaneous parametric down-conversion source**
Nina Amelie Lange, Timon Schapeler, Jan Philipp Höpker, Maximilian Protte and Tim J. Bartley
*arXiv:2303.17428v1 **[quant-ph]** (2023)*

A.3 Conference Contributions

- CLEO USA, San José, 2022, **Direct laser lithography: Single-tool patterning for nonlinear integrated quantum optics**, *talk*
- ICIQP, Copenhagen, 2022, **A toolbox for integrated quantum photonics realized by direct laser lithography as a single patterning tool**, *talk*
- CLEO Europe, online, 2021, **Fabricating WSi based superconducting microwire single photon detectors with laser lithography**, *poster*
- Quantum 2.0, online, 2021, **Towards semiconductor-superconductor-crystal hybrid integration for quantum photonics**, *poster*
- Heraeus Seminar, online, 2021, **Superconducting microwire single-photon detectors fabricated with laser lithography**, *poster*
- DPG fall meeting, Freiburg, 2021, **Towards hybrid waveguides in lithium niobate for quantum optical applications**, *poster*

Table A.1: Design parameters for the homodyne chip

Structure	Dimensions	Step size
Directional coupler	Coupler Length: 6 – 8 mm	0.133 mm
Polarization Converter	Electrode Size: 15×0.1 mm^2 Electrode Gap: 15 µm Poling period: 20.98 – 21.36 µm	0.03 µm
Phase Shifter	Electrode Size: 1×0.1 mm^2 Electrode Gap: 9 µm	

A.4 Homodyne-Chip Layout

The figure A.1 shows schematic of the homodyne chip. 15 waveguide groups were fabricated as shown in the figure. For all directional coupler the coupler length was varied. Each group was farbicated with a different poling period. The phase shifter were all 1 cm long. The length of the polarization converter was 1.5 cm. The parameters for the different structures can be taken from the tab. A.1.

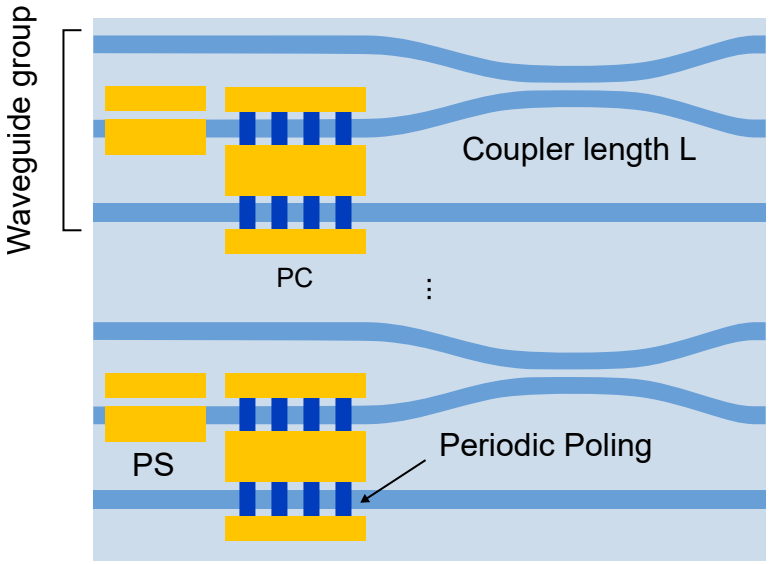

Figure A.1: Schematic of the homodyne chip. Each waveguide group has a directional coupler, a polarization converter (PC) and a phase shifter (PS). The poling period was varied for each waveguide group.

A.5 Variance of a Coherent State and Vacuum State

In this section I want to show that the variance of a coherent state/vacuum state is indeed given by

$$\Delta X_{1,\alpha}^2 = \frac{1}{4} = \Delta X_{2,\alpha}^2. \tag{A.1}$$

For this we consider a coherent state that can be written as

$$|\alpha\rangle = \exp\left(1/2|\alpha|^2\right) \sum_{n=0}^{\infty} \frac{\alpha^n}{\sqrt{n!}} |n\rangle \tag{A.2}$$

in the photon-number basis $|\alpha|^2$ is defined as the intensity of the local oscillator. The variance of an operator can be calculated with eq. 6.5. With the quadrature operators defined as in eq. 6.4 we need to calculate $\langle \hat{X}_{1,2}^2 \rangle$ and $\langle \hat{X}_{1,2} \rangle^2$. For $\langle \hat{X}_1 \rangle^2$ we can write:

$$\begin{aligned}
\langle \hat{X}_1 \rangle^2 &= \frac{1}{4} \left(\langle \alpha | \, \hat{a} + \hat{a}^\dagger \, | \alpha \rangle \right)^2 = \frac{1}{4} \left(\langle \alpha | \, \hat{a} \, | \alpha \rangle + \langle \alpha | \, \hat{a}^\dagger \, | \alpha \rangle \right)^2 \\
&= \frac{1}{4} \left(\alpha \langle \alpha | \alpha \rangle + \alpha^* \langle \alpha | \alpha \rangle \right)^2 = \frac{1}{4} \left(\alpha + \alpha^* \right)^2 \\
&= \frac{1}{4} \left(\alpha^2 + 2|\alpha|^2 + \alpha^{*^2} \right)
\end{aligned} \tag{A.3}$$

where we used the fact that a coherent state is the eigenstate of the annihilation operator with the eigenvalue α. For $\langle \hat{X}_1^2 \rangle$ we write

$$\langle \hat{X}_1^2 \rangle = \frac{1}{4} \left(\langle \alpha | \, \hat{a}^2 \, | \alpha \rangle + \langle \alpha | \, \hat{a}^{\dagger^2} \, | \alpha \rangle + \langle \alpha | \, \hat{a}\hat{a}^\dagger \, | \alpha \rangle + \langle \alpha | \, \hat{a}^\dagger \hat{a} \, | \alpha \rangle \right). \tag{A.4}$$

For simplicity, will will calculate each term separately, which gives

$$\begin{aligned}
\langle \alpha | \, \hat{a}^2 \, | \alpha \rangle &= \alpha^2, \\
\langle \alpha | \, \hat{a}^{\dagger^2} \, | \alpha \rangle &= \alpha^{*^2}, \\
\langle \alpha | \, \hat{a}^\dagger \hat{a} \, | \alpha \rangle &= |\alpha|^2, \\
\text{and } \langle \alpha | \, \hat{a}\hat{a}^\dagger \, | \alpha \rangle &= \langle \alpha | \, 1 \, | \alpha \rangle + \langle \alpha | \, \hat{a}^\dagger \hat{a} \, | \alpha \rangle = 1 + |\alpha|^2.
\end{aligned} \tag{A.5}$$

Now we can calculate the variance ΔX_1^2 with

$$\begin{aligned}
\Delta X_1^2 &= \langle \hat{X}_1^2 \rangle - \langle \hat{X}_1 \rangle^2 \\
&= \frac{1}{4} \left(\alpha^2 + 1 + 2|\alpha|^2 + \alpha^{*^2} \right) - \frac{1}{4} \left(\alpha^2 + 2|\alpha|^2 + \alpha^{*^2} \right) \\
&= \frac{1}{4}.
\end{aligned} \tag{A.6}$$

With this we have shown that the variance of the $\hat{X}_1$ is equal to 1/4. Since the vacuum state can be treated as a coherent state with an amplitude $\alpha = 0$ we get the same expression for the vacuum state. For the variance of $\hat{X}_2$ we can follow the same procedure. Doing the same calculation we can show that

$$\begin{aligned} \Delta X_2^2 &= \langle \hat{X}_2^2 \rangle - \langle \hat{X}_2 \rangle^2 \\ &= \frac{1}{4}\left(1 + 2|\alpha|^2 - \alpha^2 - \alpha^{*^2}\right) - \frac{1}{4}\left(2|\alpha|^2 - \alpha^2 - \alpha^{*^2}\right) \\ &= \frac{1}{4}. \end{aligned} \tag{A.7}$$

Acknowledgements

Now there is only one thing left to do, and that is to thank everyone who has supported me in my work. First and foremost, I would like to thank Prof. Dr. Tim J. Bartley for the opportunity to be part of his group, for the ambitious and inspiring atmosphere, and for the support in pursuing my own ideas and goals.

I would also like to thank Prof. Dr. Cedrik Meier, who not only agreed to evaluate my work, but also supported me in the lead-up to this work. I will always appreciate the chance to work in your group and also afterwards with your group members.

Next, I would like to thank all the members of the Mesoscopic Quantum Optics group. I would like to thank Dr. Thomas Hummel, Dr. Jan Philipp Höpker, Nina Lange, Johanna Biendl, Frederik Thiele, Julian Brockmeier, and Timon Schapeler for all the feedback and support inside and outside the university. Special thanks to Jan Philipp for the nice welcome and answering all my questions. I am convinced that we hold the world record for the fastest exchange of a detector sample in a cryostat. Thank you Timon, for all the late nights towards the end and the conscientious work we did together. Finally, I would like to give a special thanks to Johanna, not only for all the fun we had during the mentoring, but also for being part of the best two-person team in the cleanroom (at least in terms of humor). I am really looking forward to our SNSPDs.

I would also like to thank Prof. Dr. Christine Silberhorn for allowing me to work in her labs and learn a lot from her group members. Special thanks to Dr. Christof Eigner for his always motivating feedback. I would also like to thank Dr. Varun B. Verma and Dr. Adriana E. Lita for their support with the superconducting films.

I would like to thank the funding agencies Federal Ministry of Education and Research and the European Research Council for supporting this work.

Finally, I would like to thank my family and friends. Annette, Wolfgang, Sabine and Clara for all the support in the run-up to this work and during the last four and a half years I would like to thank you. I would like to thank my friends who have supported and cheered me on over the last few months. Without your support this would not have been possible.

Erklärung

Ich versichere, dass ich die Arbeit ohne fremde Hilfe und ohne Benutzung anderer als der angegebenen Quellen angefertigt habe und dass die Arbeit in gleicher oder ähnlicher Form noch keiner anderen Prüfungsbehörde vorgelegen hat und von dieser als Teil einer Prüfungsleistung angenommen worden ist. Alle Ausführungen, die wörtlich oder sinngemäß übernommen worden sind, sind als solche gekennzeichnet.

Ort, Datum

Unterschrift